The Dissertation Committee for Chih-Liang Wang Certifies that this is the approved version of the following dissertation:

DEVELOPMENT OF EARTH-ABUNDANT MATERIALS AND LOW-COST PROCESSES FOR SOLAR CELLS

Committee:

Arumugam Manthiram, Supervisor

Ananth Dodabalapur

Desiderio Kovar

Paulo J. Ferreira

Donglei Fan

DEVELOPMENT OF EARTH-ABUNDANT MATERIALS AND LOW-COST PROCESSES FOR SOLAR CELLS

by

Chih-Liang Wang, B.S.; M.S.

Dissertation

Presented to the Faculty of the Graduate School of

The University of Texas at Austin

in Partial Fulfillment

of the Requirements

for the Degree of

Doctor of Philosophy

The University of Texas at Austin

December 2014

Dedication

Dedicated to my wife Hui-Chieh, my daughter Amanda, and my parents Ping-Wen & Su-Hsia.

Acknowledgements

First of all, I am extremely grateful to my supervisor, Professor Arumugam Manthiram, for the valuable guidance, advice, and encouragement during my study and research. Particularly, my research work was a new topic and underwent many difficulties in the beginning. Professor Manthiram provided all the possible resources without conservation to make my research succeed. I would also like to thank Professor Desiderio Kovar and Donglei Fan for discussion on, respectively, ink preparation and nanomaterials as well as Professor Paulo J. Ferreira and Ananth Dodabalapur for introducing me to, respectively, materials analyses and solar cells in their graduate classes. I would also like to express my gratitude to all my dissertation committee members, Professor Desiderio Kovar, Paulo J. Ferreira, Ananth Dodabalapur, and Donglei Fan for serving on my committee and providing valuable input during my preliminary oral examination.

Additionally, I thank Dr. B. Reeja Jayan for her assistance, advice, and discussion on my research and Dr. Chih-Chieh Wang for the discussion on the synthesis of the buffer layer. I thank Dr. Jin-Yun Liao for the instruction and assistance on DSSC. I thank Dr. Yubao Zhao and Sheng-Heng Chung for their assistance on the hollow sphere/TEM analysis and the CSEM preparation. I thank Dr. Veronica Augustyn for the instruction in C-V measurement. I thank Dr. Eun Sung Lee, Zach Moorhead-Rosenberg, and Ke-Yu Lai for the assistance in Rigaku XRD and Dr. Yu-Sheng Su for the facility training. I thank Jackson Stolle for the assistance on the diffuse reflectance measurements. I also thank Dr. Yongzhu Fu and Eric Allcorn for their help to polish most of my manuscripts as well as all the past and current members of Professor Manthiram's group for their kind

help and support. Financial support by the Welch foundation grant number F-1254 is gratefully acknowledged.

Last but not least, I would like to express my heartfelt thanks to my beloved wife, Hui-Chieh, and my family who always provided unconditional support over the years and accompanied with me to overcome many of the difficulties during my Ph.D. studies.

DEVELOPMENT OF EARTH-ABUNDANT MATERIALS AND LOW-COST PROCESSES FOR SOLAR CELLS

Chih-Liang Wang, Ph.D.

The University of Texas at Austin, 2014

Supervisor: Arumugam Manthiram

The goal of renewable solar energy research is to develop low-cost, high-efficiency photovoltaic technologies. However, with the growing deployment of solar cells, approaching the terawatt scale, absorber materials reliant upon rare or unfriendly elements become a crucial issue. Thus, the primary objective of this dissertation is the development of a low-cost fabrication method for (i) thin-film solar cells and (ii) dye-sensitized solar cells using earth-abundant materials.

In thin-film solar cells, the kesterite Cu_2ZnSnS_4 with earth abundant elements is used as an absorber layer. It possesses a high absorption coefficient, direct band gap, and good long-term stability compared to the traditional CdTe and $Cu(In,Ga)(S,Se)_2$ (CIGS) absorber layers. A facile hot-injection approach for synthesizing $Cu_2ZnSn(S,Se)_4$ nanocrystals with varied Se to (S+Se) ratio is developed to systematically investigate the role of Se in $Cu_2ZnSn(S,Se)_4$ nanocrystals and the evolution of $Cu_2ZnSn(S,Se)_4$ nanocrystals to $Cu_2ZnSn(S,Se)_4$ film during the sulfurization step to address the problems associated with its narrow compositional window and the loss of Sn during heat treatment. Additionally, the existing substrate-type device configuration for these solar cells uses a molybdenum (Mo) back contact, which suffers from serious disadvantages

like the (i) presence of a Schottky barrier at the Mo/$Cu_2ZnSn(S,Se)_4$ interface and (ii) decomposition of $Cu_2ZnSn(S,Se)_4$ at the Mo interface. Accordingly, a low-cost and Mo-free superstrate-type device configuration of Au/$Cu_2ZnSn(S,Se)_4$/CdS/TiO_2/ITO/glass is developed to evaluate the conversion efficiency and to avoid the occurrence of a Schottky barrier at the interface and potential decomposition pathways induced by the formation of $Mo(S,Se)_2$. Furthermore, with the addition of ethyl cellulose, the loss of Sn associated with the conversion of CZTSe to CZTSSe during the grain growth process is mitigated, leading to an increase in the conversion efficiency compared to that of the precursor film without using ethyl cellulose. Such an improvement can provide insight into the grain growth of CZTSSe during the sulfurization process and thereby enhance the feasibility of sustainable, high efficiency CZTSSe solar devices.

The excellent characteristics of dye-sensitized solar cells (DSSCs) with short energy-payback time, simple assembly, and eco-friendly features make them a potential option to utilize solar energy. Accordingly, a facile, low-cost, template-free route for TiO_2 hollow submicrospheres embedded with SnO_2 nanobeans is developed for use as a versatile scattering layer in DSSCs. Our designed structure simultaneously promotes dye adsorption, light harvesting, and electron transport, leading to a 28 % improvement in the conversion efficiency as compared with the film-based SnO_2. In addition, a naturally-derived carbonaceous material as a Pt-free counter electrode for DSSCs is also developed for the first time: carbonized sucrose-coated eggshell membrane (CSEM). It is found that the carbonized sucrose-coated eggshell membranes consist of unique micropores of less than 2 nm, which effectively catalyze the triiodide into iodide in the light-electricity conversion process, leading to an improvement in the V_{oc} and a competitive efficiency as compared to that of a DSSC with a traditional Pt-based counter electrode.

Table of Contents

List of Tables xiii

List of Figures xiv

Chapter 1: Introduction 1

1.1 Types of solar cells 1

1.1.1 Thin-film solar cells 2

1.1.2 Operation principles of thin-film solar cells 3

1.1.3 Earth-abundant material 6

1.1.3.1 Sputtering techniques 6

1.1.3.2 Co-evaporation techniques 7

1.1.3.3 Electrochemical deposition techniques 7

1.1.3.4 Pure solution methods 8

1.1.3.5 Nanoparticle-based methods 9

1.1.3.6 Hybrid particle–solution methods 9

1.1.4 Cd-free buffer layer 10

1.2 Dye-Sensitized Solar Cells (DSSCs) 11

1.2.1 Operation principles of DSSC 11

1.2.2 Counter electrode 12

1.2.2.1 Platinum 13

1.2.2.2 Carbon materials 14

1.2.2.3 Polymers 14

1.2.2.4 Binary metal compounds 15

1.2.2.5 Nitrides 15

1.2.2.6 Sulfides 15

1.2.2.7 Phosphides 16

1.2.2.8 Selenides 16

1.2.2.9 Tellurides 17

1.2.2.10 Multiple compounds 17

1.2.2.11 Composite materials 17

1.2.3 Photoanodes 18
1.2.4 Electrolyte 19
1.2.5 Organic dyes 20
1.3 Objectives of this dissertation 20

Chapter 2: General experimental procedures 22
2.1 MATERIALS SYNTHESIS 22
2.2 MATERIALS CHARACTERIZATION TECHNIQUES 22
2.2.1 X-ray diffraction 22
2.2.2 Scanning electron microscopy and Energy dispersive X-ray spectroscopy 22
2.2.3 Transmission electron microscopy 23
2.2.4 Raman microscopy 23
2.2.5 UV-Vis-NIR 23
2.2.6 Surface area and pore-size measurements 23
2.2.7 Thermogravimetric analysis (TGA) 24
2.3 ELECTROCHEMICAL CHARACTERIZATION 24
2.3.1 Electrochemical impedance spectroscopy 24
2.3.2 Cyclic voltammetry 24
2.4 SOLAR CELL TESTING 24

Chapter 3: Low-cost, $Mo(S,Se)_2$-free superstrate-type solar cells fabricated with tunable band gap $Cu_2ZnSn(S_{1-x}Se_x)_4$ nanocrystal-based inks and the effect of sulfurization 26
3.1 Introduction 26
3.2 Experimental 30
3.2.1 Synthesis of $Cu_2ZnSn(S_{1-x}Se_x)_4$ nanocrystals 31
3.2.2 Fabrication of devices 31
3.2.3 Characterization of Materials 32
3.3 Results and discussion 32
3.4 Conclusions 41

Chapter 4: Low-cost CZTSSe solar cells fabricated with low band gap CZTSe nanocrystals, environmentally friendly binder, and non-vacuum processes 43

4.1 Introduction....43

4.2 Experimental....45

4.2.1 Synthesis of $Cu_2ZnSnSe_4$ nanocrystals....45

4.2.2 Fabrication of solar devices....45

4.2.3 Characterization of Materials....46

4.3 Results and discussion....47

4.4 Conclusions....64

Chapter 5: Template-free TiO_2 hollow microspheres embedded with SnO_2 nanobeans as a versatile scattering layer for dye-sensitized solar cells....65

5.1 Introduction....65

5.2 Experimental....66

5.2.1 Synthesis of SnO_2....66

5.2.2 Synthesis of TiO_2 hollow submicrospheres....67

5.2.3 Synthesis of nanobean SnO_2-embedded TiO_2 hollow submicrospheres....67

5.2.4 Assembly of DSSCs....69

5.2.5 Characterization of Materials....70

5.3 Results and discussion....71

5.4 Conclusions....82

Chapter 6: Carbonized eggshell membranes as a natural and abundant counter electrode for efficient dye-sensitized solar cells....83

6.1 Introduction....83

6.2 Experimental....84

6.2.1 Preparation of the counter electrode....84

6.2.2 Preparation of TiO_2 photoanode....85

6.2.3 Assembly of DSSCs....85

6.2.4 Materials characterization....86

6.3 Results and discussion....86

6.4 Conclusions....98

Chapter 7: Summary 99

Appendix: List of Publications 102

References.....103

Vita.....116

List of Tables

Table 1.1. Summary of three generation solar cells.....2

Table 3.1. Reported efficiencies of $Cu_2ZnSn(S,Se)_4$ nanocrystal-based absorbers.41

Table 4.1. Reported efficiencies of $Cu_2ZnSn(S,Se)_4$ nanocrystal-based absorbers.63

Table 5.1. Photovoltaic and EIS parameters of the cells with different scattering materials.....80

Table 6.1. Photovoltaic parameters of DSSCs based on CSEM, CP, and Pt CEs..93

Table 6.2. Reported efficiencies of DSSCs based on carbonized naturally-derived CEs.....94

List of Figures

Figure 1.1. Schematic of the light-electricity conversion in the p-n junction solar cell 3

Figure 1.2. Schematic of (a) CIGS thin-film solar cell, and (b) CdTe thin-film solar cell.....5

Figure 1.3. Schematic of dye-sensitized solar cell.....12

Figure 3.1. Illustration of solar cells with (a) the conventional substrate-type configuration and (b) the new superstrate-type configuration.....27

Figure 3.2. (a) Photographs of $Cu_2ZnSn(S_{1-x}Se_x)_4$ nanocrystal solutions with various Se/(S+Se) ratios of x = 0, 0.27, 0.52, 0.80, and 1.0; (b) compositional ratios of Cu/Sn, Zn/Sn, and Cu/(Zn+Sn) as a function of $Cu_2ZnSn(S_{1-x}Se_x)_4$ nanocrystal solution with various Se/(S+Se) ratios of x = 0, 0.27, 0.52, 0.80, and 1.0; (c) XRD analysis of $Cu_2ZnSn(S_{1-x}Se_x)_4$ nanocrystals with various Se/(S+Se) ratios of x = 0, 0.27, 0.52, 0.80, and 1.0; and (d) variations of the lattice constants *a* and *c* with x in the $Cu_2ZnSn(S_{1-x}Se_x)_4$ nanocrystals. 34

Figure 3.3. (a) Photograph of $Cu_2ZnSn(S_{1-x}Se_x)_4$ solar cells fabricated with our superstrate-type architecture. Cross-sectional SEM images of $Cu_2ZnSn(S_{1-x}Se_x)_4$ nanocrystals with (b) x = 0, (c) x = 0.27, (d) x = 0.52, (e) x = 0.80, and (f) x = 1.0 in the superstrate-type configuration after sulfurization. 35

Figure 3.4. (a) compositional ratios of $Cu_2ZnSn(S_{1-x}Se_x)_4$ nanocrystals with various Se/(S+Se) ratios of x = 0, 0.27, 0.52, 0.80, and 1.0 after sulfurization at 570 ^oC for 45 min; (b) change in S/(S+Se) and Cu/Sn compositional ratios in the $Cu_2ZnSn(S_{1-x}Se_x)_4$ nanocrystals with various Se/(S+Se) ratios of x = 0, 0.27, 0.52, 0.80, and 1.0 after sulfurization at 570 ^oC for 45 min; (c) conversion efficiency of superstrate-type configuration using a series of $Cu_2ZnSn(S_{1-x}Se_x)_4$ nanocrystal precursors; and (d) J - V characteristics of the superstrate-type configuration of the $Cu_2ZnSnSe_4$ nanocrystal precursor after sulfurization. 38

Figure 4.1. (a) XRD patterns of as-synthesized CZTSe nanocrystals, (b) Raman spectroscopic analyses of as-synthesized CZTSe nanocrystals, (c) UV-Vis absorption spectrum of as-synthesized CZTSe nanocrystals, and (d) color of the vial containing the CZTSe nanocrystals dispersed in ethanol with and without ethyl cellulose after the standing for a period of 5 min, 12 h, and 24 h. The inset in (c) shows a band gap of 1.05 eV for the as-synthesized CZTSe nanocrystals, determined by a plot of $(\alpha h\upsilon)^2$ as a function of $h\upsilon$. 48

Figure 4.2. Plane-view SEM images of CZTSe nanocrystals (a) with ethyl cellulose and (b) without ethyl cellulose after sulfurization at 480 ^oC. Cross-sectional SEM images of CZTSe nanocrystals (c) with ethyl cellulose after sulfurization at 550 ^oC and (d) without ethyl cellulose after sulfurization at 570 ^oC.. 50

Figure 4.3. (a) TGA plots of ethyl cellulose, (b) Cross-sectional SEM images of CZTSe nanocrystals with ethyl cellulose after sulfurization at 480 ^{o}C. Low magnification plane-view SEM images of CZTSe nanocrystals (c) without ethyl cellulose and (d) with ethyl cellulose after sulfurization at 480 ^{o}C. The change in the compositional ratios of (e) S/(S+Se) and (f) Sn/Cu in the CZTSe nanocrystals as a function of sulfurization temperature. 54

Figure 4.4. Raman spectroscopic analyses of the CZTSSe films fabricated with the CZTSe nanocrystals (a) without ethyl cellulose and (b) with ethyl cellulose as a function of sulfurization temperature.. 56

Figure 4.5. XRD patterns of (a) as-prepared CZTSe nanocrystals, and CZTSe nanocrystals (b) without ethyl cellulose and (c) with ethyl cellulose after the sulfurization at 550 ^{o}C on a superstrate-type substrate of CdS/TiO_2/ITO/soda-lime glass. 58

Figure 4.6. (a) V_{oc} of CZTSe nanocrystals with and without ethyl cellulose as a function of sulfurization temperature. (b) J_{sc} of CZTSe nanocrystals with and without ethyl cellulose as a function of sulfurization temperature. (c) FF of CZTSe nanocrystals with and without ethyl cellulose as a function of sulfurization temperature. (d) Conversion efficiency of CZTSe nanocrystals with and without ethyl cellulose as a function of sulfurization temperature. (e) J - V characteristics of CZTSSe solar device with ethyl cellulose after sulfurization at 550 ^{o}C as marked by red line and without ethyl cellulose after sulfurization at 570 ^{o}C as marked by black line. The dashed lines correspond to the dark J - V curves. (f) Cross-sectional SEM image of CZTSe nanocrystals with ethyl cellulose after sulfurization at 550 ^{o}C. 60

Figure 4.7. The content of (a) Cd, (b) Ti, and (c) In in the CZTSSe as a function of sulfurization temperature. 62

Figure 5.1. High and low magnification SEM images of SnO_2. 68

Figure 5.2. High and low magnification SEM images of TiO_2 hollow submicrospheres.....68

Figure 5.3. High and low magnification SEM images of nanobean SnO_2-embedded TiO_2 hollow submicrospheres.....69

Figure 5.4. 2-D schematic diagram showing the formation of nanobean SnO_2-embedded TiO_2 hollow submicrospheres (HS).....71

Figure 5.5. (a) XRD analysis of the TiO_2 HS before and after the embedding of SnO_2 nanobeans; (b) STEM line scan analysis and SEM image (inset) of the nanobean SnO_2-embedded TiO_2 HS; and (c) elemental mapping of the nanobean SnO_2-embedded TiO_2 HS. 72

Figure 5.6. TEM image of (a) the nanobean SnO_2-embedded TiO_2 HS; (b) high-magnification TEM image and the SAED patterns (inset) of the nanobean SnO_2-embedded TiO_2 HS; (c) high-resolution TEM images of the nanobean SnO_2-embedded TiO2 HS; (d) N_2 adsorption and desorption isotherms of the TiO_2 HS before and after the formation of SnO_2 nanobeans; pore-size distribution of the (e) TiO_2 hollow microsphere and (f) nanobean SnO_2-embedded TiO_2 HS.....74

Figure 5.7. Cross-sectional SEM image of the bilayer photoanode of SnO_2 on the nano-sized TiO_2 transparent layer.....76

Figure 5.8. Cross-sectional SEM image of the bilayer photoanode of TiO_2 hollow submicrospheres on the nano-sized TiO_2 transparent layer.....77

Figure 5.9. Cross-sectional SEM image of the bilayer photoanode of nanobean SnO_2-embedded TiO_2 hollow submicrospheres on the nano-sized TiO_2 transparent layer.....78

Figure 5.10. (a) Amount of dye loading, (b) UV-diffuse reflectance, (c) J - V characteristics, and (d) Nyquist plot of the DSSCs with different scattering layers of SnO_2, TiO_2 HS, and SnO_2-embedded TiO_2 HS atop the nano-sized TiO_2 film.....79

Figure 5.11. The equivalent-circuit diagram of the cell was used to extract the parameters of R_s (series resistance), R_{cr} (charge-recombination resistance), and R_{ct} (charge-transfer resistance).....81

Figure 6.1. In-plane SEM images of (a) an eggshell membrane, (b) CSEM, (c) CSEM after grinding with a mortar and pestle, and (d) cross-sectional SEM image of a CSEM mixed with CP.....88

Figure 6.2. Cross-sectional SEM image of CSEM without CP. 89

Figure 6.3. (a) Cyclic voltammetry of CSEM, CP, and Pt at 100 mV s^{-1}, (b) Raman spectra of CSEM and CP, (c) nitrogen adsorption-desorption isotherms of CSEM and CP, (d) pore-size distributions of CSEM and CP, (e) J-V characteristics of DSSCs with CSEM, CP, and Pt CEs, and (f) Nyquist plots of CSEM, CP, and Pt CEs. 92

Figure 6.4. DSSC device parameters as a function of the ratio of CP: (a) V_{oc}, (b) J_{sc}, (c) FF, and (d) PCE.. 95

Figure 6.5. The resistivity of the counter electrodes as a function of the ratio of CP 96

Chapter 1: Introduction

1.1 TYPES OF SOLAR CELLS

With the dramatic growth of the global population to 7 billion in the 21st century, the shortage of fossil fuels and the effect of global warming caused by carbon dioxide (CO_2) emissions from large amounts of fossil fuel combustion become a thorny problem. Solar energy possesses the inherent advantages of being a clean, never-exhausted, and environmental-friendly resource as well as offering potential for decentralization of power production making it the ideal next-generation alternative energy source. A solar cell is a photoelectric conversion device that generates electricity out of sunlight when under illumination. Since the first silicon solar cell was devised by Daryl Chapin, Calvin Souther Fuller, and Gerald Pearson at Bell Laboratories in 1954, many research efforts have been made for the development of solar photovoltaic technologies that have been mainly categorized into the three generations of solar cells in Table 1.1.[1] The mature commercial products such as mono and polycrystalline silicon solar cells are usually regarded as the first generation. Thin-film solar cells composed of 1 – 2 μm thick absorber layers like amorphous silicon (a-Si), cadmium telluride (CdTe), and copper indium gallium selenide (CIGS), among others are classified as the second generation. Lastly, the solar cells with conversion efficiencies beyond the Shockley – Queisser limit belong to the third generation. These include multi-gap tandem cells, quantum dot solar cells, hot electron converts, and so on. Even though many research efforts have recently been made on second and third generation solar cells, most of them remain at the research stage.

Table 1.1. Summary of three generation solar cells

Generation	Technology
1st	Mono Si, polycrystalline Si, etc.
2nd	a-Si, thin-film Si, CIGS, CdTe, DSSC, organic/molecular based solar cells, etc.
3rd	Multi-gap tandem cells, quantum dot solar cells, hot electron converts, etc.

1.1.1 Thin-film solar cells

Thin-film solar cells comprised of 1 – 2 μm thick absorber layers are promising for the development of low-cost solar cells. The main advantages of thin-film solar cells are light weight, flexibility, and great facility with building integrated photovoltaics (BIPV). Three major active materials used for thin-film solar cell technologies are amorphous silicon (a-Si), cadmium telluride (CdTe), and copper indium gallium selenide (CIGS). Although the non-toxic, abundant a-Si with a high absorption coefficient is well-known for its earlier application on solar calculators, the fatal shortcoming of light degradation due to the Staebler-Wronski effect poses difficulties. Thus, direct-band-gap CdTe and CIGS with high absorption coefficient and excellent long-term stability have become alternative candidates for the absorber materials. The current record-high efficiencies with CdTe (21%) and CIGS (21.7%) further demonstrate their potential on thin-film solar cell technologies.[2]

1.1.2 Operation principles of thin-film solar cells

Thin-film solar cells based on a p-n heterojunction as shown in Figure 1.1 are mainly composed of three processes to convert the light into electricity: charge generation, charge separation, and charge transport. The electron-hole pair is first generated by the absorption of light. Subsequently, the electron-hole pair is separated by the built-in voltage in the depletion region of the p-n junction. Finally, the photo-induced electron and hole are individually delivered to the external circuit.

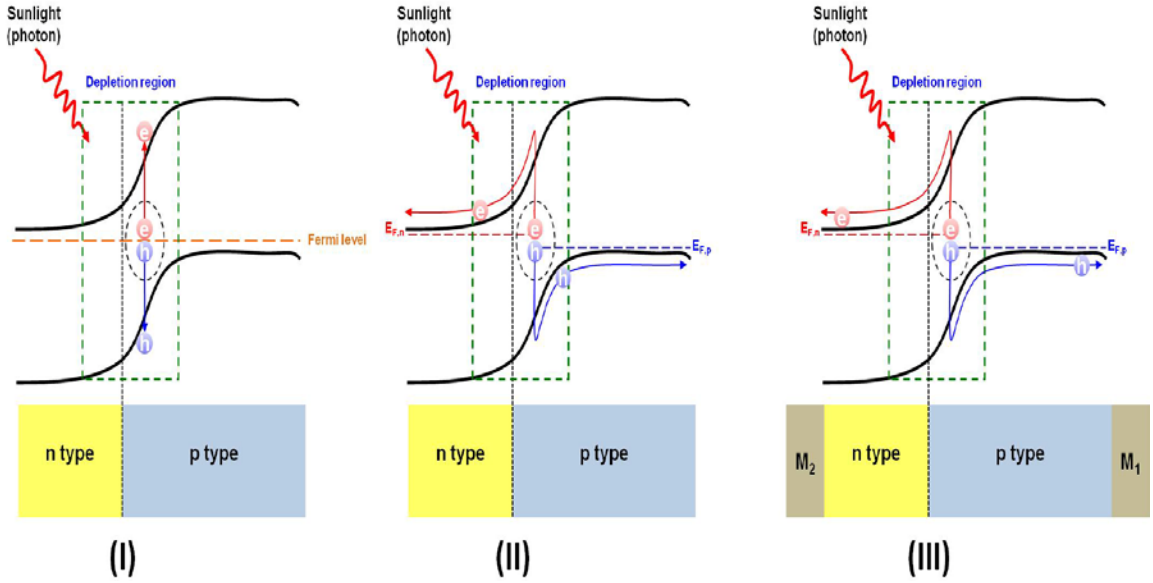

Figure 1.1. Schematic of the light-electricity conversion in the p-n junction solar cell

An efficient thin-film solar cell requires a compatible device structure to satisfy the above-mentioned requirements. Figure 1.2a depicts the common film-stack substrate-type substrate for use in CIGS.[3] The Mo back contact is first deposited onto the soda-lime glass to form the ohmic contact. The p-type CIGS absorber layer with copper vacancies (V_{Cu}) is fabricated with a co-evaporation process or a two-step process (selenization of

metal alloys). Next, the n-type CdS buffer layer with sulfur vacancies (V_S) is coated by a chemical-bath deposition and then sputtered with intrinsic zinc oxide (i-ZnO). Finally, a transparent conductive layer of aluminum-doped zinc oxide (AZO) is deposited on top of the i-ZnO by the sputtering technique as a top contact for electron transport. Unlike CIGS, which exhibits a high efficiency on the substrate-type substrate, CdTe mainly adopts the superstrate-type substrate to achieve higher efficiency as shown in Figure 1.2b.[4, 5] The main reason could be the different properties of absorber layers and interfacial conditions at buffer layer/absorber layer, varying with different fabrication sequences. The front-contact of a transparent conductive layer is followed by a high electrical resistivity metal-oxide layer, which is applied to a soda-lime glass by sputter deposition. The n-type CdS buffer layer with sulfur vacancies (V_S) is fabricated with chemical-bath deposition. The active layer of p-type CdTe with cadmium vacancies (V_{Cd}) is often fabricated by a technique of close-spaced sublimation (CSS). A heat treatment in chlorine is used to re-crystallize the nano-sized grains and significantly improve the CdTe film quality. The back-contact layer of Mo, W, or C is fabricated with a sputtering system. Unlike CdTe and CIGS, amorphous silicon has adopted a p-i-n device structure to compensate for its shorter diffusion length.[6]

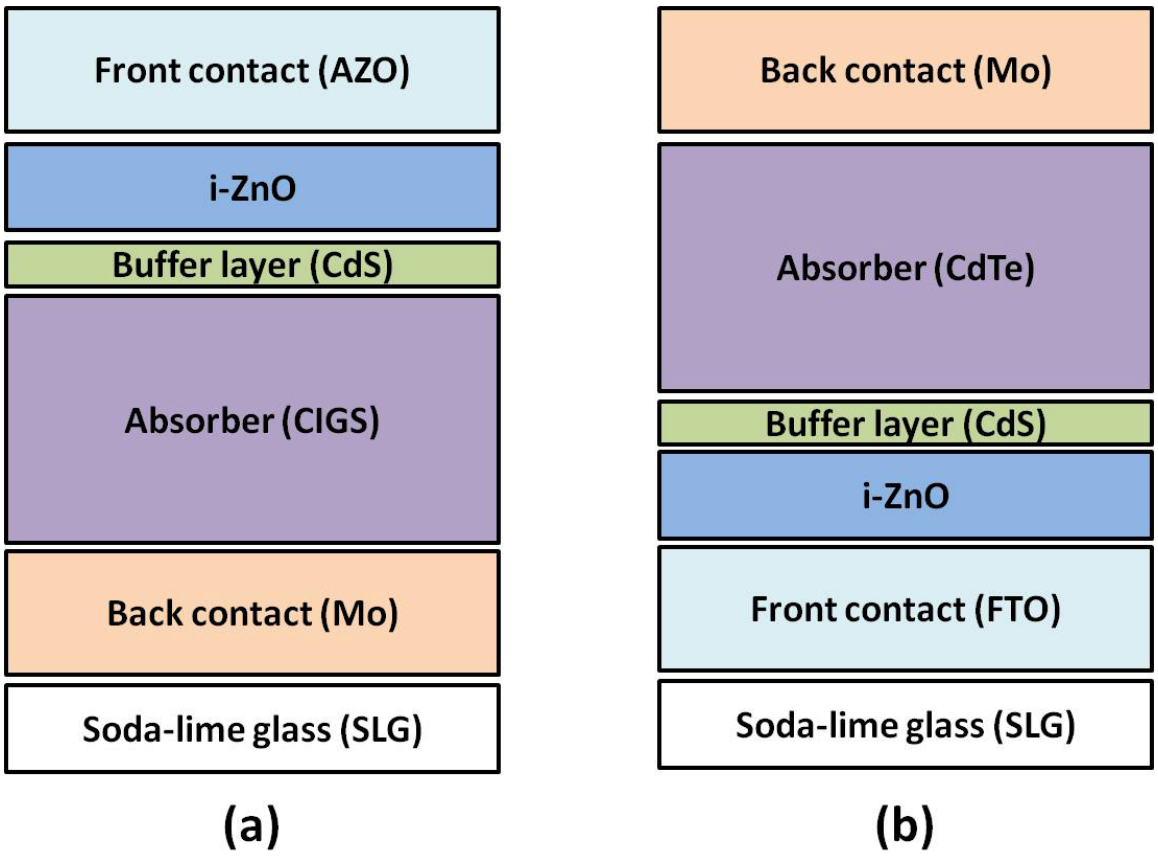

Figure 1.2. Schematic of (a) CIGS thin-film solar cell and (b) CdTe thin-film solar cell.

1.1.3 Earth-abundant material

The recent record-high efficiencies of CdTe and CIGS secure their potential as alternatives to amorphous silicon. However, with the targeted deployment of solar cells reaching the terawatt scale, those materials composed of rare or unfriendly elements will become a crucial issue. The heavy-metal cadmium utilized in CdTe has been banned in many countries because of concerns over environmental poisoning. In addition, both tellurium used in CdTe and indium and gallium used in CIGS are less abundant and expensive. Therefore, much attention has been paid to the use of earth-abundant materials. A promising candidate to meet these requirements is the kesterite-related $Cu_2ZnSn(S,Se)_4$ (CZTSSe) that possesses a high absorption coefficient of 10^4 cm^{-1}, is composed of low-cost, non-toxic, abundant elements, and offers good long-term stability.[7] In addition, the optical and electrical properties of the $Cu_2ZnSn(S,Se)_4$ series of materials could be easily tuned by varying the ratio of S/Se in $Cu_2ZnSn(S,Se)_4$ and thereby increasing the energy band gap from 1.0 to 1.5 eV with increasing amount of sulfur. Nevertheless, the narrow compositional window of stable single phases in the phase diagram leads to difficulties in the manufacturing process of $Cu_2ZnSn(S,Se)_4$. In other words, without strict environmental and processing conditions, secondary phases are easily formed, limiting its application in solar devices. Thus, many different methods to synthesize CZTSSe have been explored and they are presented below.[8]

1.1.3.1 Sputtering techniques

The sputtering technique is one of the most common fabrication techniques for CZTSSe. The first reported kesterite CZTS material was fabricated with the sputtering technique by Ito & Nakazawa in 1988.[9] Next, Katagiri *et al.* developed a two-stage fabrication process by preparing multi-stack sputtered metal precursors or co-sputtered

metal-alloy precursors, followed by a high-temperature heat treatment in the presence of sulfur. In 2008, a conversion efficiency of 6.7% was reported by the same group.[10] Several key findings have been reported, such as a Cu-poor and Zn-rich condition to form a preferred defect of copper vacancy V_{Cu} in CZTS, decomposition of CZTS resulting in the loss of Sn during heat treatment, and formation of secondary phases. Recently, an efficiency of 8% has been achieved by using binary targets of $Cu_x(S,Se)_y$, $Zn_x(S,Se)_y$ and $Sn_x(S,Se)_y$ followed by a heat treatment in the presence of SnS and S_2 to form a high quality film.[8]

1.1.3.2 Co-evaporation techniques

The co-evaporation technique has been a successful method to fabricate high-quality and high-efficiency CIGS solar cells because of its excellent capability to individually control the evaporated elements.[11] However, CZTS/Se involving Sn re-evaporation and volatile S/Se in a high temperature substrate makes it hard to produce a high-quality film by co-evaporation approach.[8] Some research reports have been proposed to mitigate the loss of Sn by developing a fast co-evaporation process or increasing Sn overpressure in the process.[12-15] An IBM group recently demonstrated an efficiency of 8.4% by first co-evaporating pure CZTS in a low-temperature process followed by a short annealing procedure.[16, 17]

1.1.3.3 Electrochemical deposition techniques

Electrochemical deposition is a well-developed industrial technology due to its advantages of being a non-vacuum process, having high throughput, and having high materials utilization. The electroplating process is mainly used to make CuZnSn alloy

precursor on a Mo substrate, followed by heat treatment in the presence of S or Se vapor to convert the electroplated alloy precursors into CZTS/Se. Previous studies have reported that secondary phases remain in the resulting film. The different electroplated metal or alloy stack sequences will also affect the device performance and the adhesion to the Mo substrate.[18-21] Recently, an IBM group demonstrated an efficiency of 7.3% by improving the intermixing of electroplated precursor films via an additional heat treatment at 350 ^{o}C before the selenization/sulfurization process.[22] However, a large amount of oxygen involved during the fabrication process was found in the resulting CZTSSe film, which may limit the potential of electrochemical deposition techniques.

1.1.3.4 Pure solution methods

The sol-gel solution process is regarded as the ideal synthesis method. It has low-cost and scalability advantages as well as being a simple and environmentally friendly preparation technique. An efficiency of 2.2% has been achieved by preparing a sol–gel solution composed of copper (II) acetate monohydrate, zinc (II) acetate dihydrate, tin (II) chloride dihydrate, and 2-methoxyethanol solvent.[23] However, it is challenging to produce a single homogeneous phase and void-free film directly from the sol-gel solution. An efficiency of 4.1% was obtained by dimethyl sulfoxide (DMSO) solvent mixing with metal salts and thiourea.[24] Recently, an efficiency of 8.3 % was obtained using the same dimethyl sulfoxide (DMSO) solvent by tuning the precursors to produce a pure kesterite phase even though imperfect morphology was still observed.[25]

1.1.3.5 Nanoparticle-based methods

The nanoparticle-based method has the advantages of low-cost manufacturing and higher throughput.[26] However, an efficient device based on nanoparticle-based methods requires a sintering process and suitable liquid vehicles to produce a compact film composed of large-size grains.[8] In 2009, Steinhagen *et al* first demonstrated an efficiency of 0.23%.[27] In the same year, Guo *et al* improved the efficiency to 0.8% by sintering CZTS nanoparticles in the presence of Se vapor.[28] In 2010, a conversion efficiency of 6.7% was demonstrated by the same group by modifying the coating technique of CZTS nanoparticles using hexanethiol solvent followed by the same selenization process.[29] Recently, DuPont demonstrated an efficiency of 8.5 % by adopting binary and ternary metal chalcogenide nanoparticles dispersed in hexanethiol, rather than using quaternary CZTS nanoparticles to precisely control the composition.[30]

1.1.3.6 Hybrid particle–solution methods

The hybrid particle-solution approach for CZTSSe was first demonstrated by an IBM group.[31] This approach is able to produce a dense and crack-free high-quality CZTSSe film by providing a combination of the advantages of particle-based and solution-based methods without requiring the binder. Two slurries - chalcogenide hydrazine solution (Cu_2S–S and SnSe-Se) and particle-based Zn-chalcogenide precursors (ZnSe(N_2H_4) or ZnS(N_2H_4)) - are prepared individually and mixed together to form a hybrid particle–solution slurry for the spin-coating technique. The chalcogenide hydrazine solution not only serves as a binding media but also provides the intimate contact with Zn-chalcogenide precursors, which can facilitate a fast chemical reaction and homogeneous phase formation. With the availability of higher quality CZTSSe film, the different material properties between CZTSSe and CIGS could be investigated and

provide insights for the improvement of high-performance devicees.[8, 32, 33] The first working device made by IBM achieved an efficiency of 9.6%, which is higher than the previous approaches.[31] Recently, a record-high efficiency of 12% was further demonstrated by the same group via an improvement to the optical design in the film-stack structure.[34, 35] However, this hybrid particle–solution method using the strong reducing agent hydrazine has a fatal shortcoming: handling hydrazine requires appropriate protective equipment to avoid explosion and fire, making it hard for large-scale manufacturing. However, an efficiency of 8.1% has still been achieved by replacing pure hydrazine with safer, diluted hydrazine mixtures (hydrazine–water–ammonia),[36] but there is still a lot of room for the development of a safe slurry to meet the requirements of the large-scale manufacturing.

1.1.4 Cd-free buffer layer

The current record-high efficiency of CZTSSe, 12.6%, is beyond the commercial threshold efficiency of 10%.[34] However, the widespread commercialization of CZTSSe is impeded by the use of the heavy metal cadmium, which has been banned in many countries under the hazardous substances directive (RoHS) adopted by the European Union in 2003. It has also been reported that the conduction band offset at the CdS/$Cu_2ZnSn(S,Se)_4$ interface is higher than the optimum value of 0.4 eV and can, therefore, result in a lower J_{sc} and fill factor.[37] Thus, a desirable Cd-free buffer layer with a suitable optimum band offset will become an urgent mission in the near future. Even though previous knowledge on CIGS and many research efforts have already been applied towards Cd-free buffer layers such as ZnO, ZnS, In_2S_3,[38] many of them remain at the research stage.[39]

1.2 Dye-Sensitized Solar Cells (DSSCs)

Dye-sensitized solar cells (DSSCs) are based on a photoelectrochemical system to convert light into electricity under the illumination.[40] Unlike the p-n junction solar cells, the operation of DSSCs is based on the photosynthesis process in plants and it allows the individual manipulation of the light absorption and charge transfer processes, offering greater flexibility in dealing with material design. The excellent capability of dye-sensitized solar cells (DSSCs) in achieving short energy payback time, simple assembly, and eco-friendly features make them a potential technology for renewable energy use.

1.2.1 Operation principles of DSSC

The prototypical architecture of a DSSC consists of a porous film of n-type TiO_2, a photosensitized dye, a redox couple consisting of I^-/I_3^- electrolyte, and a Pt counter electrode as shown in Figure 1.3.[40] Upon solar illumination, the dye molecule undergoes an electronic transition from the ground state to the excited state. This is followed by an ultrafast electron injection from the excited state of the dye molecule into the conduction band of TiO_2, which leads to the oxidation of the dye molecule. The oxidized dye subsequently stimulates the reduction of iodide into triiodide in the electrolyte, and the electron injected into the conduction band of TiO_2 is transported to the counter electrode via the external circuit. The collected electron at the counter electrode is used to regenerate iodide from triiodide in order to complete the light-electricity conversion process.

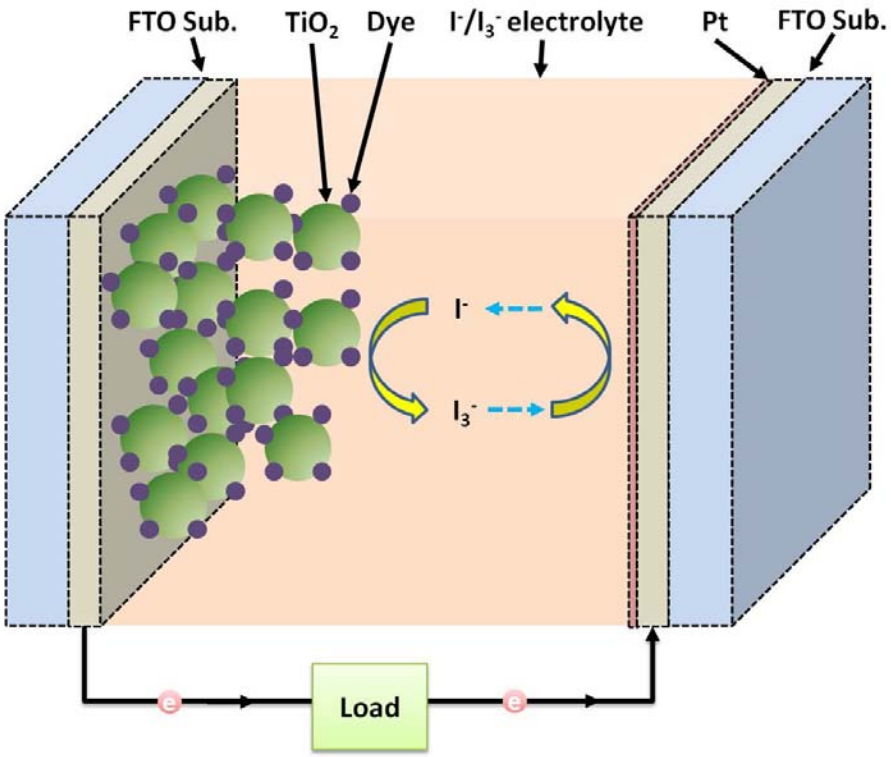

Figure 1.3. Schematic of dye-sensitized solar cell

1.2.2 Counter electrode

The role of the counter electrode in the DSSCs is to deliver the electron and catalyze the regeneration of iodide from triiodide to complete the light-electricity conversion process.[41] The most common material used for counter electrodes is platinum (Pt) due to its high electrical conductivity and great catalytic ability to regenerate iodide from triiodide. Many key findings from the studies using Pt counter electrodes laid the foundation of DSSC technology. However, with the target of expanding solar generation up to the terawatt scale, the noble and scarce nature of Pt as well as its poor stability in the electrolyte has become a significant hurdle to realize low-cost, and thus, large-scale deployment of DSSCs. Thus, the emergence of Pt-free counter electrodes has been paid

much attention recently. More detailed progress associated with Pt and Pt-free counter electrodes will be discussed below.

1.2.2.1 Platinum

Platinum (Pt) has been one of the most extensively studied materials for DSSC technologies. The Pt counter electrode is typically fabricated onto a fluorine-doped tin oxide (FTO) substrate. Many methods for synthesizing Pt counter electrodes have been explored, such as sputtering deposition, electrodeposition, pyrolysis, chemical reduction, and vapor deposition.[42-46] In particular, the chemical reduction method is one of the most common approaches due to its simplicity, low temperature, high catalytic activity, and low Pt loading. The influence of Pt on catalytic activity was also investigated by the Ma group.[47] It was found that a Pt thickness of 2 nm is sufficient to offer good catalytic activity for use in DSSCs and that Pt film below 10 nm remains transparent. Pt thickness beyond 25 nm enables light reflection to enhance light utilization.[47] On the other hand, the catalytic ability of Pt is related with its exposed facets, which follows the sequence of Pt (111) > Pt (411) > Pt (100) calculated by density functional theory (DFT).[48] Experimental results are also consistent with the theoretical calculation and show that DSSCs using a Pt (111) oriented counter electrode has the highest efficiency relative to those using Pt (411) and Pt (100) orientations.[49] The recent champion DSSC using a Pt counter electrode has achieved a conversion efficiency of 13%.[50] However, the noble and scarce nature of Pt has become a significant hurdle to realize low-cost, and thus, large-scale deployment of DSSCs. Seeking Pt-free counter electrodes to address these challenges has become an important research topic.

1.2.2.2 Carbon materials

Carbon has been one of the more promising candidates for Pt-free counter electrodes due to its advantages of low cost, high catalytic activity, high electrical conductivity, high thermal stability, and good corrosion resistance.[41] Many carbon-based materials have been explored, such as activated carbon (Ca), carbon black (Cb), conductive carbon (Cc), carbon dye (Cd), carbon fiber (Cf), mesoporous carbon (Cm), carbon nanotubes (CNTs), fullerene, graphene, and so on.[51] However, the common problem of carbon materials is the poor adhesion between carbon and the substrate, strongly limiting their long-term use. Recently, using carbon paste to improve the adhesion onto the substrate has been proposed.[52] In addition, another shortcoming of carbon materials is their opacity that requires the development of transparent carbon materials for semi-transparent applications.[53] Overall, the carbon materials possess many merits to become the most competitive alternative to Pt counter electrode material for the low-cost and high performance commercial DSSCs.

1.2.2.3 Polymers

Developing a polymer material as the counter electrode is essential for the sake of the advancement of transparent and flexible DSSCs. Several conductive polymer materials with good catalytic activity, easy accessibility, and low-cost have been adopted as counter electrodes in DSSCs. These include poly(3,4-ethylenedioxythiophene) polystyrene sulfonate (PEDOT:PSS), polypyrrole (PPy), polyaniline (PANI), and so on.[41] Developing a new organic polymer with long-term stability is required for application in commercial DSSCs.

1.2.2.4 Binary metal compounds

Since 2009, significant research efforts have focused on binary metal compounds to investigate the possibility of replacing the rare and noble Pt counter electrode in DSSCs. These binary metal compounds include carbides, nitrides, sulfides, phosphides, and so on. In carbide-based compounds, tungsten carbide (WC) was first used for the counter electrode of a DSSC by Lee *et al.*[54] The Ma group then adopted tungsten carbide (WC) and molybdenum carbide (MoC) for DSSCs.[55] Subsequently, various carbides such as TiC, VC, NbC, Cr_3C_2, Ta_4C_3, SiC, and ZrC were developed and evaluated for their efficiencies in DSSCs. Most of them show high catalytic activity with the exception of SiC and ZrC.[41]

1.2.2.5 Nitrides

Because of the similar properties of nitrides to carbides, such as high hardness, high melting point, and high electrical and thermal conductivity, a variety of nitrides such as TiN, Mo_2N, MoN, W_2N, WN, Fe_2N, NiN, VN, NbN, CrN, and Ta_4N_5 were also developed to investigate the catalytic activity as applied to DSSCs as a counter electrode.[41] In particular, an efficiency of 8.31% was obtained by using large surface area nitride particles with a mesoporous structure.[56]

1.2.2.6 Sulfides

CoS was first synthesized and applied to DSSC as a counter electrode due to the lower cost and abundant nature of elemental cobalt. Since the Grätzel group demonstrated an efficiency of 6.5% by using CoS nanoparticles and verified its long-term stability in severe conditions, sulfide counter electrodes have gained much attention.[57]

Many sulfides have been synthesized and adopted as counter electrodes in DSSCs such as CoS nanorods, Co_8S_9, NiS nanoarrays, $Co_{8.4}S_8$, Ni_3S_2, $Cu_{1.8}S$, Bi_2S_3, and FeS_2.[58-65] More recently, the syntheses of MoS_2 and WS_2 by the Ma group were introduced as counter electrodes in DSSCs, demonstrating efficiencies of 7.59% and 7.73%, respectively, for MoS_2 and WS_2, which is comparable to that of Pt with 7.64%.[66]

1.2.2.7 Phosphides

Some phosphides such as Ni_5P_4 and MoP have also been synthesized and introduced as counter electrodes. Though efficient devices using Ni_5P_4 (5.71%) and MoP (4.92%) have been made, an efficiency of phosphides higher than that of Pt has not been reported yet.[67] There is still much room for further development of phosphide counter electrodes.

1.2.2.8 Selenides

Cobalt selenide ($Co_{0.85}Se$) and nickel selenide ($Ni_{0.85}Se$) were synthesized and introduced as counter electrodes in DSSCs by the Wang group.[68] The device using $Ni_{0.85}Se$ shows an efficiency of 8.32% and that using $Co_{0.85}Se$ yields an efficiency of 9.40%, which exceeds that using Pt (8.64%). DSSCs using $NiSe_2$ and CoSe have also been reported to show higher efficiencies than Pt.[69, 70] In addition, some new selenides such as $NbSe_2$ nanosheets and nanorods were successfully synthesized, and they yielded an efficiency close to the DSSC based on a Pt counter electrode.[71]

1.2.2.9 Tellurides

CoTe and $NiTe_2$ synthesized by the Ma group were also introduced as counter electrodes and they produced efficiencies of, respectively, 6.92% and 7.21%, which are comparable to the DSSC based on Pt (7.04%).[72]

1.2.2.10 Multiple compounds

Unlike the binary compounds mentioned above, multiple compounds composed of three or more elements have been adopted as the counter electrode in DSSCs. Copper zinc tin sulfide (CZTS) was initially developed as a multiple compound based counter electrode.[73, 74] Work by the Lin group demonstrates efficiencies of 3.62% and 7.37%, respectively, by using the counter electrode based on CZTS nanoparticles (CZTS) and selenization of nanoparticles (CZTSSe). The Wu group subsequently synthesized CZTSe and produced an efficiency of 7.82% by optimizing its thickness to 1.2 μm.[75] $CuInS_2$ with different morphologies, such as vertically-oriented $CuInS_2$ nanosheet, and nanocrystals, were also investigated by a different group. An efficiency of 6.33%, comparable to that of sputtered Pt (6.07%), was reached by optimizing the vertically-oriented $CuInS_2$ nanosheet.[76] Other ternary compounds such as $NiCo_2S_4$, $CoMoS_4$ and $NiMoS_4$ have been synthesized by the Lin group.[77, 78] Their efficiencies after adding the graphite can be comparable to that of Pt.

1.2.2.11 Composite materials

Composite counter electrodes are composed of two or more constituent materials with different physical or chemical properties. The investigation of composite counter electrodes has been paid much attention due to their high catalytic activity and

combination of advantages. Some composite materials that have been investigated are WC/ordered mesoporous carbon, MoC/ordered mesoporous carbon, TiN/carbon nanotubes, and Pt/carbon.[79] New composite materials based on different combinations are continually being developed. The Ma group synthesized WO_2/mesoporous carbon and VC/mesoporous carbon and showed them to possess higher activities than Pt.[80, 81] The Han group developed a new system of metal/polypyrrole/C and showed efficiencies in DSSCs using Co/polypyrrole/C (7.64%) and Ni/polypyrrole/C (7.44%), higher than that of bare carbon (6.26%).[82] Some binary compounds combined with graphene, such as MoS_2/graphene, NiS/graphene and CoS/graphene,[83-85] or combined with multi-wall carbon nanotubes, such as WS_2/MWCNTs and MoS_2/MWCNTs,[86, 87] have also been introduced as counter electrodes. The Ouyang group adopted single wall carbon nanotubes/reduced graphene oxide (SWCNTs/rGO) as a counter electrode and produced an efficiency of 8.37%, higher than that of Pt (7.79%).[88] In addition to the carbon-based composite materials, Pt-based composite materials such as TiC/Pt, WO_2/Pt, and VN/Pt have also been investigated.[89] The Wang group has also synthesized one dimensional $CuInS_2$-ZnS heterostructured nanorods and showed a conversion efficiency of 7.5%, higher than that of Pt (7.1%).[90]

1.2.3 Photoanodes

A nanosized TiO_2 film with 10 – 15 μm of thickness functions as the photoanode in DSSCs to physically adsorb the molecular dye and transport the injected electron from the dye to the external circuit. Different metal oxides in addition to TiO_2 have been explored such as Al_2O_3, ZnO, and SnO_2, and the results have shown that the device performance of DSSCs is strongly affected by the materials properties of the photoanode.

On the other hand, the morphology of the photoanode has also been used to improve the light scattering and electron transport. A variety of shapes such as large particles, nanotubes, nanowires, nanospindles, electrospun fibers, nano-embossed hollow spheres, hexagonal plates, and photonic crystals have been investigated.[91] Recently, a bilayer structure composed of a nanosized transparent layer and a scattering layer has been paid much attention due to the enhancement of the device performance by effectively improving the light scattering. Different structural designs for the scattering layer are also investigated such as double light-scattering film,[92] surface plasmon effects,[93-95] 1-3D nanostructured designs,[96] quintuple-shelled hollow microspheres,[97] and multi-stack structures.[98]

1.2.4 Electrolyte

The electrolyte serves as the medium to connect between the TiO_2 photoanode and the counter electrode in DSSCs. The ionic conductivity in the electrolyte will directly affect the device performance. There are three main DSSC electrolytes: I-mediated electrolyte, Co-complexes-mediated electrolyte, and S-mediated electrolyte.[40] The most commonly used one is I-mediated electrolyte while the greatest device efficiency has been achieved by using Co-complexes-mediated electrolyte. However, the same counter electrodes show different efficiencies in different electrolytes. For instance, the efficiency of a carbon counter electrode is usually less than that of a Pt counter electrode in an I-mediated electrolyte but it outperforms the Pt counter electrode in the S-mediated electrolyte.[40]

1.2.5 Organic dyes

The dye is an important component to convert the incident light into electricity in the DSSC. Upon solar illumination, the dye molecule undergoes an electronic transition from the ground state to an excited state. An ultrafast electron injection from the excited state of the dye molecule into the conduction band of TiO_2 allows transport of the electron out through TiO_2. The most commonly used dyes are ruthenium-based dyes because they have demonstrated good performance in DSSCs. However, the ruthenium-based dyes are limited by purification, synthesis processes, and low molar extinction coefficients.[40] Thus, metal-free dyes have been paid much attention recently due to the higher freedom of the molecular design and higher molar extinction coefficients. Recently, dyes incorporated with a donor-π-acceptor (D-π-A) structure have become a promising route to optimize the property of the dye due to its flexibility of structural design.[99, 100] Many studies are focused on tuning the donor groups, engineering the conjugated bridges, and optimizing the acceptor/anchors in D-π-A dyes to improve the properties of the dyes such as the absorption, charge recombination rate, long-term stability, and injection efficiency.[40]

1.3 OBJECTIVES OF THIS DISSERTATION

The primary objective of this dissertation is to develop a low-cost fabrication method for solar cells using earth-abundant materials. Two types of solar cells are investigated: (i) thin-film solar cells and (ii) dye-sensitized solar cells. Accordingly, the general experimental techniques and procedures are initially described in Chapter 2. In Chapter 3, $Cu_2ZnSn(S,Se)_4$ nanocrystals with tunable properties are successfully synthesized by a hot-injection approach and the relationships among $Cu_2ZnSn(S,Se)_4$ nanocrystals, sulfurization, and $Cu_2ZnSn(S,Se)_4$ films are systematically investigated. In

addition, a low-cost superstrate-type substrate is developed to evaluate the conversion efficiency and provide $Cu_2ZnSn(S,Se)_4$ with a transformative solution to avoid the occurrence of potential decomposition pathways induced by the formation of $Mo(S,Se)_2$ at the substrate interface. In Chapter 4, the sulfurization process is used to optimize the band gap and investigate the effect of S doping into CZTSe nanocrystals during heat treatment. In addition, the loss of Sn associated with the conversion of CZTSe to CZTSSe nanocrystals is studied by comparing the ink with and without the addition of ethyl cellulose.

In Chapter 5, a bilayer structural design composed of a light-scattering layer and a nano-sized transparent layer for use in dye-sensitized solar cells (DSSCs) is developed for the enhancement of light harvesting. A facile, low-cost, template-free route for TiO_2 hollow submicrosphere embedded with SnO_2 nanobeans for use as a versatile scattering layer in DSSC is designed and the relationship among our designed structure as well as the dye adsorption, light harvesting, and electron transport in DSSC are explored. In Chapter 6, a naturally-derived carbonaceous material as a Pt-free counter electrode for DSSCs is explored: carbonized sucrose-coated eggshell membrane (CSEM). This material made from eggshell membranes are recycled from domestic waste and applied to DSSCs to realize large-scale deployment at an affordable cost. The catalytic activity and sites are investigated by cyclic voltammetry (C-V) and Raman spectroscopy. The surface area and the pore-size distribution are also studied by Brunauer-Emmett-Teller (BET) method. The study here not only investigates the relationship between the microstructure and the charge-transfer process but also brings new insights into the future application of natural materials for use in DSSCs. Finally, Chapter 7 provides a summary of the investigations.

Chapter 2: General experimental procedures

2.1 MATERIALS SYNTHESIS

All the chemicals used in the experiments were ACS grade without further purification. The synthesis procedures for $Cu_2ZnSn(S,Se)_4$ nanoparticles, metal-oxide photoanodes, and Pt-free counter electrodes are described in detail in each individual chapter.

2.2 MATERIALS CHARACTERIZATION TECHNIQUES

2.2.1 X-ray diffraction

The crystal structures of the materials were characterized with a Philips X-ray diffractometer (XRD) or a Rigaku X-ray diffractometer using Cu Kα radiation. The crystalline phases were referenced from the JCPDS cards.

2.2.2 Scanning electron microscopy and Energy dispersive X-ray spectroscopy

The in-plane and cross-sectional scanning electron microscopy (SEM) images for the microstructure morphology were collected with a FEI Quanta 650. The compositional analyses and the elemental mapping of the materials were carried out with a JEOL5610 SEM or a Hitachi S5500 scanning electron microscope (SEM)/scanning transmission electron microscope (STEM), both equipped with energy dispersive spectroscopy (EDS).

2.2.3 Transmission electron microscopy

The microstructure and crystal structure analyses were conducted with a JEOL 2010F transmission electron microscope (TEM) with an accelerating voltage 200 kV. The TEM samples were prepared on copper grids.

2.2.4 Raman microscopy

The Raman spectra were acquired with a Renishaw inVia Raman Microscope using 532 nm laser excitation at a 50 X objective.

2.2.5 UV-Vis-NIR

The band gap of nanoparticles and the amount of dye adsorption were acquired with a Cary 5000 UV-Vis-NIR spectrometer. Diffuse reflectance spectra were recorded with a Varian Cary 500 UV-Vis-NIR instrument equipped with an integrating sphere of a Labsphere DRA-CA-5500.

2.2.6 Surface area and pore-size measurements

The surface area and pore-size distributions were measured by the Brunauer-Emmett-Teller (BET) method with an automated gas sorption analyzer (AutoSorb iQ2, Quantachrome Instruments). The samples were baked at 100 ^{o}C for 24 h in a vacuum oven. The pore-size distribution plots were based on Horvath-Kawazoe (HK) model (micropore analysis) and density functional theory (DFT) model (micro/mesopore analysis).

2.2.7 Thermogravimetric analysis (TGA)

Thermogravimetric analysis (TGA) was performed with a Perkin Elmer TGA 7 with 5 ^{o}C per minute heating rate under a flow of argon.

2.3 ELECTROCHEMICAL CHARACTERIZATION

2.3.1 Electrochemical impedance spectroscopy

The electrochemical properties were analyzed by electrochemical impedance spectroscopy (EIS) data collected with a program-controlled Solartron SI 1287 and SI 1260 instrument. The ingredients of the as-prepared electrolyte contained 0.6 M 1-methyl-3-propylimidazolium iodide (PMII), 0.05 M lithium iodide (LiI), 0.03 M iodine (I_2), 0.1 M of guanidinium thiocyanate (GuNCS), and 0.5 M 4-tert-butyl-pyridine (tBP) in a mixture of acetonitrile and valeronitrile (85:15 in volume ratio).

2.3.2 Cyclic voltammetry

Three-electrode cyclic voltammetry (C-V) ($Ag/AgNO_3$ as a reference electrode and Pt foil as a counter electrode) was utilized to analyze the electrochemical activities. A liquid electrolyte composed of 0.1 M $LiClO_4$, 10 mM LiI, and 1 mM I_2 in acetonitrile was used.

2.4 SOLAR CELL TESTING

The current density-voltage (J - V) characteristics using a solar simulator with a 100 mW cm^{-2} light illumination under AM 1.5 G conditions were measured by a Keithley 2400 source measurement unit. All samples for the solar device performances were tested

with the light illuminating through the ITO side of the substrate. Silver paste was used to reduce the contact resistance between ITO and the wire.

Chapter 3: Low-cost, $Mo(S,Se)_2$-free superstrate-type solar cells fabricated with tunable band gap $Cu_2ZnSn(S_{1-x}Se_x)_4$ nanocrystal-based inks and the effect of sulfurization*

3.1 INTRODUCTION

The earth-abundant kesterite Cu_2ZnSnS_4 with a high absorption coefficient of 10^4 cm^{-1}, direct band gap, and good long-term stability has become an attractive candidate for use in solar cell absorber layers as it is composed of non-toxic, abundant elements compared to the traditional CdTe and $Cu(In,Ga)(S,Se)_2$ (CIGS) thin-film absorbent layers.[7] However, the vulnerability of the $Cu_2ZnSn(S,Se)_4$ system to decomposition pathways (equation 1) during heat treatment leads to different requirements for producing efficient $Cu_2ZnSn(S,S_4)$-based devices compared to CIGS.[101, 102]

$$Cu_2ZnSn(S,Se)_4\,(s) \rightarrow Cu_2(S,Se)\,(s) + Zn(S,Se)\,(s) + Sn(S,Se)\,(g) + \tfrac{1}{2}\,(S,Se)_2\,(g) \qquad (1)$$

This decomposition can be avoided by providing excess $(S,Se)_2$ gas or a Sn(S,Se) source during the heat treatment of $Cu_2ZnSn(S,Se)_4$.[103] However, heat treatment can lead to the formation of $Mo(S,Se)_2$ at the interface between the Mo back contact and the $Cu_2ZnSn(S,Se)_4$ active layer interface (Figure 3.1a).

While beneficial to devices based on the CIGS system, $Mo(S,Se)_2$ is detrimental to the $Cu_2ZnSn(S,Se)_4$ system due to the formation of an undesirable Schottky barrier at the $Mo/Cu_2ZnSn(S,Se)_4$ interface.[104] Moreover, $Mo(S,Se)_2$ can accelerate the decomposition of $Cu_2ZnSn(S,Se)_4$.[105] Despite approaches such as use of a diffusion

* C.-L. Wang, C.-C. Wang, B. Reeja-Jayan and A. Manthiram, "Low-cost, $Mo(S,Se)_2$-free superstrate-type solar cells fabricated with tunable band gap $Cu_2ZnSn(S_{1-x}Se_x)_4$ nanocrystal-based inks and the effect of sulfurization," *RSC Advances* 3, 19946-19951 (2013). C.-L. Wang carried out the experimental work. C.-C. Wang and B. Reeja-Jayan provided assistance in the discussion and experimental details. Dr. A. Manthiram supervised the project.

barrier of TiN or alloyed Mo metal to reduce the impact of (S,Se) on Mo,[106, 107] the formation of $Mo(S,Se)_2$ cannot completely be eliminated. It is, therefore, challenging to fabricate high-quality $Cu_2ZnSn(S,Se)_4$ devices while using a Mo back contact. Unfortunately, all current $Cu_2ZnSn(S,Se)_4$ research is based on the typical substrate-type device structure with an Mo back contact (Figure 3.1a), which may become a critical bottleneck for increasing the power conversion efficiency of these devices.

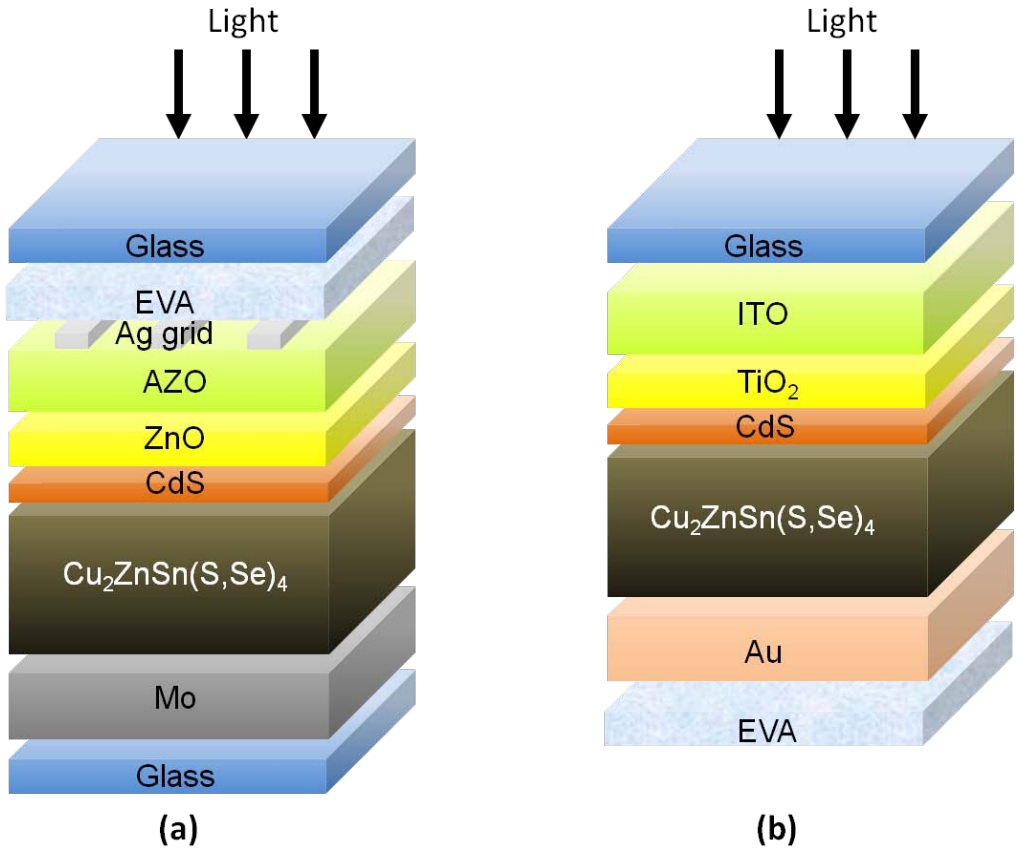

Figure 3.1. Illustration of solar cells with (a) the conventional substrate-type configuration and (b) the new superstrate-type configuration. EVA refers to ethylene vinyl acetate, which was used for encapsulating the solar cells.

On the other hand, high efficiency has been achieved with CdTe on a superstrate-type substrate, as compared to that of CIGS with a substrate-type substrate with Mo back contact.[2] Such a difference indicates that not only the quality of the absorbent film but also the interfacial condition varied by the heat treatment is important for producing high-efficiency solar cells. While the current device efficiency of $Cu_2ZnSn(S,Se)_4$ remains far behind those of CIGS and CdTe, it is highly possible to further raise the conversion efficiency of $Cu_2ZnSn(S,Se)_4$ by adopting a suitable substrate to promote the film quality and the interfacial conditions.

We present here that inverting the existing $Cu_2ZnSn(S,Se)_4$ device structure to have a bottom substrate of CdS/TiO_2/ITO/soda-lime glass instead of Mo during the sulfurization of $Cu_2ZnSn(S,Se)_4$ can help address the aforementioned problems associated with the formation of $Mo(S,Se)_2$. This novel superstrate-type configuration of $Au/Cu_2ZnSn(S,Se)_4/CdS/TiO_2$/ITO/soda-lime glass, shown in Figure 3.1b, includes a bifunctional interlayer of CdS to circumvent the formation of $Mo(S,Se)_2$ and avoid the occurrence of potential decomposition pathways. Such a superstrate-type architecture has additional benefits like simplifying the mechanistic studies of $Cu_2ZnSn(S,Se)_4$, blocking the diffusion of Na from the glass substrate into the active layer using a window layer of TiO_2, and reducing the overall manufacturing cost of $Cu_2ZnSn(S,Se)_4$ modules by utilizing a single piece of glass to both offer support and encapsulate the device in the module. In addition, our work on the $Cu_2ZnSn(S,Se)_4$ system with a superstrate-type device architecture could provide alternative approaches to assess the possibility of replacing CdTe by $Cu_2ZnSn(S,Se)_4$ to greatly impact the solar cell market.

A variety of techniques to make kesterite-related materials such as Cu_2ZnSnS_4, $Cu_2ZnSn(S,Se)_4$ and $Cu_2ZnSnSe_4$ have been reported.[18, 28, 108-111] Although a record high efficiency of 11% with the $Cu_2ZnSn(S,Se)_4$ family has been achieved using a

hydrazine-based approach,[33] hydrazine is a toxic and unstable chemical, which is not suitable for large-scale commercial manufacturing processes. Alternatively, adopting $Cu_2ZnSn(S,Se)_4$ nanocrystals as the initial precursor with a robust, easily scalable, and relatively safe manufacturing process becomes an attractive alternative to control the kesterite-related structure with tunable quaternary compositions and spatial compositional uniformity. Since Cu_2ZnSnS_4 nanocrystal-based inks followed by a selenization process has been demonstrated by Guo *et al*,[29] nanocrystal-based inks have been considered a promising route for producing a high quality absorbent layer in the Cu_2ZnSnS_4 devices. However, the strong chemical reaction of Se vapor during selenization causes undesirable effects on $Cu_2ZnSn(S,Se)_4$ devices,[106] as compared to the mild chemical and environmentally friendly reaction of S vapor during sulfurization. Furthermore, S being more abundant in the earth's crust compared to Se makes the sulfurization process more cost-effective compared to selenization. These advantages make the sulfurization of $Cu_2ZnSn(S,Se)_4$ nanocrystals attractive for development of high-quality, low cost $Cu_2ZnSn(S,Se)_4$ films. Unfortunately, currently there are no studies on the effect of sulfurization on the properties of $Cu_2ZnSn(S,Se)_4$ nanocrystals and their films.

Accordingly, we present here the controllability of Cu-poor and Zn-rich $Cu_2ZnSn(S_{1-x}Se_x)_4$ nanocrystals with various S to Se ratios, synthesized by a facile hot-injection approach using only oleylamine reagent, to successfully synthesize a series of $Cu_2ZnSn(S_{1-x}Se_x)_4$ nanocrystals and investigate the role played by Se in $Cu_2ZnSn(S_{1-x}Se_x)_4$ during the sulfurization. Additionally, the proposed low-cost superstrate-type device structure of $Cu_2ZnSn(S_{1-x}Se_x)_4$/CdS/TiO_2/ITO/soda-lime glass without the effect of $Mo(S,Se)_2$ and Na diffusion has been demonstrated for the first time in the $Cu_2ZnSn(S,Se)_4$ class of materials. This new architecture also provides a stable platform

to conduct mechanistic studies that can help correlate materials characteristics with device performance.

3.2 EXPERIMENTAL

The superstrate-type device structure of $Cu_2ZnSn(S_{1-x}Se_x)_4$/CdS/TiO_2/ITO/soda-lime glass, as shown in Figure 3.1b, was devised for the first time and compared to the typical device structure of Figure 3.1a. The 30 nm thick anatase TiO_2 layer was fabricated by a sol-gel synthesis, followed by heat treatment at 450 ^oC for 2 h on ITO-coated glass slides purchased from Nanocs (Product No. ITO-0021-50). The CdS buffer layer was deposited on top of the TiO_2 layers by chemical bath deposition (CBD). Dense CdS thin-film layers were obtained during CBD inside a water bath maintained at 65 ^oC for 15 min. The Cu-poor and Zn-rich $Cu_2ZnSn(S_{1-x}Se_x)_4$ nanocrystals, with Se/(S+Se) ratios of x = 0, 0.27, 0.52, 0.80, 1.0, were synthesized by the hot-injection approach under an argon atmosphere to investigate the influence of Se in $Cu_2ZnSn(S_{1-x}Se_x)_4$ nanocrystals during the sulfurization. A (S+Se) anion precursor to Cu ratio higher than 2.5 was prepared for the hot-injection process. An ink consisting of $Cu_2ZnSn(S_{1-x}Se_x)_4$ nanocrystals and ethanol was spincoated onto the top of the CdS buffer layer. The $Cu_2ZnSn(S_{1-x}Se_x)_4$ film was formed by sulfurization of the spincoated $Cu_2ZnSn(S_{1-x}Se_x)_4$ layer at 570 ^oC for 45 min. The sulfurization process was performed inside a graphite box containing 10 mg sulfur powder under argon flow. A mild HCl (hydrogen chloride) etching process was applied for the devices after the sulfurization step. Finally, a thermally evaporated gold electrode was used to define an active device area of 0.1 cm^2 by using the high-purity gold wire with 0.5 mm in diameter and 5 cm in length.

3.2.1 Synthesis of $Cu_2ZnSn(S_{1-x}Se_x)_4$ nanocrystals

The $Cu_2ZnSn(S_{1-x}Se_x)_4$ nanocrystals were prepared by a hot-injection method. The Cu, Zn, and Sn ionic precursors were chosen as copper(II) acetylacetonate [$Cu(acac)_2$], zinc acetate [$Zn(O_2CCH_3)_2$], and tin(II) chloride dihydrate [$SnCl_2.2H_2O$], respectively. The Cu-poor and Zn-rich compositions were kept during the synthesis of these $Cu_2ZnSn(S_{1-x}Se_x)_4$ nanocrystals. In a typical synthesis, 1.68 mmol of copper(II) acetylacetonate, 1.4 mmol of zinc acetate, and 1.0 mmol of tin(II) chloride dehydrate were added into a 500 mL 3-neck flask with 30 mL of oleylamine. A (S+Se) anion precursor to Cu ratio of higher than 2.5 times was prepared for the hot-injection process. As that oleylamine solution of Cu, Zn, and Sn ionic precursors was heated at 200 ^oC, a 10 mL of oleylamine solution with various ratios of elemental S and Se (x = 0, 0.25, 0.5, 0.75, and 1) was injected, followed by heating at 250 ^oC for 1 h under argon atmosphere. After the reaction, the solution was precipitated by methanol and washed by isopropyl alcohol /hexane three times to remove the residual oleylamine.

3.2.2 Fabrication of devices

A 30 nm thick anatase TiO_2 layer was fabricated by a sol-gel synthesis, followed by heat treatment at 450 ^oC for 2 h on ITO-coated glass slides purchased from Nanocs (New York, NY). The CdS buffer layer using the mixed aqueous solutions of $CdSO_4$, NH_2CSNH_2, NH_4OH, and deionized water was deposited onto the top of the TiO_2 layer by chemical-bath deposition (CBD). Dense CdS thin-film layers were obtained during CBD inside a water bath maintained at 65 ^oC for 15 min. An ink consisting of $Cu_2ZnSn(S_{1-x}Se_x)_4$ nanocrystals and ethanol was prepared and spincoated onto the top of the CdS buffer layer. The $Cu_2ZnSn(S_{1-x}Se_x)_4$ film was formed by sulfurization of the spincoated $Cu_2ZnSn(S_{1-x}Se_x)_4$ layer. The sulfurization process was carried out by placing

the sample of as-synthesized $Cu_2ZnSn(S_{1-x}Se_x)_4$ nanocrystals/CdS/TiO_2/ITO/soda-lime glass inside a graphite box with sulfur powders at 570 ^oC in a tubular furnace for 45 minutes under argon flow. A mild hydrogen chloride (HCl) etching process was applied for the whole device after the sulfurization. Finally, a thermally evaporated gold electrode was used to define an active device area of 0.1 cm^2.

3.2.3 Characterization of Materials

The $Cu_2ZnSn(S_{1-x}Se_x)_4$ crystals were characterized with a Philips X-ray diffractometer (XRD) using Cu Kα radiation. The cross-sectional SEM images were collected with a FEI Quanta 650. The compositional analyses were carried out by an energy-dispersive X-ray spectroscopy (EDS) equipped in a JEOL5610 SEM. The current density-voltage (J - V) characteristics using a solar simulator with a 100 $mWcm^{-2}$ light illumination under AM 1.5 G conditions were measured by a Keithley 2400 source measurement unit. All samples for the solar device performances were tested with the light illuminating through the ITO side of the substrate.

3.3 RESULTS AND DISCUSSION

To examine the influence of the content of Se in $Cu_2ZnSn(S_{1-x}Se_x)_4$ during the sulfurization, a series of Cu-poor and Zn-rich $Cu_2ZnSn(S_{1-x}Se_x)_4$ nanocrystals with various S to Se ratios based on a kesterite structure are required. Figure 3.2a shows the photographs of $Cu_2ZnSn(S_{1-x}Se_x)_4$ nanocrystal solutions with the energy band gaps tuned by varying the Se/(S + Se) ratios as x = 0, 0.27, 0.52, 0.80, and 1.0. In Figure 3.2b, the compositional analysis by energy-dispersive X-ray spectroscopy (EDS) indicates that the S to Se ratio in $Cu_2ZnSn(S_{1-x}Se_x)_4$ nanocrystals under Cu-poor and Zn-rich conditions can

be varied by our hot-injection approach. X-ray diffraction (XRD) analysis shown in Figure 3.2c indicates that the pure Cu_2ZnSnS_4 and $Cu_2ZnSnSe_4$ nanocrystals exhibit diffraction peaks that match with those in the JCPDS cards 26-0575 and 70-8930, respectively.

With increasing Se content in the $Cu_2ZnSn(S_{1-x}Se_x)_4$ nanocrystals, the diffraction peaks shift to lower angles due to the substitution of larger Se (0.198 nm) for smaller S (0.184 nm). Additionally, the lattice constants *a* and *c* of $Cu_2ZnSn(S_{1-x}Se_x)_4$ obtained from the XRD data in Figure 3.2d reveal that the volume of the $Cu_2ZnSn(S_{1-x}Se_x)_4$ unit cell increases with increasing amount of Se in $Cu_2ZnSn(S_{1-x}Se_x)_4$. These results indicate that the $Cu_2ZnSn(S_{1-x}Se_x)_4$ nanocrystals could be successfully synthesized and tuned by the hot-injection method. Contrary to Riha *et al*,[112] who synthesized $Cu_2ZnSn(S_{1-x}Se_x)_4$ by using extra $NaBH_4$ and toxic trioctylphosphine oxide, and Ou *et al*,[113] who synthesized by dissolving thiourea in 1-octadecenee, our hot-injection approach employing high amounts of elemental anion precursors and involving direct mixing of S with Se in oleylamine demonstrates a facile, environmentally benign, and easily scalable route to synthesize a series of $Cu_2ZnSn(S_{1-x}Se_x)_4$ nanocrystals.

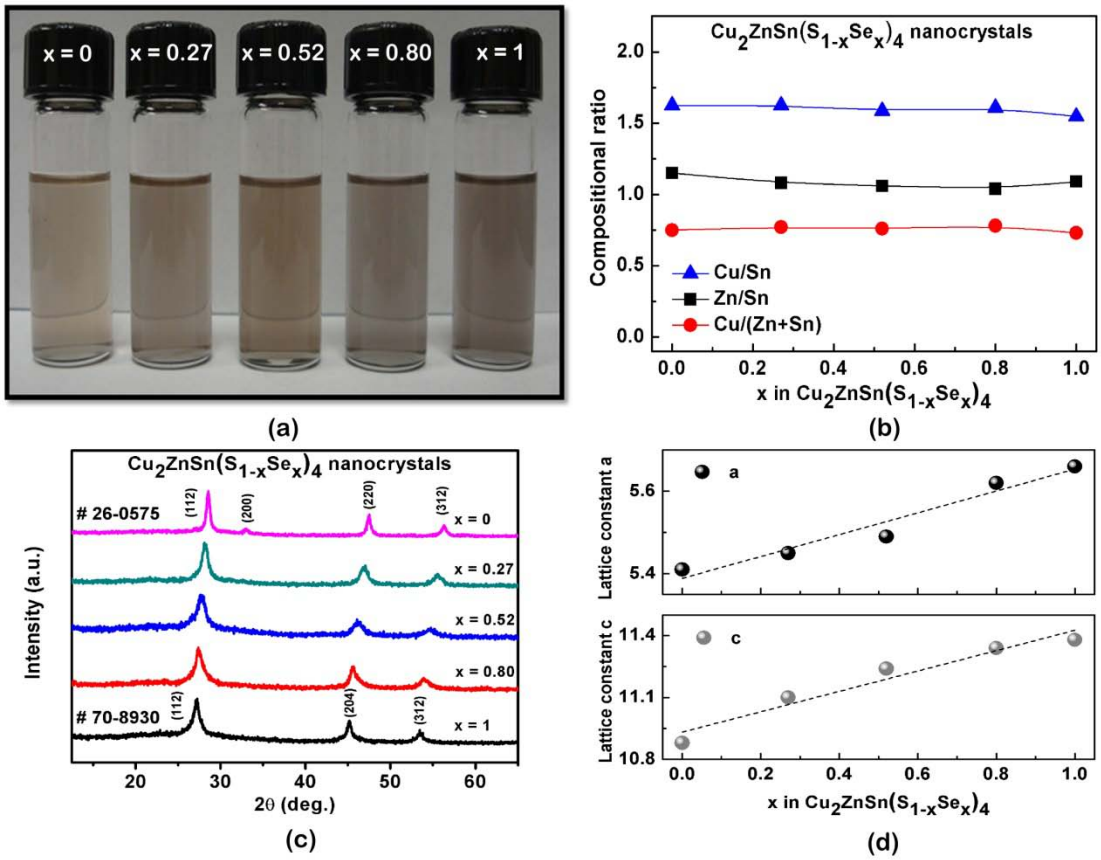

Figure 3.2. (a) Photographs of $Cu_2ZnSn(S_{1-x}Se_x)_4$ nanocrystal solutions with various Se/(S+Se) ratios of x = 0, 0.27, 0.52, 0.80, and 1.0; (b) compositional ratios of Cu/Sn, Zn/Sn, and Cu/(Zn+Sn) as a function of $Cu_2ZnSn(S_{1-x}Se_x)_4$ nanocrystal solution with various Se/(S+Se) ratios of x = 0, 0.27, 0.52, 0.80, and 1.0; (c) XRD analysis of $Cu_2ZnSn(S_{1-x}Se_x)_4$ nanocrystals with various Se/(S+Se) ratios of x = 0, 0.27, 0.52, 0.80, and 1.0; and (d) variations of the lattice constants *a* and *c* with x in the $Cu_2ZnSn(S_{1-x}Se_x)_4$ nanocrystals.

Nanocrystals have been considered a promising precursor to make a spatially uniform film with precisely controlled composition. However, to form a solar cell junction, the heat treatment to promote the grain growth of nanocrystals is necessary to improve carrier transport in as-prepared nanocrystal films. As a result, a series of $Cu_2ZnSn(S_{1-x}Se_x)_4$ followed by a 570 ^oC heat treatment in the presence of sulfur were investigated for realizing the varied morphology of films with increasing content of Se in $Cu_2ZnSn(S_{1-x}Se_x)_4$ nanocrystals.

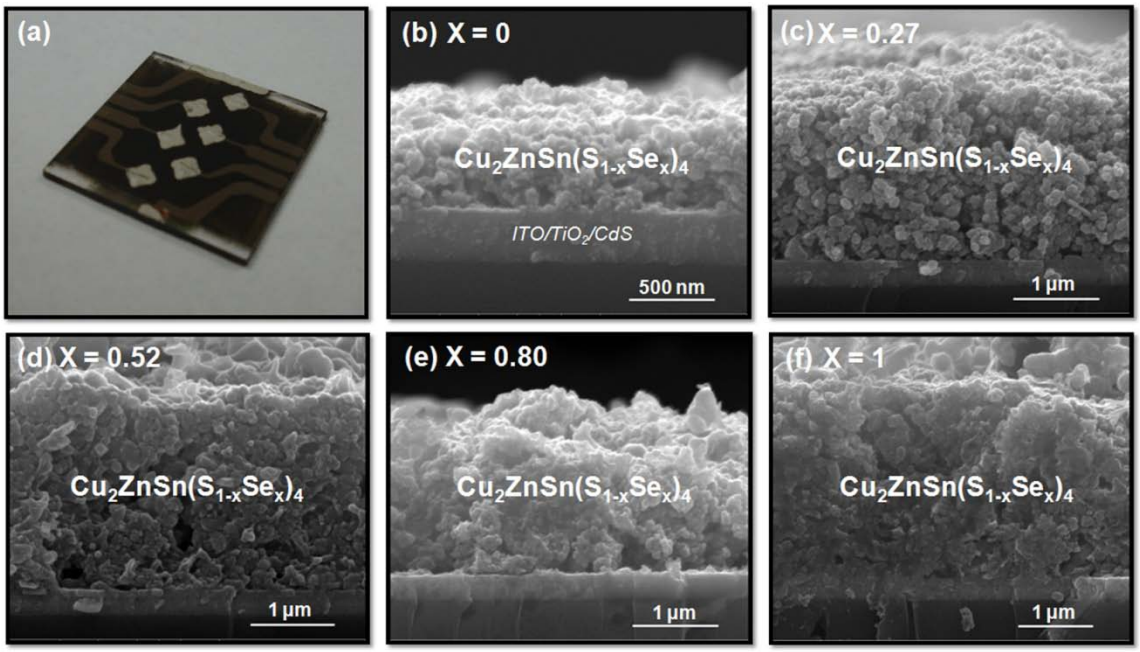

Figure 3.3. (a) Photograph of $Cu_2ZnSn(S_{1-x}Se_x)_4$ solar cells fabricated with our superstrate-type architecture. Cross-sectional SEM images of $Cu_2ZnSn(S_{1-x}Se_x)_4$ nanocrystals with (b) x = 0, (c) x = 0.27, (d) x = 0.52, (e) x = 0.80, and (f) x = 1.0 in the superstrate-type configuration after sulfurization.

The $Cu_2ZnSn(S_{1-x}Se_x)_4$ nanocrystals were incorporated into devices based on the new superstrate-type architecture, $Au/Cu_2ZnSn(S_{1-x}Se_x)_4/CdS/TiO_2/ITO$/soda-lime glass, as depicted in Figure 3.3a. The cross-sectional SEM images of a device stack comprising of the $Cu_2ZnSn(S_{1-x}Se_x)_4/CdS/TiO_2/ITO$/soda-lime glass layers, for a series of x values, are shown in Figure 3.3b-f. The data reveal that the compactness and size of the grains present in the $Cu_2ZnSn(S_{1-x}Se_x)_4$ film after the sulfurization is increased by increasing the Se content in the as-synthesized Cu_2ZnSnS_4 nanocrystals. Compared to the sulfurization of pure $Cu_2ZnSnSe_4$, the image of the as-synthesized Cu_2ZnSnS_4 nanocrystals after the sulfurization treatment revealed relatively small grains, widely distributed over the film, as show in Figure 3.3b, which suggests a slower rate of grain regrowth. This would suggest that the Se content in the as-synthesized Cu_2ZnSnS_4 nanocrystals can assist the grain regrowth of $Cu_2ZnSn(S_{1-x}Se_x)_4$ and benefit the formation of a compact film consisting of larger-size grains, driven by the thermal force of the chemical reaction depicted in equation 2 in presence of S during heat treatment:

$$Cu_2ZnSnSe_4\,(s) + 2\,S_2\,(g) \rightarrow Cu_2ZnSnS_4\,(s) + 2\,Se_2\,(g) \qquad (2)$$

This phenomenon of stimulating the grain regrowth for $Cu_2ZnSnSe_4$ nanocrystals in the presence of sulfur is the same as that for Cu_2ZnSnS_4 nanocrystals in the presence of selenium, which proceeds in the reverse direction to that indicated by equation 2. This suggests that the reaction to produce $Cu_2ZnSn(S,Se)_4$ would follow equation 2 and $Cu_2ZnSn(S,Se)_4$ system can be achieved by adjusting the amount of Se and S in the heat treatment, which agrees well with a similar concept in the $CuIn(S,Se)_2$ system.[114] While varying the amount of sulfur vapor during heat treatment, the S/S+Se ratio could be tuned for producing high quality $Cu_2ZnSn(S,Se)_4$ with an optimal band gap.

In Figure 3.4a, the EDX analysis indicates the compositional ratios in $Cu_2ZnSn(S_{1-x}Se_x)_4$ nanocrystals with various Se/(S+Se) ratios of x = 0, 0.27, 0.52, 0.80, and 1.0 after the 570 ^oC sulfurization for 45 min. Even though there is no consensus for a specific compositional ratio, the expected ranges of desirable compositional ratios have been indicated in Figure 3.4a by different shadow regions. The compositional ratios of Zn/Sn and Cu/(Zn+Sn) for various $Cu_2ZnSn(S_{1-x}Se_x)_4$ nanocrystals are slightly decreased, but the compositional ratio of Cu/Sn in $Cu_2ZnSn(S_{1-x}Se_x)_4$ nanocrystals decreased with increasing the Se content in the $Cu_2ZnSn(S_{1-x}Se_x)_4$ nanocrystals. Furthermore, Figure. 3.4b shows the change in the S/(S+Se) and Cu/Sn compositional ratios for a series of $Cu_2ZnSn(S_{1-x}Se_x)_4$ after the 570 ^oC sulfurization for 45 min. For the change in the S/(S+Se) compositional ratio, we can see that much of the Se in the as-synthesized $Cu_2ZnSn(S_{1-x}Se_x)_4$ nanoparticles has been replaced by S during sulfurization, which suggests the occurrence of reaction 2 in the presence of S during heat treatment. On the other hand, it is found that the $Cu_2ZnSn(S_{1-x}Se_x)_4$ film with x = 0 in Figure 3.3b is relatively thin compared to the others. It can be attributed to the formation of pores accompanying the grain regrowth and induced during the Se-S exchanging process. Since large amount of Se is replaced by gas phase S, it is expected to leave relatively large number of pores in the resulting film, leading to the volume expansion as shown in Figure 3.3c-f. Secondarily, the unit cell volume of $Cu_2ZnSn(S_{1-x}Se_x)_4$ film is varied with the ratio of S to Se due to the larger volume of $Cu_2ZnSnSe_4$ unit cell compared to that of Cu_2ZnSnS_4, which also makes it reasonable to have the $Cu_2ZnSn(S_{1-x}Se_x)_4$ films thick.

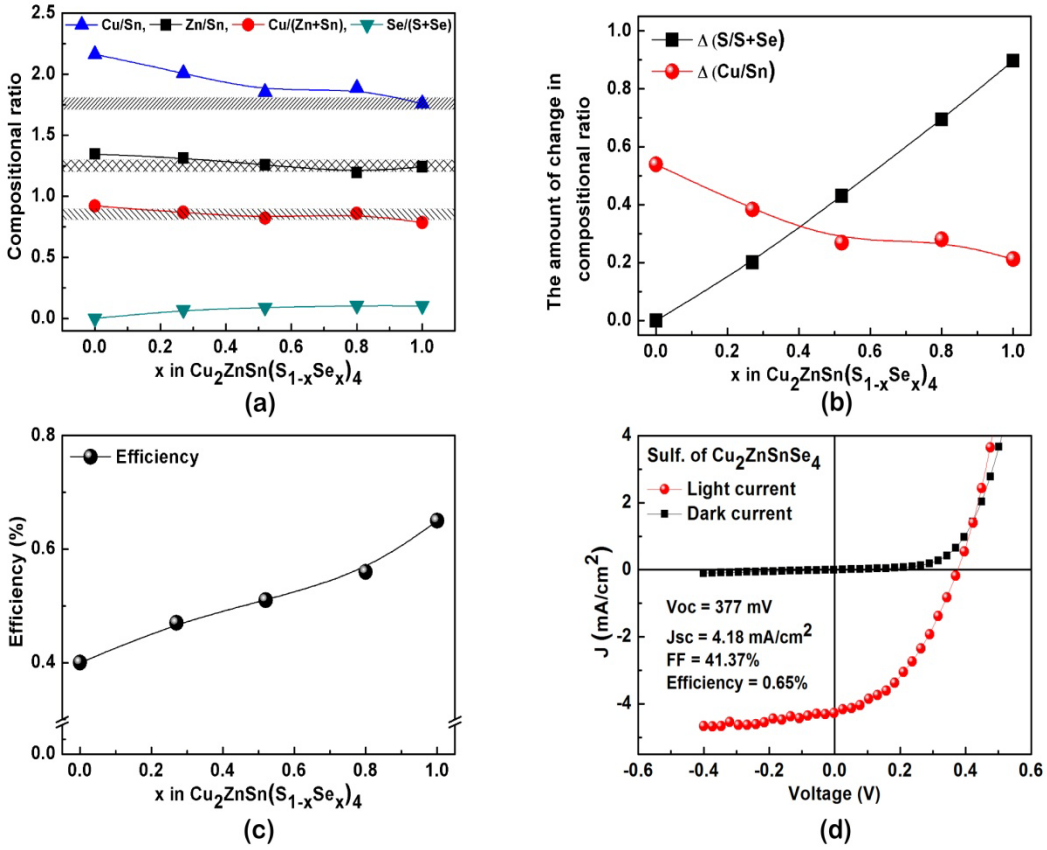

Figure 3.4. (a) compositional ratios of $Cu_2ZnSn(S_{1-x}Se_x)_4$ nanocrystals with various Se/(S+Se) ratios of x = 0, 0.27, 0.52, 0.80, and 1.0 after sulfurization at 570 ^oC for 45 min; (b) change in S/(S+Se) and Cu/Sn compositional ratios in the $Cu_2ZnSn(S_{1-x}Se_x)_4$ nanocrystals with various Se/(S+Se) ratios of x = 0, 0.27, 0.52, 0.80, and 1.0 after sulfurization at 570 ^oC for 45 min; (c) conversion efficiency of superstrate-type configuration using a series of $Cu_2ZnSn(S_{1-x}Se_x)_4$ nanocrystal precursors; and (d) J - V characteristics of the superstrate-type configuration of the $Cu_2ZnSnSe_4$ nanocrystal precursor after sulfurization.

For the change in the Cu/Sn compositional ratio, this implies the progression of the decomposition path of reaction 1, leading to the loss of Sn. On increasing the Se content in the $Cu_2ZnSn(S_{1-x}Se_x)_4$ nanocrystals, the loss of Sn after the sulfurization can be suppressed. This can be explained by the addition of Se into the $Cu_2ZnSn(S_{1-x}Se_x)_4$ nanocrystals, stimulating the grain regrowth by the reaction involving the replacement of Se by S to suppress the decomposition path of reaction 1. Our results indicate the possibility of solving the issue of the secondary phases arising from the loss of Sn if the grain regrowth condition can be further optimized. According to Guo's work,[29] the occurrence of the loss of Sn during the selenization was also revealed. The change of the compositional ratio from the Cu_2ZnSnS_4 nanocrystals (Cu/Sn = 1.37, Cu/(Zn+Sn) = 0.70, Zn/Sn = 0.95) to the $Cu_2ZnSn(S,Se)_4$ resulting film (Cu/Sn = 1.66, Cu/(Zn+Sn) = 0.79, Zn/Sn = 1.11) agrees well with our finding of the loss of Sn in the nanocrystals during the sulfurization.

As a proof-of-concept, the $Cu_2ZnSn(S_{1-x}Se_x)_4$ nanocrystals after the sulfurization process were tested on the superstrate-type configuration of CdS/TiO_2/ITO/soda-lime glass. The solar cells were illuminated through the ITO side of the substrate with a 100 $mWcm^{-2}$ white light illumination under AM 1.5 G conditions for measuring the solar cell current density-voltage (J - V) characteristics. To the best of our knowledge, we are the first group to demonstrate $Cu_2ZnSn(S,Se)_4$ absorbers on the superstrate-type configuration, which serves as a platform for us to investigate the sulfurization of $Cu_2ZnSn(S,Se)_4$ nanocrystals without being influenced by the effect of $Mo(S,Se)_2$ and Na. The conversion efficiencies of superstrate-type configuration with a series of $Cu_2ZnSn(S_{1-x}Se_x)_4$ nanocrystal precursors have also been evaluated as shown in Figure 3.4c. The results suggest that our new device architecture has the ability to become a stable platform to test device performance while varying the properties of materials. An

open-circuit voltage (V_{oc}) of 377 mV, short-circuit current density (J_{sc}) of 4.18 $mAcm^{-2}$, fill factor (FF) of 41.37% for the sulfurization of $Cu_2ZnSnSe_4$ nanocrystals can be extracted from the J - V characteristics under 1 sun (AM 1.5 G) illumination, as shown in Figure 3.4d. Our superstrate-type device structure without using any binder in the ink exhibits comparable V_{oc} and FF to the typical substrate-type device structure, when compared to the reported efficiencies of $Cu_2ZnSn(S,Se)_4$ nanocrystal-based absorber as listed in Table 3.1. When combining the results of Figure 3.4c with Figure 3.4a, we see that relatively higher conversion efficiency can be achieved only when the compositional ratios are closer to the expected ranges of desirable compositional ratios. The relatively high efficiency of the solar cell is due to a compact film with larger grain size, as shown in Figure 3.3f, and lower loss of Sn, as shown in Figure 3.4b, with increasing Se content in the $Cu_2ZnSn(S_{1-x}Se_x)_4$ nanocrystals. However, the limitation of our device efficiency mainly by a relatively lower short-circuit current density could be attributed to the resulting $Cu_2ZnSn(S,Se)_4$ film consisting of relatively high porosity and roughness even after sulfurization, which are likely to increase charge trapping and recombination. Such defects could be mitigated by modifying the coating technique, such as adjusting the concentration of ink or adopting different organic solvents like alkanethiol to fabricate a robust precursor film.[29]

In addition, it has been reported that the preferred dominant defects of $Cu_2ZnSn(S,Se)_4$ consists of V_{Cu} shallow acceptors. However, undesirable Cu_{Zn} deep acceptors tend to occur most of the time.[115] Besides, the increase in S content in the resulting $Cu_2ZnSn(S,Se)_4$ film is likely to have higher defect density, resulting in stronger recombination.[116] This suggests that optimizing the band gap by tuning the ratio of S to Se is beneficial for producing higher efficiency devices in our system. Our

$Cu_2ZnSn(S,Se)_4$ film with x = 1.0 after sulfurization shows S-rich $Cu_2ZnSn(S,Se)_4$ with the Se/S+Se ratio of around 0.1, as shown in Figure 3.4a.

Table 3.1. Reported efficiencies of $Cu_2ZnSn(S,Se)_4$ nanocrystal-based absorbers.[27-29, 117]

Device structure	V_{oc} (mV)	J_{sc} (mA cm^{-2})	FF (%)	Eff. (%)
Glass/Mo/CZTSSe/CdS/ZnO/ITO	420	30.4	52.7	6.73
Glass/Mo/CZTSSe/CdS/ZnO/ ITO	210	11.5	33.1	0.80
Glass/Au/CZTS/CdS/ZnO/ITO	321	1.95	37.0	0.23
Glass/ITO/TiO_2/CdS/CZTSSe/Au	377	4.18	41.3	0.65

This suggests that the conversion efficiency can further be raised by fabricating Se-rich $Cu_2ZnSn(S,Se)_4$ films by reducing the replaced amount of Se by S, which could be achieved by varying the amount of sulfur vapor during the heat treatment.[16] As a result, it could reasonably be expected that the efficiency for the sulfurization of $Cu_2ZnSnSe_4$ in our supstrate-type configuration could be further enhanced by fabricating a robust precursor film and optimizing the Se/S+Se ratio in the $Cu_2ZnSn(S,Se)_4$ film.

3.4 CONCLUSIONS

In conclusion, we have demonstrated Cu-poor and Zn-rich $Cu_2ZnSn(S_{1-x}Se_x)_4$ nanocrystals with varying S to Se ratios, synthesized and altered by a facile hot-injection approach using only the oleylamine reagent. The evolution of $Cu_2ZnSn(S_{1-x}Se_x)_4$ nanocrystals to $Cu_2ZnSn(S_{1-x}Se_x)_4$ film was investigated for the first time via tuning the ratio of Se to S in $Cu_2ZnSn(S_{1-x}Se_x)_4$ nanocrystals followed by a sulfurization step. It was

found that minimizing the possibility for the loss of Sn during the heat treatment and producing a compact film with large grain size are beneficial for the device performance. Accordingly, a novel low-cost superstrate-type device architecture has been demonstrated offering an opportunity for the $Cu_2ZnSn(S,Se)_4$ system to circumvent challenges in the existing substrate-type architecture, such as decomposition of $Cu_2ZnSn(S,Se)_4$ and a possible Schottky barrier at the $Mo/Cu_2ZnSn(S,Se)_4$ interface.

Chapter 4: Low-cost CZTSSe solar cells fabricated with low band gap CZTSe nanocrystals, environmentally friendly binder, and non-vacuum processes†

4.1 INTRODUCTION

Colloidal semiconductor nanocrystals have been one of the promising solutions to achieve the ultimate goal of low-cost, high-efficiency solar cells due to the advantages of efficient utilization of materials, excellent capability for precisely controlled compositions, and large-scale manufacturing processes.[1] Recently, successful application of semiconductor nanocrystals such as CdTe, CIGS, and PbS to photovoltaic devices has been demonstrated to assure their potential.[118-120] However, with the targeted deployment of solar cells reaching the terawatt scale, those materials adopting the rare or unfriendly elements would become a crucial issue.[121] The environmentally benign and earth abundant kesterite-related Cu_2ZnSnS_4 (CZTS), $Cu_2ZnSn(S_{1-x}Se_x)_4$ (CZTSSe), and $Cu_2ZnSnSe_4$ (CZTSe) materials with high absorption coefficients become promising absorbent candidates for the next generation solar cells to meet the terawatt scale solar demand.[7, 122] Recently, many efforts have been made with the syntheses of CZTS, CZTSe, and CZTSSe nanocrystals.[27, 112] However, it is challenging to make high quality films to promote the transport of electron and hole for producing high-efficiency p-n junction solar devices.

An efficiency of 0.8% was demonstrated using CZTS nanocrystals followed by a selenization process, and such an approach has become a prevailing route for making CZTSSe solar cells.[28] With further improvements in coating the film by adopting hexanethiol solvent, a higher efficiency of 6.73% has been achieved by the same group.[29]

† C.-L. Wang and A. Manthiram, "Low-cost CZTSSe solar cells fabricated with low band gap CZTSe nanocrystals, environmentally friendly binder, and non-vacuum processes," *ACS Sustainable Chemistry & Engineering* 2, 561-568 (2014). C.-L. Wang carried out the experimental work. Dr. A. Manthiram supervised the project.

However, the utilization of toxic and unfriendly solvents such as toluene or hexanethiol to disperse the nanocrystals is not environmental friendly. Unfortunately, only a few studies have focused on green and sustainable solvents for preparing the CZTSSe nanocrystal-based ink. Simultaneously, the typical selenization process by inefficiently using a large amount of rare Se element (with only 0.05 ppm in the earth's crust) during heat treatment makes it challenging to meet the terawatt scale demand of solar cells.[123] In addition, the active Se during heat treatment not only easily creates an unwanted layer of $MoSe_2$ at the interface but also causes undesirable effects on the device performance, leading to difficulties in controlling the manufacturing process.[106] In contrast to the traditional route for CZTSSe involving the inefficient and harsh chemical reaction processes associated with Se, an alternative route for CZTSSe involving the sulfurization of the fabricated precursor CZTSe nanocrystals with the abundant and mild S element could enhance the commercial viability of CZTSSe solar cells. Unfortunately, only few studies have focused on this route.

Accordingly, we demonstrate here a new route to make the CZTSSe films by using the low band gap CZTSe nanocrystals, synthesized by a hot-injection approach, followed by a sulfurization process. The effect of S doping into CZTSe nanocrystals during heat treatment is also investigated by varying the sulfurization temperature from 480 to 570 °C. Furthermore, ethyl cellulose, which can replace the toxic and unfriendly solvent of toluene or hexanethiol, is used as a binder in the film preparation process with CZTSe nanocrystals. In order to investigate the role of ethyl cellulose in the evolution of nanocrystals into films, a low-cost superstrate-type substrate is adopted to evaluate the conversion efficiency.

4.2 EXPERIMENTAL

4.2.1 Synthesis of $Cu_2ZnSnSe_4$ nanocrystals

The CZTSe nanocrystals were produced by a hot-injection approach. Cationic precursors of Cu, Zn, and Sn were selected from copper(II) acetylacetonate [$Cu(acac)_2$], zinc acetate [$Zn(O_2CCH_3)_2$], and tin(II) chloride dihydrate [$SnCl_2.2H_2O$], respectively. In a typical synthesis, a mixed solution of 1.61 mmol of copper(II) acetylacetonate, 1.3 mmol of zinc acetate, and 1.0 mmol of tin(II) chloride dehydrate with 30 mL of oleylamine was heated up first. A 10 mL of oleylamine solution with elemental Se was injected into the mixed solution at 200 ^oC. Then, the solution mixture was heated to 250 ^oC with a holding time of 1 h. After cooling to room temperature, the product was precipitated into methanol and washed with isopropyl alcohol/hexane three times to remove the residual oleylamine.

4.2.2 Fabrication of solar devices

The conversion efficiency of the solar devices was examined with a low-cost and $Mo(S,Se)_2$-free superstrate-type substrate of CdS/TiO_2/ITO/soda-lime glass with a layer (30 nm) of anatase TiO_2 synthesized by a sol-gel method at 450 ^oC and a buffer layer (100 nm) of CdS prepared by a chemical bath deposition (CBD) method at 65 ^oC on a commercial ITO substrate, purchased from Nanocs (Product No. ITO-0021-50).[117] No antireflectance coating of MgF_2 was used. A gold electrode prepared by a thermal evaporator was used to define an active area of 0.1 cm^2. The heating filament was loaded with a high-purity gold wire with 0.5 mm in diameter and 5 cm in length. Two inks were prepared for the spin-coating process. Although the nanocrystals could be well dispersed in a nonpolar solvent, the toxicity or high volatility of most of the nonpolar solvents make

it challenging to prepare a scalable and uniform film with the spin-coating process. Therefore, the environmentally friendly and safe solvent ethanol with relatively low volatility was chosen for the spin-coating process. Besides, in order to investigate the effect of the binder on the ink, ethyl cellulose with more than 46-48 % ethoxyl groups that freely dissolve in ethanol was used. The first ink was prepared by dispersing 10 mg of CZTSe in 0.8 mL of ethanol by ultrasonication for 20 min. The other ink was prepared by dispersing 10 mg of CZTSe in a premixed solution of 0.8 mL of ethanol with 0.3 mg of ethyl cellulose by ultrasonication for 20 min. After spin-coating onto the superstrate-type substrate, the as-prepared film (ink without ethyl cellulose) and the composite film (ink with ethyl cellulose) were treated by a sulfurization process from 480 to 570 ^{o}C for 45 minutes. The sulfurization process was performed by placing the samples in a graphite box with sulfur powder under an argon flow. Once the tubular furnace was preheated to a desirable temperature, the whole graphite box was immediately moved to the heating region to provide a fast ramping rate and mitigate the effect of potential diffusion at the interface. An etching process with dilute HCl (hydrochloric acid) solution was applied before thermally depositing the gold back contact.[124]

4.2.3 Characterization of Materials

The CZTSe sample was characterized with a Philips X-ray diffractometer (XRD) with Cu Kα radiation. The band gap of CZTSe was determined by a Cary 5000 UV-Vis-NIR equipment. The CZTSe nanocrystals dispersed in hexane were used for UV- Vis absorption measurement to avoid the extra signals from those dispersed in a premixed solution of ethanol and ethyl cellulose. The Raman spectra were acquired with a Renishaw inVia Raman Microscope using 532 nm laser excitation at a 50 X objective.

The in-plane and cross-sectional images were collected with a FEI Quanta 650 scanning electron microscope (SEM). The compositional analyses collected with energy-dispersive X-ray spectroscopy (EDS) were carried out with a JEOL5610 SEM. Thermogravimetric analysis (TGA) was performed with a Perkin Elmer TGA 7 with 5 ^{o}C per minute heating rate under a flow of argon. The current density-voltage (J - V) characteristics under air mass 1.5 global (AM 1.5 G) conditions with a solar simulator using a 100 mWcm^{-2} light illumination were measured with a Keithley 2400 equipment. The conversion efficiencies of all solar cells based on a superatrate-type substrate were assessed with the light illuminating into the ITO side of the substrate. Silver paste was used to reduce the contact resistance between ITO and the wire.

4.3 RESULTS AND DISCUSSION

Figure 4.1a shows the X-ray diffraction (XRD) pattern of the as-synthesized CZTSe nanocrystals, which matches well with all the diffraction peaks in the Joint Committee on Powder Diffraction Standards (JCPDS) card 52-0868. The CZTSe unit cell has lattice constants of a = 5.64 Å and c = 11.20 Å with a volume of 356.26 Å^3, which is larger than the 319.50 Å^3 of CZTS because of the larger radius of Se (0.198 nm) compared to that of S (0.184 nm). According to the Debye-Scherrer analysis, the as-synthesized CZTSe nanocrystals have an average crystallite size of 20 nm. Raman spectroscopic analysis in Figure 4.1b also indicates that the as-synthesized nanocrystals can be identified with the main peaks of 196 and 231 cm^{-1} in CZTSe crystallite structure. A small deviation between 193 and 196 cm^{-1} may be attributed to the uneven surface scattering. Furthermore, Figure 4.1c shows the absorbance of as-synthesized CZTSe nanocrystals as a function of the wavelength. It can be found that the CZTSe nanocrystals

possess a low energy band gap of 1.05 eV, as determined from the UV- vis absorption spectrum, shown in the upper inset of Figure 4.1c, which is consistent with the previous literature.[125]

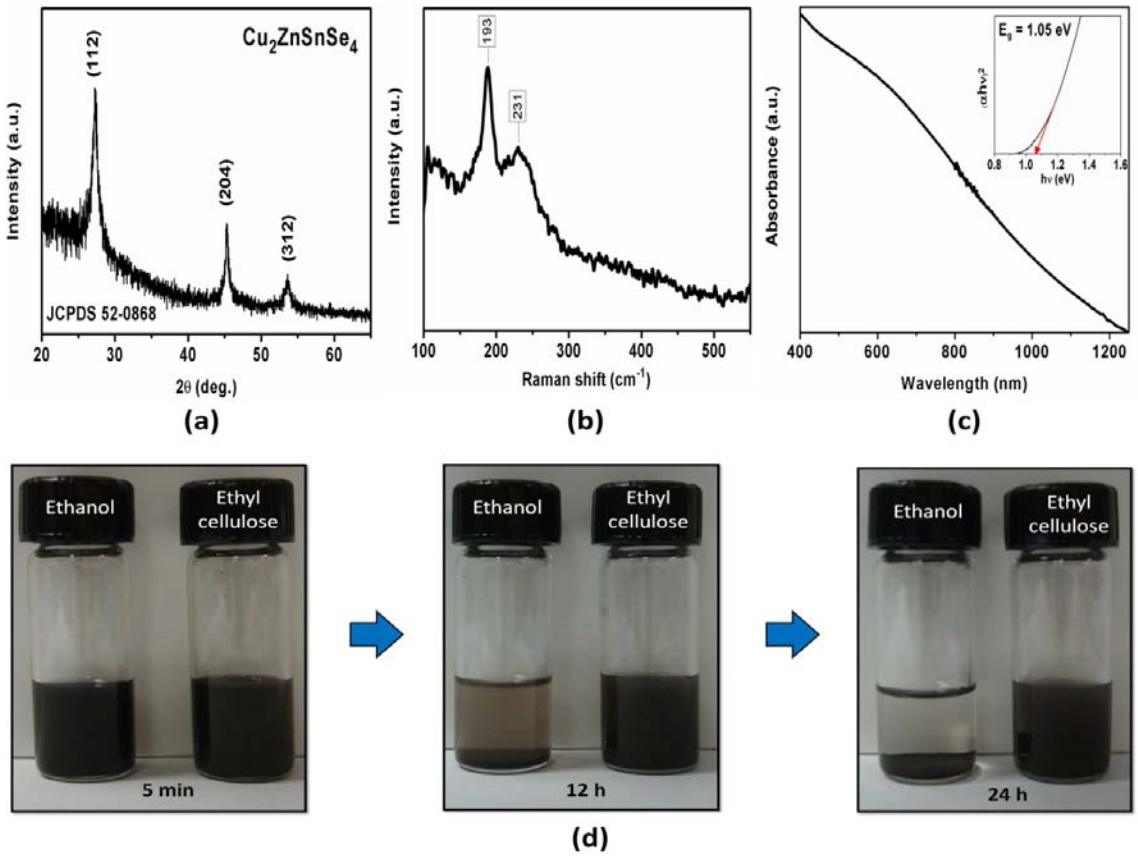

Figure 4.1. (a) XRD patterns of as-synthesized CZTSe nanocrystals, (b) Raman spectroscopic analyses of as-synthesized CZTSe nanocrystals, (c) UV-Vis absorption spectrum of as-synthesized CZTSe nanocrystals, and (d) color of the vial containing the CZTSe nanocrystals dispersed in ethanol with and without ethyl cellulose after the standing for a period of 5 min, 12 h, and 24 h. The inset in (c) shows a band gap of 1.05 eV for the as-synthesized CZTSe nanocrystals, determined by a plot of $(\alpha h\upsilon)^2$ as a function of $h\upsilon$.

These analyses show that a single phase of CZTSe nanocrystals with a low energy band gap of 1.05 eV has been synthesized by the hot-injection approach. In addition, in order to compensate for the potential loss of Sn during heat treatment, the as-synthesized CZTSe nanocrystals with cation ratios of Zn/Sn = 0.99 and Cu/(Zn+Sn) = 0.72, analyzed by EDS, is suitable for fabricating Cu-poor and Zn-rich CZTSSe solar cells. In addition, the effect of ethyl cellulose on CZTSe nanocrystals was evaluated by dispersing the nanocrystals in ethanol with and without ethyl cellulose as shown in Figure 4.1d. After a period of 12 h, the middle segment in Figure 4.1d shows that some of the nanoparticles dispersed in ethanol have settled at the bottom compared to that dispersed in ethanol with ethyl cellulose. After a period of 24 h, the color of the supernatant liquid in the vial with the nanoparticles dispersed in ethanol has become almost clear as seen in the right segment of Figure 4.1d because all the nanocrystals have settled at the bottom. In contrast, the color of the dispersion in ethanol with ethyl cellulose remains black, indicating the beneficial role played by ethyl cellulose for producing a stable ink.

Figure 4.2 shows the SEM images of the as-prepared CZTSe films with or without ethyl cellulose after the sulfurization treatment. The morphology of the CZTSSe film with the use of ethyl cellulose after sulfurization at 480 ^{o}C in Figure 4.2a shows a feature of better grains in comparison to the film obtained without using ethyl cellulose in Figure 4.2b. Besides, the cross-sectional SEM images indicate the film using ethyl cellulose shows larger grain size at 550 ^{o}C in Figure 4.2c, as compared to that without ethyl cellulose at 570 ^{o}C in Figure 4.2d. Such induced grain growth at a relatively low temperature for the film with the aid of ethyl cellulose could be attributed to the bridging together of the CZTSe nanocrystals by the polymer, leading to the precursor film with a higher packing density beneficial for the grain growth.

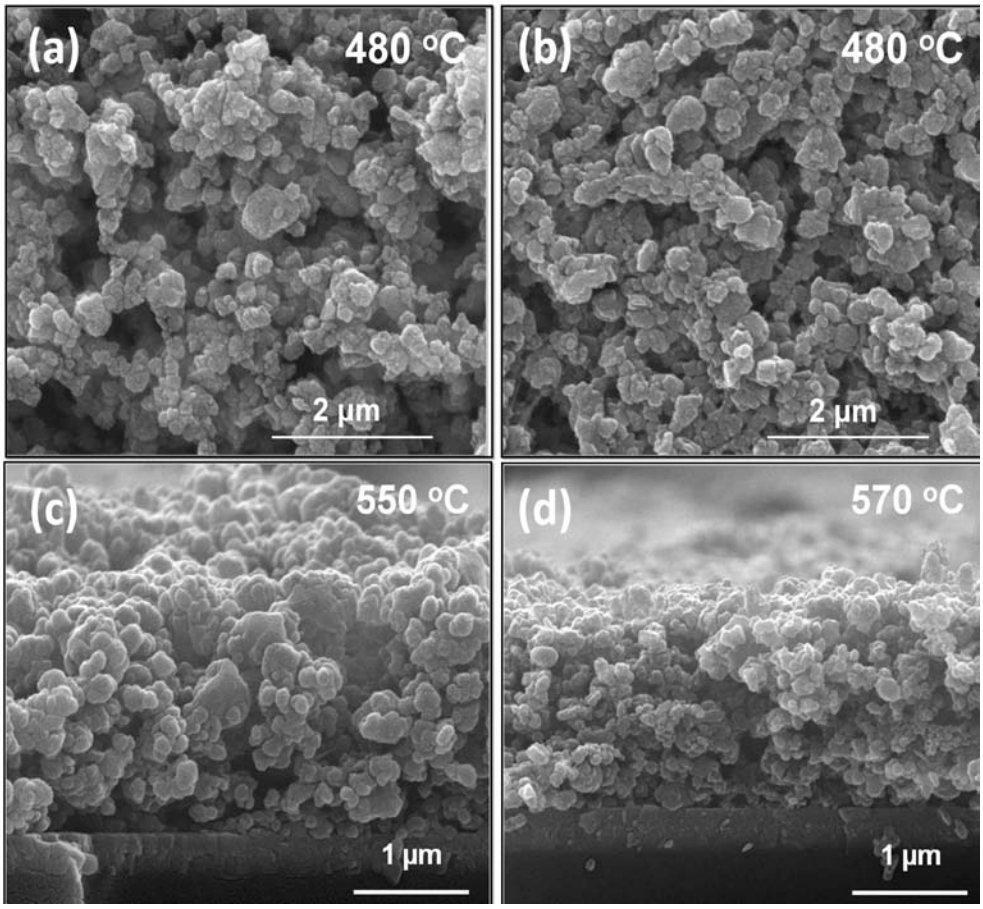

Figure 4.2. Plane-view SEM images of CZTSe nanocrystals (a) with ethyl cellulose and (b) without ethyl cellulose after sulfurization at 480 °C. Cross-sectional SEM images of CZTSe nanocrystals (c) with ethyl cellulose after sulfurization at 550 °C and (d) without ethyl cellulose after sulfurization at 570 °C.

In order to further understand the role of ethyl cellulose during the sulfurization treatment, TGA experiment was carried out. Figure 4.3a shows the weight loss of the ethyl cellulose with temperature. As seen, the 1st decomposition of ethyl cellulose begins at about 150 ^{o}C, the 2nd weight loss occurs at about 300 °C, and < 1 % weight of ethyl cellulose remains when the temperature is above 410 ^{o}C. It indicates that ethyl cellulose possesses the inherent properties of low ash and easy removal, which is suitable for the additive binder in the ink. However, it has been reported that the existence of large amount of residual amorphous carbon layer at the bottom interface between Mo and $CuInSe_2$ (CIS) causes a negative effect on the device performance while adding the polymer as a viscosity controlling agent in the typical metal salts ink to prepare CIS absorbent films.[126, 127] Such problems can be understood by considering that the decomposition path of ethyl cellulose after the heat treatment may be hindered by the upper dense layer with the early formation of CIS crystallite film, which results in a double-layer structure consisting of the incomplete removal of ethyl cellulose left at the bottom of the resulting film and the crystallite film at the top. As compared to the film prepared by the typical metal salts ink, our film prepared by nanocrystals-based ink with the ethyl cellulose additive shows a single-layer structure without residual carbon layer at the interface between CZTSSe and CdS, as shown in Figure 4.3b, which indicates all the carbon from the ethyl cellulose could be effectively removed through the existence of pores between the nanocrystals. Thus, it can be found in Figure 4.3c and d, which were obtained with our nanocrystal ink without and with ethyl cellulose after sulfurization at 480 ^{o}C, that both show microstructures consisting of pores.

Furthermore, the EDS analysis, as shown in Figure 4.3e, indicates the amount of S doped into the film (or the change in the compositional ratios of S/(S+Se)) without and with ethyl cellulose as a function of sulfurization temperature. The sulfurization process

was carried out by placing the samples with 2 mg sulfur powder in a graphite box with a volume of 6.25 cm^3 under argon flow. The approximate pressure of S vapor during heat treatment as a function of temperature is also shown in Figure 4.3e, all of which are higher than the required value to stabilize the formation of CZTS.[101] Although the pressure of S vapor increases with temperature, the observation of a nearly constant ratio of the change of S/(S+Se) around 0.6 in a large range of 480 to 570 ^oC would suggest that the amount of S doped into the CZTSe can be controlled during the sulfurization process. Besides, it can be found that the amount of S doped into the CZTSe can be tuned from $\Delta S/(S+Se) = 0.89$ (Figure 3.4a) to around 0.6 by reducing 10 mg to 2 mg sulfur powder in a graphite box.

Such a doping path by replacing Se in CZTSe by S in the sulfurization can be referred to the following reaction:

$$Cu_2ZnSnSe_4\,(s) + 2\,S_2\,(g) \rightarrow Cu_2ZnSnS_4\,(s) + 2\,Se_2\,(g)$$

Additionally, the role played by ethyl cellulose on the film quality during the grain growth process was further investigated and understood via the compositional change. In Figure 4.3f, the EDS analysis indicates the compositional change in Sn/Cu ratio as a function of the sulfurization temperature for the films with or without ethyl cellulose. The film without ethyl cellulose shows significant variations of the change in Sn/Cu ratio, while that with ethyl cellulose shows minor variations, indicating that ethyl cellulose can suppress the loss of Sn. Nevertheless, in order to understand the reaction pathway associated with the loss of Sn during the grain growth process, Raman spectroscopy was utilized for characterizing the CZTSSe film after the sulfurization. It is known that the major Raman peaks of pure CZTSe at 196 cm^{-1} and pure CZTS at 338 cm^{-}

^{1} are attributed to the A_1 anion vibration mode of the lattice, which corresponds to the vibration of Se (and S) relative to the fixed surrounding atoms. Such a variation in the major A_1 mode vibration with increasing ratio of Se to S leads to Raman shifts towards a smaller wave number while Se atoms are incorporated into CZTS at different levels. A bimodal behavior with major peaks shifting to the location between 196 cm^{-1} and 338 cm^{-1} is usually observed.[128]

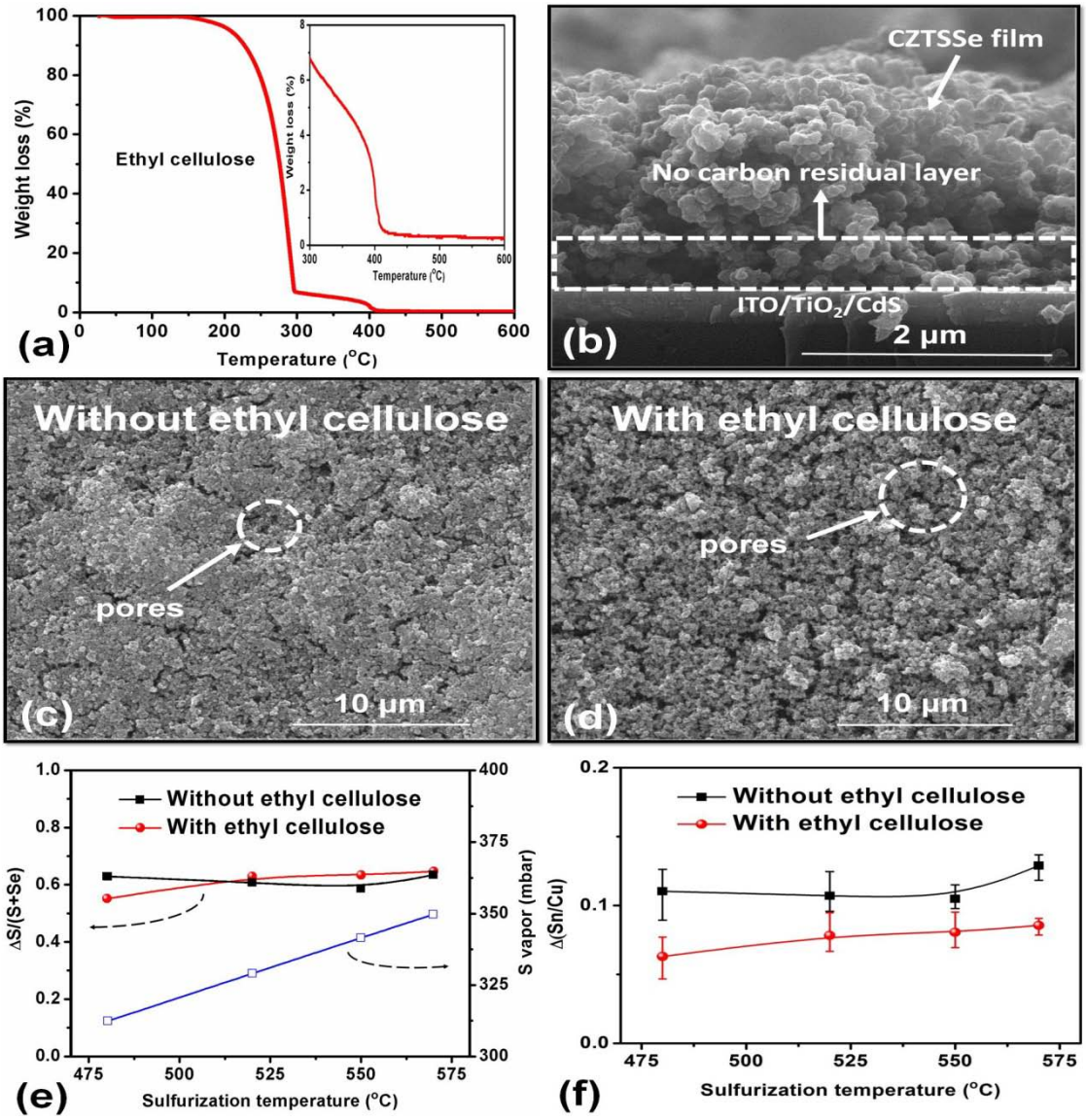

Figure 4.3. (a) TGA plots of ethyl cellulose and (b) cross-sectional SEM images of CZTSe nanocrystals with ethyl cellulose after sulfurization at 480 °C. Low magnification plane-view SEM images of CZTSe nanocrystals (c) without ethyl cellulose and (d) with ethyl cellulose after sulfurization at 480 °C. Changes in the compositional ratios of (e) S/(S+Se) and (f) Sn/Cu in the CZTSe nanocrystals as a function of sulfurization temperature.

Figure 4.4a (and b) shows the Raman analyses of devices obtained without (and with) using ethyl cellulose as a function of sulfurization temperature from 480 to 570 ^{o}C. As seen, shifting of two major peaks occurs, from 213 cm^{-1} (209 cm^{-1}) and 324 cm^{-1}(323 cm^{-1}) to 216 cm^{-1} (216 cm^{-1}) and 325 cm^{-1}(325 cm^{-1}), which are attributed to the change in the lattice vibrations on incorporating S into CZTSe. Besides, the XRD analysis of the CZTSSe devices with and without ethyl cellulose after sulfurization at 550 ^{o}C, as shown in Figure 4.5, indicates that the three main diffraction peaks of CZTSe also shift to higher angles due to the replacement of larger Se (0.198 nm) by smaller S (0.184 nm) during the sulfurization process, which is consistent with the peak shifts in the Raman analysis. These results are consistent with previous studies, showing the shifts in the XRD peaks and in the two Raman peaks of CZTSSe with the ratio of S/(S+Se) (210 and 329 cm^{-1} for S/(S+Se) = 0.4).[7]

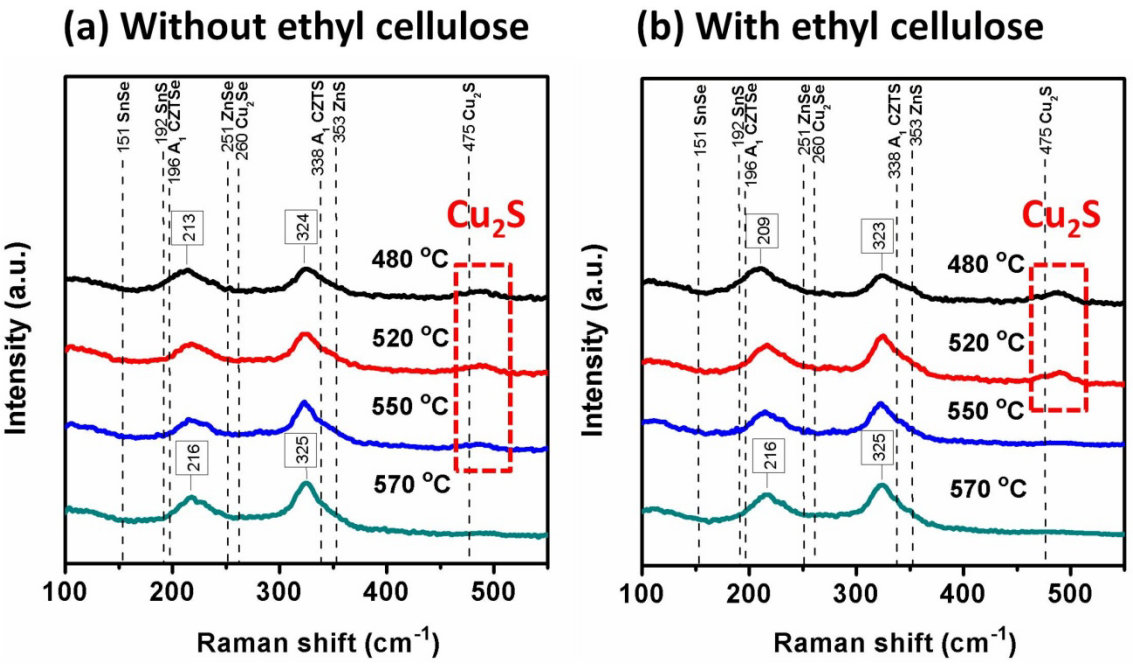

Figure 4.4. Raman spectroscopic analyses of the CZTSSe films fabricated with the CZTSe nanocrystals (a) without ethyl cellulose and (b) with ethyl cellulose as a function of sulfurization temperature. Raman peak locations of the compounds can be found in the literature. [7, 128-132]

However, a weak peak at 490 cm^{-1} corresponding to Cu_2S in the Raman spectrum of Figure 4.4a, which cannot be detected by XRD, is found from the sulfurization temperature of 480 to 550 ^oC, which then disappeared after 570 ^oC. This indicates that a Cu_2S secondary phase forms in the film when no ethyl cellulose is used and it exists during the grain growth process until the sulfurization temperature of 570 ^oC is reached. On the other hand, Figure 4.4b reveals that the 490 cm^{-1} peak corresponding to Cu_2S disappeared after the sulfurization temperature of 550 ^oC when ethyl cellulose is used. This finding is similar to Mainz *et al.*'s work associated with the selenization process of CZTS nanocrystals that tend to form copper selenide by an initial intermediate separation

of the cations at the surface, followed by the diffusion of Zn and Sn to form CZTSSe.[133] As a result, the lower loss of Sn from the film with ethyl cellulose than that without ethyl cellulose, as recognized from Figure 4.3f, can be explained to be due to a high packing density of the film to facilitate the diffusion of Zn and Sn to convert into CZTSSe. On the contrary, the film without ethyl cellulose is more prone to the evaporation of Sn(S,Se) gas phase before compiling together, leading to a large amount of Sn loss from the film. Once the loss of Sn is too large, not only the desirable composition of CZTSSe with Cu-poor and Zn-rich condition cannot be realized, but also the removal of the unwanted $Cu_2(S,Se)$ become difficult. No detectable Raman peak of Zn(S,Se) may be attributed to the removal of Zn-rich compounds during the HCl etching process.[124]

In order to investigate the effectiveness of our route, the conversion efficiencies of CZTSSe solar devices prepared with the CZTSe nanocrystals with and without ethyl cellulose as a function of sulfurization temperature were evaluated. With increasing sulfurization temperature, not only V_{oc} in Figure 4.6a but also J_{sc} in Figure 4.6b for the devices with and without ethyl cellulose can be raised. Such enhancement of V_{oc} and J_{sc} can be attributed to the reduced defects of CZTSSe during the grain growth process.

On the other hand, it is worth noting that Figure 4.6c shows that the values of FF for the films without ethyl cellulose decrease with increasing sulfurization temperature, but those with ethyl cellulose are much higher than those without ethyl cellulose at higher temperature. It can be explained that the ethyl cellulose additive in the CZTSSe film could not only effectively improve the film quality by promoting the grain growth as suggested by Figure 4.2 but also suppress the Cu_2S phase by mitigating the loss of Sn as explained by Figure 4.4b. Furthermore, as compared to the previous reports showing low FF (~35%) with ethyl cellulose,[126, 127] our device using ethyl cellulose with a higher FF (>40%) may be attributed to the complete removal of ethyl cellulose as shown in Figure

4.3b.[134] As a result, it is believed that the ethyl cellulose additive in the nanocrystal-based ink would play a crucial role in tuning the CZTSSe film quality during the sulfurization treatment.

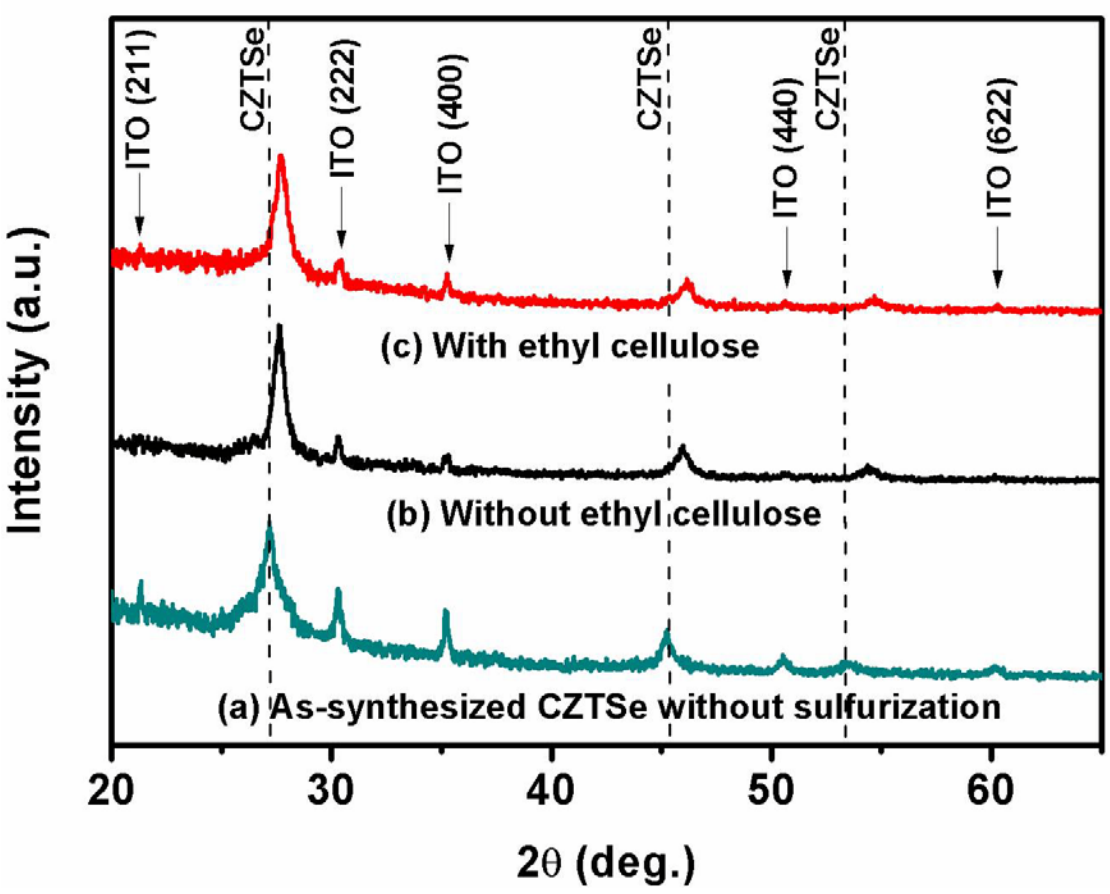

Figure 4.5. XRD patterns of (a) as-prepared CZTSe nanocrystals, and CZTSe nanocrystals (b) without ethyl cellulose and (c) with ethyl cellulose after the sulfurization at 550 ^{o}C on a superstrate-type substrate of CdS/TiO_2/ITO/soda-lime glass.

Figure 4.6d illustrates the conversion efficiency of solar devices with and without using ethyl cellulose as a function of sulfurization temperature. It shows that doubling of the conversion efficiency can be achieved by increasing the temperature from 480 to 570 ^{o}C for both cases with and without ethyl cellulose, demonstrating that the modification of CZTSe nanocrystals by sulfurization treatment is applicable for promoting the quality of CZTSSe film. Besides, the efficiency of the device with ethyl cellulose is higher than that without ethyl cellulose after the sulfurization at 520 ^{o}C, which can be attributed to the removal of ethyl cellulose from the film. Figure 4.6e shows that our preliminary conversion efficiency of 1.11% with a V_{oc} of 363 mV, J_{sc} of 6.83 mAcm^{-2}, and FF of 44.72% has been achieved by using CZTSe nanocrystals and the ethyl cellulose binder after the sulfurization process at 550 ^{o}C, compared to an efficiency of 1.00% with a V_{oc} of 353 mV, J_{sc} of 7.75 mAcm^{-2}, and FF of 36.66% without using ethyl cellulose binder after the sulfurization process at 570 ^{o}C. (The error bar in efficiency is estimated to be ±0.02%) Such an improvement of 11% in the conversion efficiency can be attributed to the prevention of the unwanted Cu_2S secondary phase from the film at a lower sulfurization temperature of 550 ^{o}C by using ethyl cellulose.

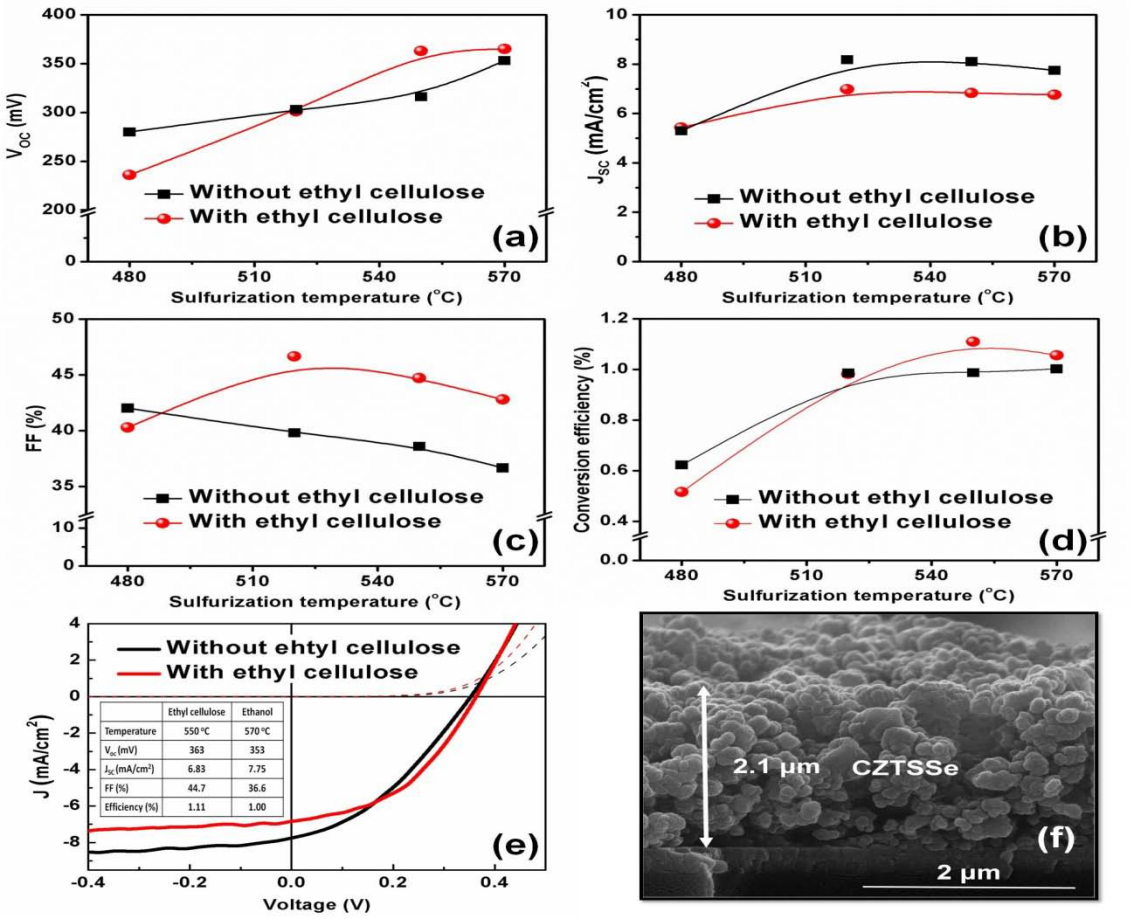

Figure 4.6. (a) V_{oc} of CZTSe nanocrystals with and without ethyl cellulose as a function of sulfurization temperature. (b) J_{sc} of CZTSe nanocrystals with and without ethyl cellulose as a function of sulfurization temperature. (c) FF of CZTSe nanocrystals with and without ethyl cellulose as a function of sulfurization temperature. (d) Conversion efficiency of CZTSe nanocrystals with and without ethyl cellulose as a function of sulfurization temperature. (e) J - V characteristics of CZTSSe solar device with ethyl cellulose after sulfurization at 550 ^{o}C as marked by red line and without ethyl cellulose after sulfurization at 570 ^{o}C as marked by black line. The dashed lines correspond to the dark J - V curves. (f) Cross-sectional SEM image of CZTSe nanocrystals with ethyl cellulose after sulfurization at 550 ^{o}C.

Table 4.1 summarizes all reported efficiencies for CZTSSe fabricated by nanocrystal-based approaches. Compared to the previous work on CZTSSe fabricated by CZTS nanoparticles (without using malodorous hexanethiol) followed by a selenization process on the typical Mo substrate structure, our efficiency of 1% with a superstrate-type substrate shows its promise with the comparable values of FF = 36.66% and V_{oc} = 353 mV. The increase in the conversion efficiency of the superstrate-type devices with the sulfurization temperature from 480 to 570 ^{o}C (Figure 4.6d) could suggest that the effect of the diffusion of CdS into the absorbent layer appear minor, even though the small amount of the diffusion of Cd into CZTSSe slightly increases with the sulfurization temperature as shown in Figure 4.7a. It can explain the existence of the Cd_{Cu} defect via the diffusion of Cd into CZTSe to form the embedded n-type layer at the interface, which is beneficial for the device performance.[135] Furthermore, our fabrication method using CZTSe nanocrystals as the initial precursor also tends to mitigate the interdiffusion between CdS and the absorbent layer due to the relatively strong bonding between atoms in the crystallite structure, which differs from the previous post-annealing or co-evaporation approaches by using active metal or elemental gases as the initial precursors.[136, 137] On the other hand, the diffusion of Ti and In into CZTSSe cannot be detected as shown, respectively, in Figures 4.7b and 4.7c. It indicates that TiO_2 film in the superstrate-type substrate is sufficient to block not only the diffusion of In from ITO into CdS but also the diffusion of Cd or S from CdS into ITO. These results of our device performance indicate that the superstrate type substrate has high potential to become a sustainable substrate for low-cost CZTSSe solar cells.

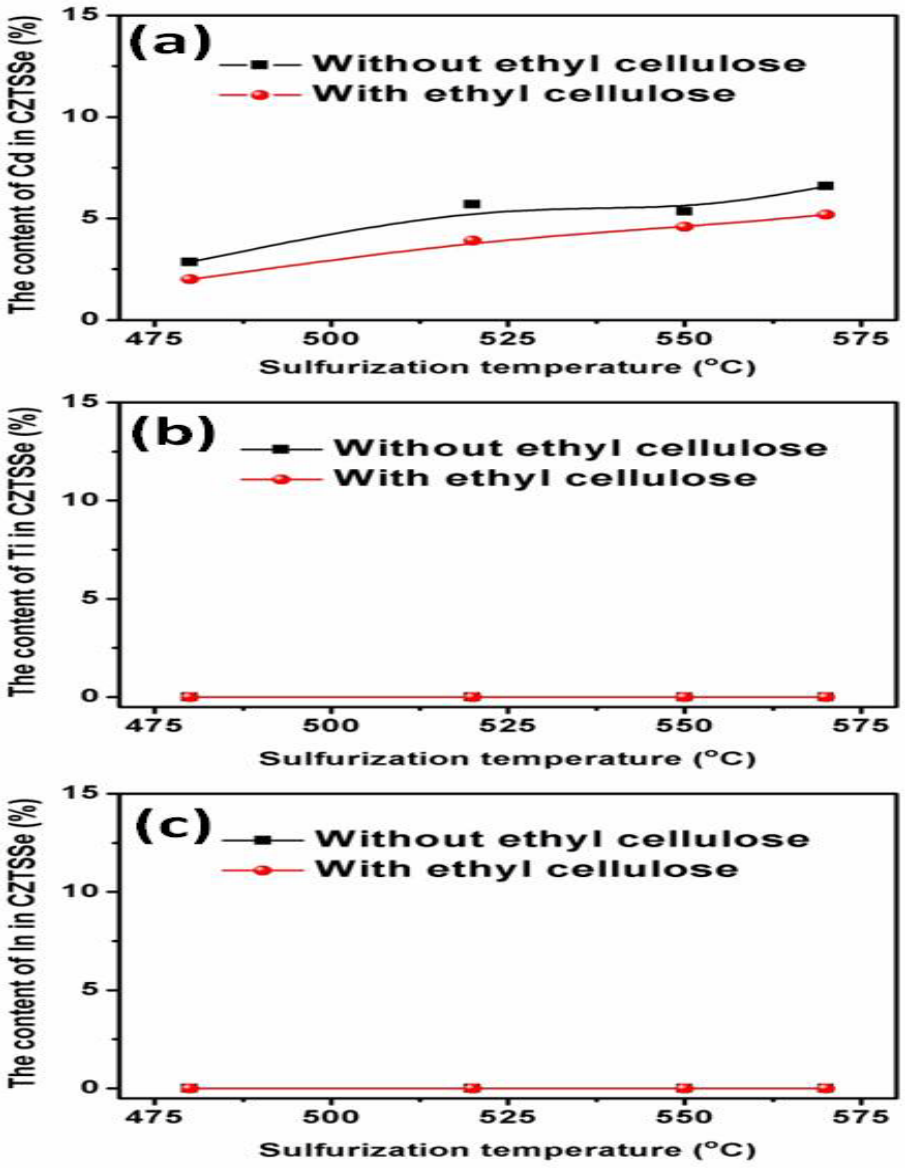

Figure 4.7. The content of (a) Cd, (b) Ti, and (c) In in the CZTSSe as a function of sulfurization temperature.

However, the high conversion efficiency of CZTSSe achieved by using hexanethiol, as given in Table 4.1, suggests that our initial device performance with a low short-circuit current (7.75 mA cm^{-2} for ethanol and 6.83 mA cm^{-2} for ethyl cellulose) could be further raised by fabricating a robust film to improve the transport properties of electrons and holes.

Table 4.1. Reported efficiencies of $Cu_2ZnSn(S,Se)_4$ nanocrystal-based absorbers.[27-30, 138]

Device structure	Solvent	V_{oc} (mV)	J_{sc} ($mAcm^{-2}$)	FF (%)	Eff. (%)
Glass/Au/CZTS/CdS/ZnO/ITO	Toluene	321	1.95	37.0	0.23
Glass/Mo/CZTSSe/CdS/ZnO/ITO	Toluene	210	11.5	33.1	0.80
Glass/Mo/CZTSSe/CdS/ZnO/ITO	Hexanethiol	420	30.4	52.7	6.73
Glass/Mo/CZTSSe/CdS/ZnO/ITO	Hexanethiol	451	29.0	64.9	8.50
Glass/ITO/TiO_2/CdS/CZTSSe/Au	Ethanol	353	7.75	36.6	1.00
Glass/ITO/TiO_2/CdS/CZTSSe/Au	EC*	363	6.83	44.7	1.11

* EC refers to ethyl cellulose.

Figure 4.6f shows the cross-sectional microstructure of enlarged grains with low density, caused by the removal process of ethyl cellulose during the sulfurization, which results in an increase in the recombination rate at the grain boundaries. This suggests that it is highly possible to reduce the short circuit current and a compact film with larger grain size is required for high efficiency CZTSSe solar devices. This problem is likely to be addressed by improving the device-making processes through the optimization of the de-binder process in the heat treatment to further promote the film quality.

4.4 CONCLUSIONS

We have demonstrated a low-cost, environmentally friendly, scalable route for making CZTSSe films using CZTSe nanocrystals, synthesized by a hot injection approach, followed by a mild sulfurization process. The solar devices with the CZTSSe film exhibit apparent improvements in V_{oc} and J_{sc}, suggesting this mild sulfurization process can offer device properties comparable to that achieved with the typical harsh selenization process. In addition, with the addition of ethyl cellulose binder into the ink, the evolution of CZTSe nanocrystals into CZTSSe film is promoted, while the loss of Sn during the evolution is suppressed, which are beneficial for increasing FF and manipulating the preferred composition. However, the cross-sectional SEM image suggests there is still room for the improvement of the microstructure and a compact film with larger grain size is required for high efficiency CZTSSe solar devices.

Chapter 5: Template-free TiO_2 hollow microspheres embedded with SnO_2 nanobeans as a versatile scattering layer for dye-sensitized solar cells

5.1 Introduction

The excellent characteristics of dye-sensitized solar cells (DSSCs) with short energy-payback time, simple assembly, and eco-friendly features make them a potential option to utilize renewable energy. Since the remarkable breakthrough made by Grätzel, the basic sandwich structure consisting of a nanoparticle TiO_2 photoanode, I^-/I_3^- electrolyte, and a Pt counter electrode has been adopted as the main concept to pursue high-efficiency DSSCs.[139] Recently, a novel bilayer structural design composed of a light-scattering layer and a nano-sized transparent layer has become one promising way to effectively promote the device performance by enhancing the light absorption.[91] Different shapes within the scattering layer, such as nanorods, hollow spheres, mirror-like structures, have been explored.[140-146] However, a good scattering layer requires a submicron- or micron-scale size to effectively scatter the visible light, which sacrifices the surface area (less dye loading). Another challenge persisting with the typical TiO_2 photoanode is the low electron mobility (0.1 – 1.0 cm^2 V^{-1} S^{-1}), which severely increases the electron recombination with a submicron- or micron-scale thickness.[147] Thus, the development of a versatile scattering layer with a multi-functional structure to satisfy all the needs (dye loading, light scattering, and electron transport) of a DSSC is becoming critical.

Recently, much attention has been focused on hollow sphere structures due to their exploitable interior spherical space and controlled structure for DSSC applications.[148] For instance, the core-shell structure of Au surrounded with a TiO_2 hollow sphere was devised to eliminate the photo-induced hole by the Au

nanoparticles and suppress electron recombination.[149] In addition, utilization of multi-shelled hollow spheres takes advantage of the multi-interior spheres to simultaneously enhance the dye loading and efficiency of light scattering.[97] Unfortunately, these studies involving expensive elemental gold or template-based synthesis routes make them difficult to adapt for large-scale and low-cost manufacturing.

In this chapter, we present a facile, template-free synthesis route for TiO_2 hollow submicrospheres embedded with SnO_2 nanobeans for use as a versatile scattering layer in DSSC. The hollow spherical structure is designed to increase the light absorption by multiple light scattering. Unlike the Au@TiO_2 core-shell microstructure, the low-cost and high mobility SnO_2 (100 – 200 cm^2 V^{-1} S^{-1}) with long-term stability under ultraviolet radiation is decorated with TiO_2 hollow submicrospheres for improving the electron transport. Furthermore, the embedding of SnO_2 nanobeans in TiO_2 hollow submicrospheres increases the dye loading by increasing the surface area.

5.2 EXPERIMENTAL

5.2.1 Synthesis of SnO_2

SnO_2 was fabricated by a hydrothermal synthesis. In a typical synthesis, a solution of 0.216 g $K_2SnO_3 \cdot 3H_2O$ and 1.35 g urea was added into a solution of ethanol and water (1:1) contained in a 100 mL Teflon liner sealed with the autoclave and subjected to heat treatment at 180 ^oC for 18 h in an oven. After washing with ethanol and water, the SnO_2 powder was heated at 500 ^oC for 3 h air. The SEM images of SnO_2 are shown in Figure 5.1.

5.2.2 Synthesis of TiO_2 hollow submicrospheres

The TiO_2 hollow submicrospheres were fabricated with a facile template-free solvothermal synthesis. In a typical synthesis of TiO_2 hollow submicrospheres, a solution containing tetra-n-butyl titanate (2.33 mmol), ethanedioic acid (0.013 mol), and isopropyl alcohol (66.67 mL) was dropped in a 100 mL Teflon liner sealed with the autoclave and subjected to heat treatment at 180 ^{o}C for 6 h in an oven. Subsequently, the TiO_2 hollow submicrospheres after washing with ethanol and water several times were collected and dried for 5 h at 100 ^{o}C in a vacuum oven. The powder was heated at 500 ^{o}C for 3 h under air atmosphere before preparing the paste for doctor blade coating. The SEM images of TiO_2 hollow submicrospheres are shown in Figure 5.2.

5.2.3 Synthesis of nanobean SnO_2-embedded TiO_2 hollow submicrospheres

The embedding of SnO_2 nanobeans in TiO_2 hollow submicrosphere was performed with hydrothermal synthesis. In a typical synthesis, 200 mg of as-prepared TiO_2 hollow submicrospheres in a solution of ethanol and water (1:1) was added into a solution of 0.216 g $K_2SnO_3 \cdot 3H_2O$ and 1.35 g urea in a 100 mL Teflon liner sealed with the autoclave and subjected to heat treatment at 180 ^{o}C for 18 h in an oven. After washing with ethanol and water, the SnO_2-embedded TiO_2 hollow submicrospheres were heated at 500 ^{o}C for 3 h in air. The SEM images of nanobean SnO_2-embedded TiO_2 hollow submicrospheres are shown in Figure 5.3.

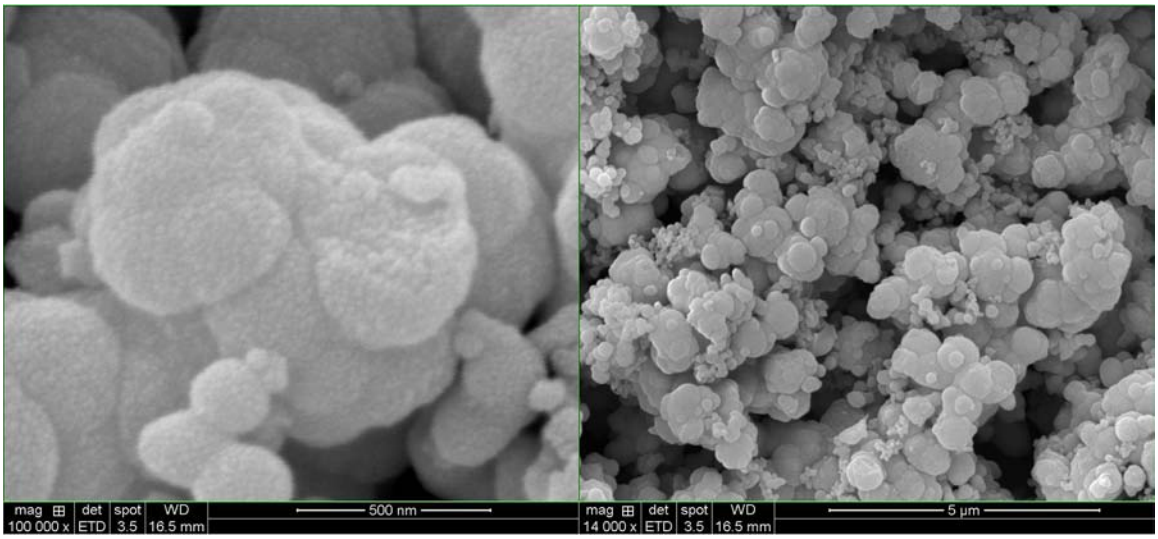

Figure 5.1. High and low magnification SEM images of SnO_2.

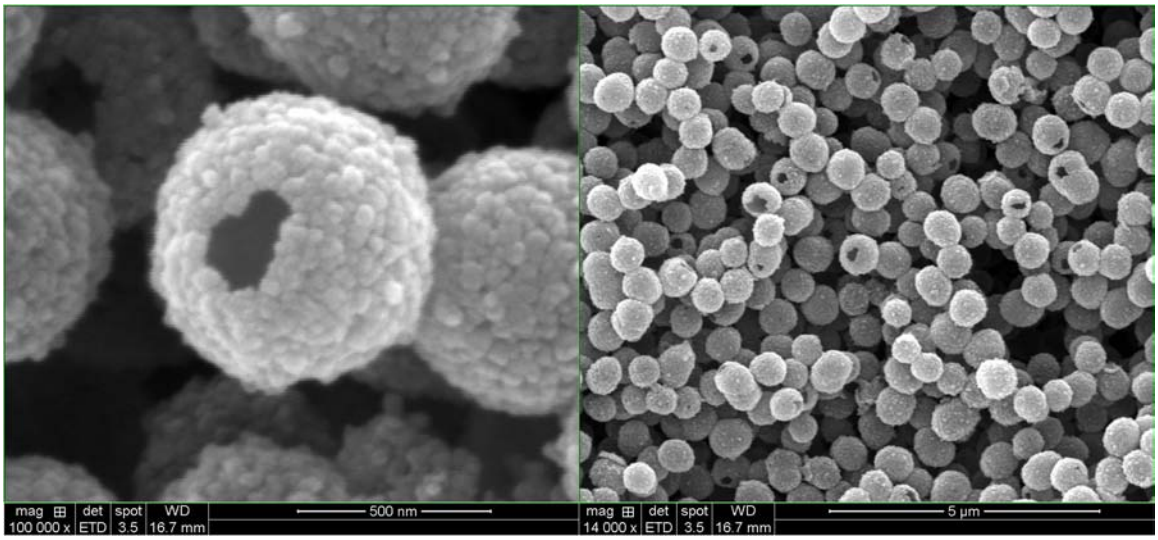

Figure 5.2. High and low magnification SEM images of TiO_2 hollow submicrospheres.

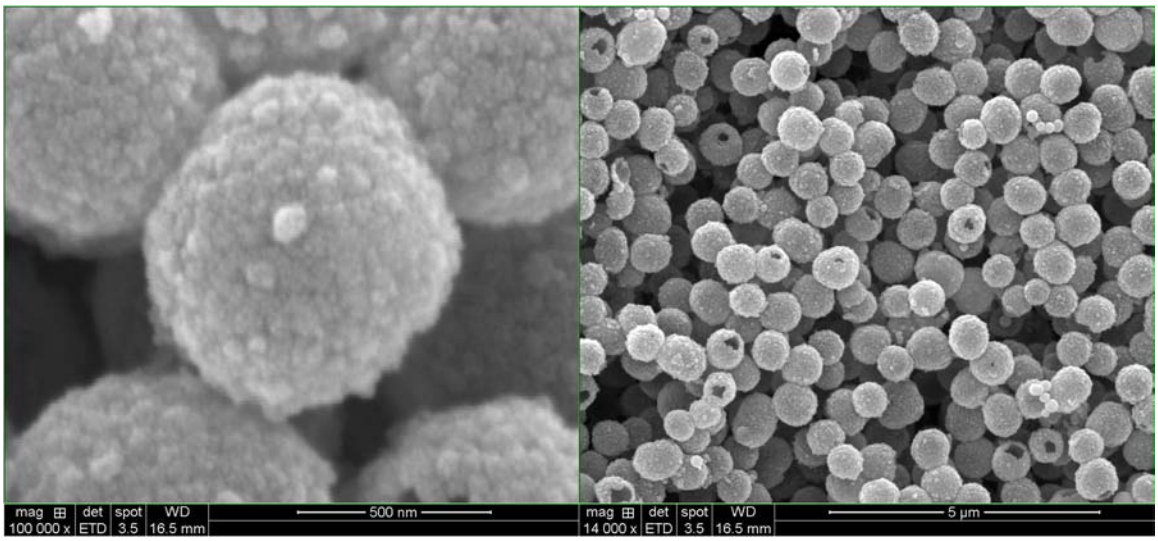

Figure 5.3. High and low magnification SEM images of nanobean SnO_2-embedded TiO_2 hollow submicrospheres.

5.2.4 Assembly of DSSCs

The bilayer film-stack photoanode consisting of a scattering layer and a transparent layer was fabricated on fluorine doped tin oxide (FTO) glass substrate. The paste for the transparent layer was prepared with 1 g of P25 TiO_2 powder, 0.2 mL of acetic acid, 3 g of terpineol, 0.5 g of ethyl cellulose, and 10 mL of ethanol. The other paste for the scattering layer was prepared with 50 mg of the SnO_2 (TiO_2 hollow submicrospheres or nanobean SnO_2-embedded TiO_2 hollow submicrospheres) powder, 150 mg of terpineol, 25 mg of ethyl cellulose, and 0.5 ml of ethanol. A transparent layer of ~ 10 µm and a scattering layer of ~ 4 µm were achieved by multiple doctor blade coatings with, respectively, the P25 TiO_2 paste and SnO_2 (the TiO_2 hollow submicrospheres or nanobean SnO_2-embedded TiO_2 hollow submicrospheres) paste, followed by a heat treatment for 15 min at 500 °C. The sample was then immersed in 40

mM of an aqueous $TiCl_4$ solution at 70 °C for 30 min, followed by heat treatment for 15 min at 520 °C to grow a thin TiO_2 layer on the surface. Cross-sectional images of the three photoanodes composed of the scattering layers (SnO_2, TiO_2 hollow submicrospheres, and nanobean SnO_2-embedded TiO_2 hollow submicrospheres) on the nano-sized TiO_2 transparent layer are shown in Figure 5.7-9. Subsequently, a 0.5 mM solution of N719 dye (acetonitrile and *tert*-butyl alcohol = 1:1) was prepared for dye adsorption and the photoanodes were immersed for 16 h. The Pt counter electrode was synthesized with a 5 mM H_2PtCl_6 isopropanol solution onto a FTO glass substrate at 400 °C for 15 min. Then, the sensitized photoanode and the counter electrode were assembled with the electrolyte to construct the DSSC cell. The ingredients of the as-prepared electrolyte contained 0.6 M of 1-methyl-3-propylimidazolium iodide (PMII), 0.05 M of lithium iodide (LiI), 0.03 M of iodine (I_2), 0.1 M of guanidinium thiocyanate (GuNCS), and 0.5 M of 4-tert-butyl-pyridine (tBP) in a mixture of acetonitrile and valeronitrile (85:15 in volume ratio). The current density-voltage characteristics of DSSCs with a defined area of 0.12 cm^2 were measured under AM 1.5 G illumination with a solar simulator using 100 mW cm^{-2}.

5.2.5 Characterization of Materials

The crystal structure of the scattering materials were characterized by a Rigaku X-ray diffractometer (XRD) and JEOL 2010F transmission electron microscope (TEM). The morphologies and the elemental mapping of the materials were collected with a Hitachi S5500 scanning electron microscope (SEM)/scanning transmission electron microscope (STEM) equipped with energy dispersive spectroscopy (EDS). The surface area and pore-size distributions were measured by the Brunauer-Emmett-Teller (BET)

method with an automated gas sorption analyzer (AutoSorb iQ2, Quantachrome Instruments). Diffuse reflectance spectra were recorded with a Varian Cary 500 UV-Vis-NIR instrument equipped with an integrating sphere of a Labsphere DRA-CA-5500. The amount of dye adsorption was acquired with a Cary 5000 UV-Vis-NIR spectrometer. The electrochemical properties were analyzed by electrochemical impedance spectroscopy (EIS) data collected with a program-controlled Solartron SI 1287 and SI 1260 instrument.

5.3 RESULTS AND DISCUSSION

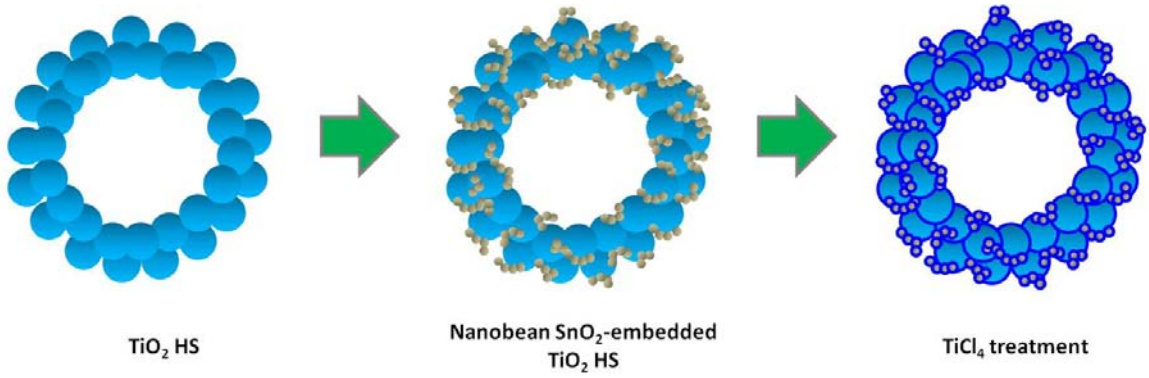

Figure 5.4. 2-D schematic diagram showing the formation of nanobean SnO_2-embedded TiO_2 hollow submicrospheres (HS).

Figure 5.4 shows the 2-D schematic diagram for the formation of the SnO_2-embedded TiO_2 hollow submicrospheres (SnO_2-embedded TiO_2 HS). The template-free TiO_2 hollow submicrospheres (TiO_2 HS) were first fabricated with an inside-out Ostwald ripening process.[150] Subsequently, the TiO_2 HS were embedded with the SnO_2 nanobeans to increase the surface area and porosity. Finally, an ultra thin TiO_2

layer was deposited on the circumference of SnO_2 nanobeans with a $TiCl_4$ treatment to passivate the surface of the SnO_2. Further experimental details can be found in the electronic supplementary information.

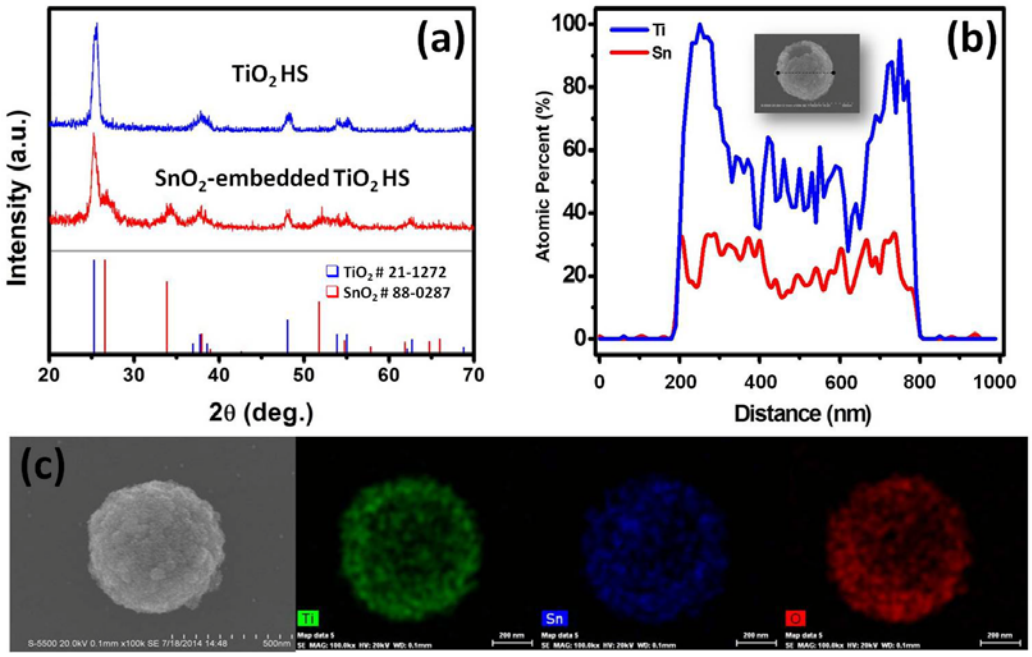

Figure 5.5. (a) XRD analysis of the TiO_2 HS before and after the embedding of SnO_2 nanobeans; (b) STEM line scan analysis and SEM image (inset) of the nanobean SnO_2-embedded TiO_2 HS; and (c) elemental mapping of the nanobean SnO_2-embedded TiO_2 HS.

The XRD analyses of the TiO_2 HS before and after the embedding of SnO_2 are shown in the top panel of Figure 5.5. It can be seen that the XRD patterns of TiO_2 HS without the embedding of SnO_2 matches well with JCPDS 21-1272, indicating that our hollow submicrospheres synthesized by the Ostwald ripening process can produce

a pure anatase phase of TiO_2. The bottom panel in Figure 5.5a shows the XRD of the TiO_2 HS after the embedding of SnO_2. The additional XRD peaks, other than those of the anatase TiO_2 phase, can be identified with JCPDS 88-0287, revealing that the hydrothermal process can also facilitate the formation of a pure rutile-phase SnO_2 on the anatase TiO_2 HS.[151, 152]

Scanning transmission electron microscopy (STEM) and energy dispersive spectroscopy (EDS) line scan were used in Figure 5.5b to characterize the distribution of Sn over the TiO_2 HS after the embedding of SnO_2. The STEM image indicates that the hollow spherical submicrostructure of TiO_2 is preserved after the embedding of SnO_2, suggesting that our template-free route for producing a hollow sphere is robust and comparable to the template-based hollow sphere routes. In addition, its surface is decorated with mesopores, leading to an increase in the surface area. The EDS line scan also indicates that the distribution of Ti has a strong concentration at both edges but a weak concentration at the center, which is consistent with a hollow sphere shape. Unlike the distribution of Ti, Sn shows roughly constant concentration, indicating the embedding of SnO_2 is accommodated well at the surface of TiO_2 hollow spherical structure. Furthermore, the elemental mapping of STEM confirms that the embedding of SnO_2 is uniformly dispersed among TiO_2 HS as shown in Figure 5.5c.

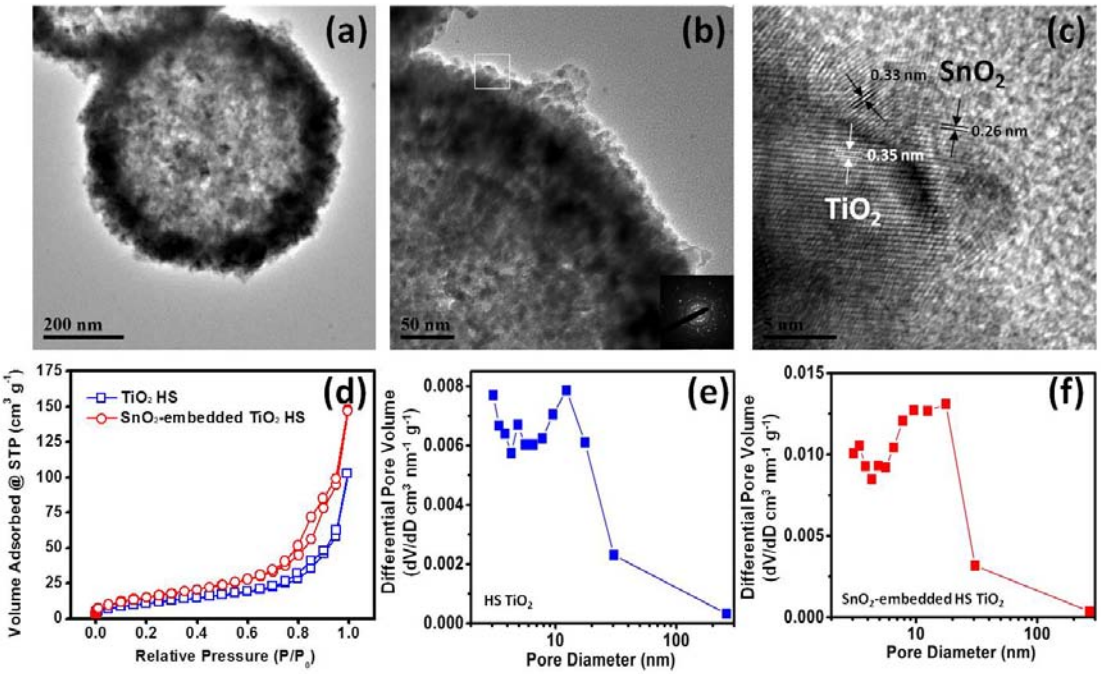

Figure 5.6. TEM image of (a) the nanobean SnO_2-embedded TiO_2 HS; (b) high-magnification TEM image and the SAED patterns (inset) of the nanobean SnO_2-embedded TiO_2 HS; (c) high-resolution TEM images of the nanobean SnO_2-embedded TiO_2 HS; (d) N_2 adsorption and desorption isotherms of the TiO_2 HS before and after the formation of SnO_2 nanobeans; pore-size distribution of the (e) TiO_2 hollow microsphere and (f) nanobean SnO_2-embedded TiO_2 HS.

The transmission electron microscopy (TEM) images in Figure 5.6a-d show a composite microstructure for the SnO_2-embedded TiO_2 HS. As seen in Figure 5.6a, the hollow sphere has a diameter of 600 nm with a wall thickness of 100 nm, which makes it suitable for light scattering in the wavelength range of 400 nm - 800 nm. In addition, Figure 5.6a indicates that the morphology and structure of the SnO_2 embedded over the hollow sphere possesses a nanobean shape of around 5 nm, which

effectively decorates the surface of TiO_2 HS, assembling a highly mesoporous microstructure. The high-resolution TEM in Figure 5.6c reveals that both the embedded SnO_2 nanobeans and TiO_2 HS possess highly crystalline structures, which is consistent with the XRD analysis in Figure 5.5a. The surface area and pore-size distribution of the nanobean SnO_2-embedded TiO_2 HS were determined by the Brunauer-Emmett-Teller (BET) measurement. Nitrogen adsorption-desorption isotherms with IUPAC (International Union of Pure and Applied Chemistry) type H3 hysteresis loops are shown in Figure 5.6d, which verifies the existence of a mesoporous microstructure for both the TiO_2 HS and the nanobean SnO_2-embedded TiO_2 HS. In addition, the pore-size distribution of TiO_2 HS shows a maximum distribution around 12 nm, as compared with that of the nanobean SnO_2-embedded TiO_2 HS with a broad distribution from 7 to 17 nm; this suggests that the embedded SnO_2 nanobeans were deposited into the pores at the TiO_2 HS. Thus, the surface area of TiO_2 HS (40 m^2 g^{-1}) is increased to 56 m^2 g^{-1} after the embedding of SnO_2, which enables the nanobean SnO_2-embedded TiO_2 HS to accommodate a high amount of dye loading.

The bilayer film-stack structure composed of a series of scattering layers (SnO_2, TiO_2 HS, and SnO_2-embedded TiO_2 HS) atop a nano-sized TiO_2 film followed by the $TiCl_4$ treatment was used to investigate the amount of dye adsorption and light scattering. The cross-sectional SEM images of the bilayer film-stack structure are shown in Figure 5.7-9.

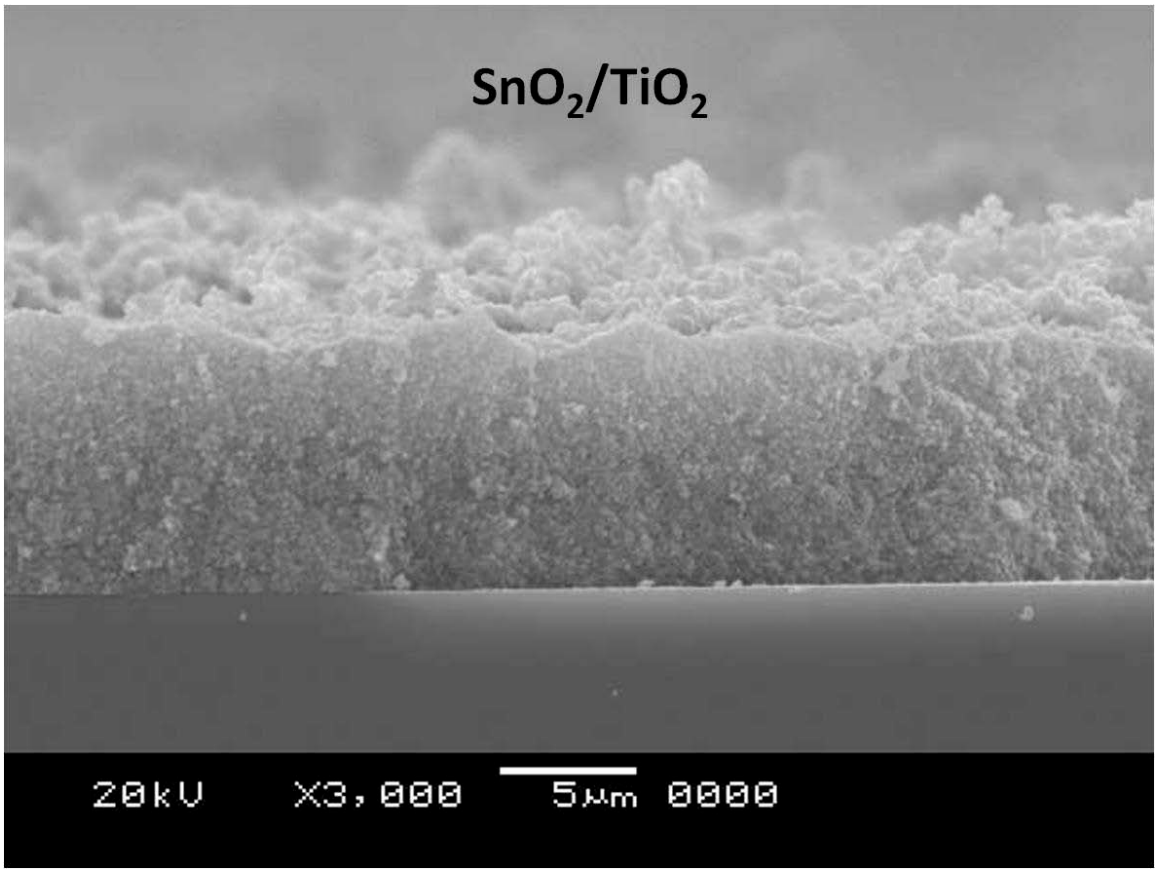

Figure 5.7. Cross-sectional SEM image of the bilayer photoanode of SnO_2 on the nano-sized TiO_2 transparent layer.

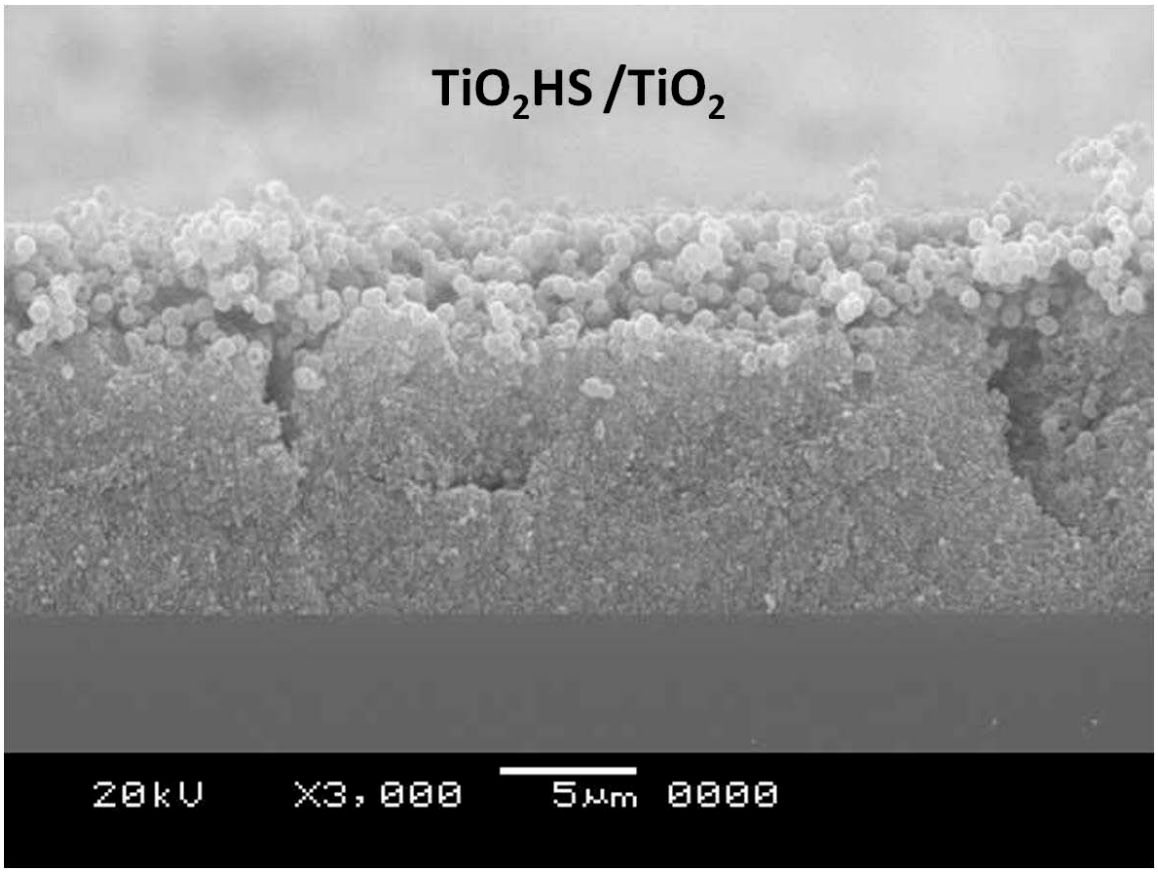

Figure 5.8. Cross-sectional SEM image of the bilayer photoanode of TiO_2 hollow submicrospheres on the nano-sized TiO_2 transparent layer.

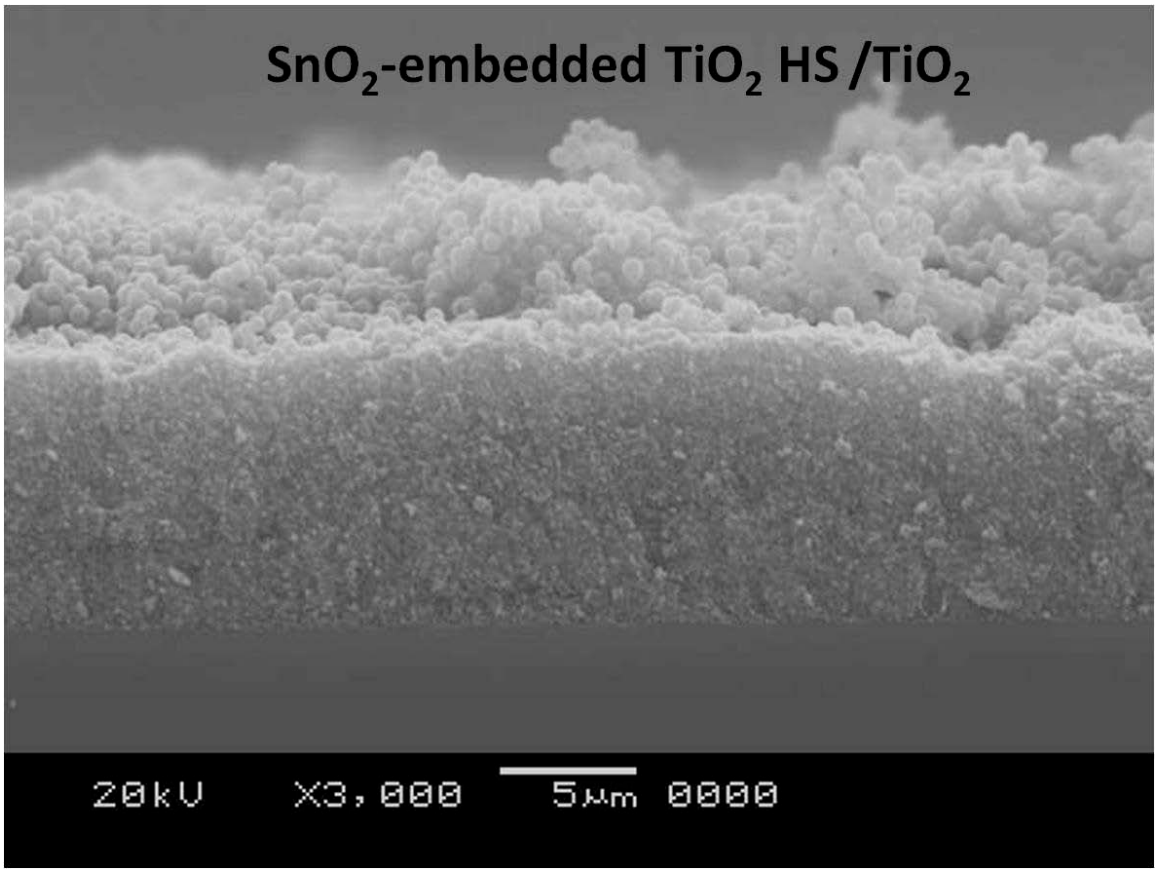

Figure 5.9. Cross-sectional SEM image of the bilayer photoanode of nanobean SnO_2-embedded TiO_2 hollow submicrospheres on the nano-sized TiO_2 transparent layer.

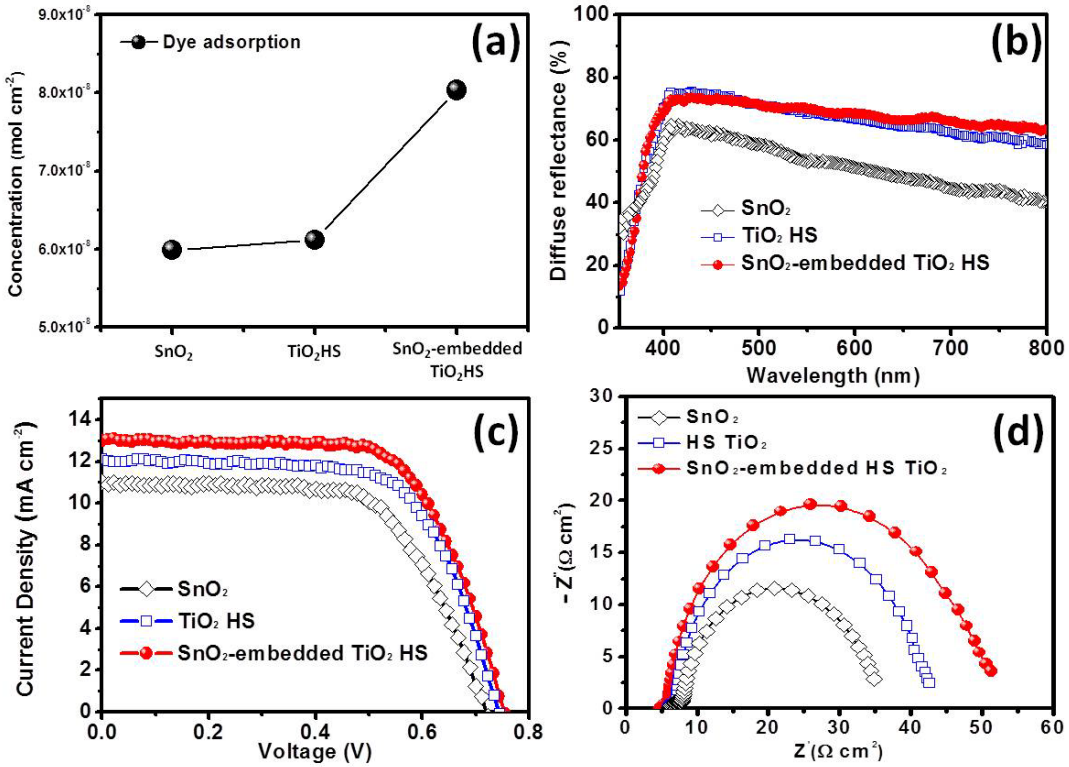

Figure 5.10. (a) Amount of dye loading, (b) UV-diffuse reflectance, (c) *J* - *V* characteristics, and (d) Nyquist plot of the DSSCs with different scattering layers of SnO_2, TiO_2 HS, and SnO_2-embedded TiO_2 HS atop the nano-sized TiO_2 film.

In Figure 5.10a, the SnO_2-embedded TiO_2 HS with high surface area exhibits a high amount of dye adsorption (8.03×10^{-8} mol cm^{-2}) as compared with the poor dye adsorption of SnO_2 (5.98×10^{-8} mol cm^{-2}) and the lower surface area TiO_2 HS (6.11×10^{-8} mol cm^{-2}), suggesting that the possibility of the electron stimulated from the ground state to the excited state in the dye can be increased to improve the short-circuit-current density J_{sc}. Figure 5.10b reveals the diffuse reflectance spectra of a series of SnO_2, TiO_2 HS, and SnO_2-embedded TiO_2 HS scattering layers atop the

nano-sized TiO_2 film. It can be seen that the SnO_2-embedded TiO_2 HS and TiO_2 HS have higher diffuse reflectance than SnO_2 to effectively scatter the incident light in the wavelength range of 400 – 800 nm. Fabrication of the DSSCs with a series of scattering layers was used to evaluate the power conversion efficiency with a solar simulator under AM 1.5 condition. The *J-V* characterization as shown in Figure 5.10c reveals the conversion efficiency of SnO_2-embedded TiO_2 HS is 6.58% with J_{sc} = 13 mA cm^{-2}, V_{oc} = 754 mV, and *FF* = 67.21%, which is higher than those of TiO_2 HS (6.01%) and SnO_2 (5.11%). (The error bar in efficiency is estimated to be ±0.02%.) More photovoltaic and electrochemical impedance spectroscopy (EIS) parameters are summarized in Table 5.1. The DSSC with a SnO_2-embedded TiO_2 HS scattering layer mainly exhibits an improvement in both J_{sc} and V_{oc}, which enhances the conversion efficiency by around 28% as compared with a SnO_2 scattering layer. The enhancement in J_{sc} can be attributed to the higher diffuse reflectance and the greater dye loading, as seen, respectively, in Figure 5.10a and Figure 5.10b. In addition, the increase in V_{oc} can be associated with the reduced recombination due to the embedding of SnO_2 nanobeans on the TiO_2 HS.

Table 5.1. Photovoltaic and EIS parameters of the cells with different scattering materials

Scattering layers	J_{sc} (mA cm^{-2})	V_{oc} (V)	*FF* (%)	*PCE* (%)	R_s (Ω cm^2)	R_{cr} (Ω cm^2)	R_{ct} (Ω cm^2)
SnO_2	720	11.01	64.58	5.11	6.06	25.17	1.56
TiO_2 HS	743	12.13	66.70	6.01	5.99	34.04	0.91
SnO_2-embedded TiO_2 HS	754	13.00	67.21	6.58	4.89	42.01	0.89

R_s, R_{cr}, and R_{ct} refer, respectively, to series resistance, charge recombination resistance, and charge transfer resistance. (The error bar of EIS is estimated to be ±0.05 Ω cm^2.)

To further investigate the charge-transfer process and electron transport, EIS data were collected at open-circuit voltage with an AC amplitude of 10 mV in the frequency range from 0.1 Hz to 1 MHz in the dark. Figure 5.10d shows the Nyquist impedance spectra of the cells with a series of scattering layers (SnO_2, TiO_2 HS, and SnO_2-embedded TiO_2 HS) atop the nano-sized TiO_2 film. The equivalent circuit diagram of the cell is shown in Figure 5.11.

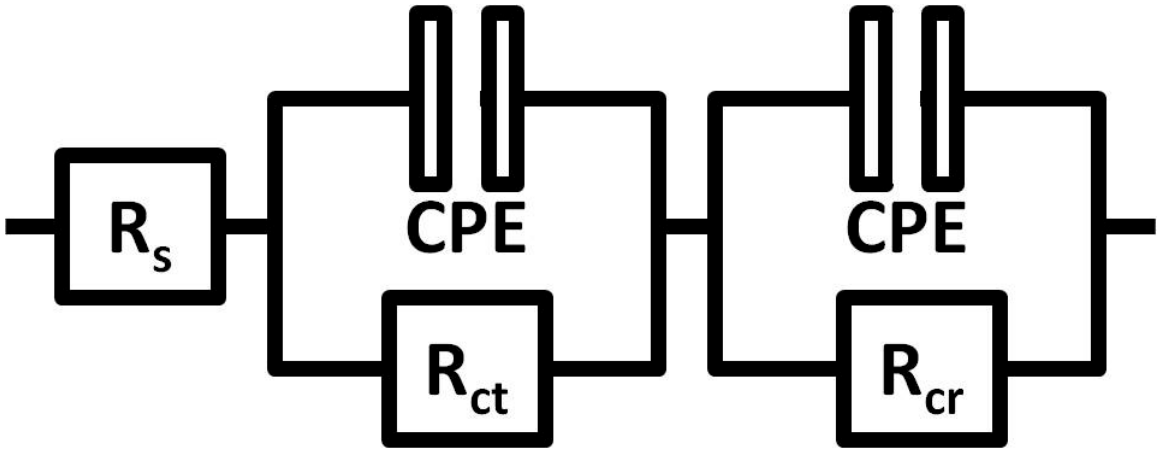

Figure 5.11. The equivalent-circuit diagram of the cell was used to extract the parameters of R_s (series resistance), R_{cr} (charge-recombination resistance), and R_{ct} (charge-transfer resistance). R_{cr} reflects the charge recombination associated with the charge-transfer resistance at the interface of metal oxides/dye/electrolyte and the electron transport in the photoanodes of the metal oxides. R_{ct} is related with the charge transfer between electrolyte and counter electrode.

It is known that the semicircle in the middle frequency range reflects charge recombination, which is attributed to the charge-transfer resistance at the interfaces of metal oxides/dye/electrolyte and the electron transport in the photoanodes of the

metal oxides.[153] A larger semicircle for the cell using the scattering layer of SnO_2-embedded TiO_2 HS (42.01 Ω cm^2) than those for TiO_2 HS (34.04 Ω cm^2) and SnO_2 (25.17 Ω cm^2) reveals a lower electron recombination, which agrees well with the high V_{oc} obtained with SnO_2-embedded TiO_2 HS. Furthermore, a comparative study of SnO_2-embedded TiO_2 HS and TiO_2 HS confirms that the low electron recombination in SnO_2-embedded TiO_2 HS can be mainly attributed to the nanobeans of SnO_2 embedded in TiO_2 HS due to the improvement in electron transport by the high mobility of SnO_2 in the metal-oxide photoanode.

5.4 Conclusions

In conclusion, a designed microstructure of template-free TiO_2 hollow submicrospheres embedded with SnO_2 nanobeans has been developed for use as a versatile scattering layer in DSSC. In addition to the enhanced light scattering by submicro-scale TiO_2 hollow spheres, the embedding of SnO_2 nanobeans in the hollow sphere has been found to effectively increase the surface area, leading to an improvement in the dye loading. A 28 % improvement in the conversion efficiency could be achieved by adopting this designed structure as a scattering layer to provide a promising combination of improvement in dye adsorption, light harvesting, and electron transport.

Chapter 6: Carbonized eggshell membranes as a natural and abundant counter electrode for efficient dye-sensitized solar cells

6.1 Introduction

The ultimate goal of renewable solar energy is aimed at developing low-cost, high-efficiency photovoltaic technologies that can satisfy the demand for future terawatt-scale solar energy. The dye-sensitized solar cells (DSSC), with a light-electricity conversion efficiency exceeding 12%, are considered to be one of the most promising candidates for next-generation solar cells due to their facile assembly, cost-effectiveness, and environmental friendliness.[50, 154] The prototypical architecture of a DSSC consists of a porous film of n-type TiO_2, a photosensitized dye, a redox couple consisting of I^-/I_3^- electrolyte, and a Pt counter electrode. The noble and scarce nature of Pt as well as its poor stability in the electrolyte has become a significant hurdle to realize low-cost, and thus, large-scale, deployment of DSSCs. Upon solar illumination, the dye molecule undergoes an electronic transition from the ground state to the excited state. This is followed by an ultrafast electron injection from the excited state of the dye molecule into the conduction band of TiO_2, which leads to the oxidation of the dye molecule. The oxidized dye subsequently stimulates the reduction of iodide into triiodide in the electrolyte, and the electron injected into the conduction band of TiO_2 is transported to the counter electrode. The function of the counter electrode is to regenerate iodide from triiodide in order to complete the light-electricity conversion process. Accordingly, the electrical properties and catalytic ability of the counter electrode (CE) play a significant role in the DSSC process.

Materials previously explored as alternatives to Pt for CEs include carbonaceous materials, conductive polymers, metal compounds, and composite materials.[40, 41, 51] However, materials that involve toxic and/or complex synthesis processes or that contain

vulnerable microstructures, become challenging for large-scale manufacturing. In contrast to such materials, natural materials drawn directly from our surroundings are abundant, accessible, and environmentally friendly. Several naturally-derived materials, composed of unique structures, have been developed for advanced applications, such as synthesis templates, photonic crystals, supercapacitors, Li-S batteries, and DSSCs.[155-163] Recently, it is further found that the electrochemical activity of the naturally-derived materials as CEs in DSSC can be correlated with their unique structures and demonstrated their potential to substitute for the typical Pt electrode. For instance, the macroporous structure (beyond 50 nm) of carbonized sea tangle and the mesoporous structure (2-50 nm) of carbonized oak were explored by, respectively, Grätzel *et al.* and Gao *et al.*[162, 163] However, the relationship between the electrochemical activity and the microstructure remain unclear and naturally-derived CEs composed of micropores (less than 2 nm) have not yet been applied to DSSCs as CEs.

In this chapter, we present a naturally-derived carbonaceous material as a Pt-free CE for DSSCs. The material was made from eggshell membranes that were recycled from domestic waste. It is found that the unique micropore-rich, hierarchically-porous microstructure of eggshell membranes can effectively facilitate the charge transfer process, leading to an improved V_{oc} and a competitive efficiency as compared to a DSSC with a traditional Pt-based CE.

6.2 Experimental

6.2.1 Preparation of the counter electrode

The sucrose-coated eggshell membranes were fabricated with eggshell membranes immersed in a 40% sucrose solution, followed by a pre-carbonization process

at 180°C.[159] After a carbonization process at 800°C, CSEMs were ground to a powder for ink preparation. Commercial CP purchased from Ted Pella, Inc. (Product No. 16053) was used to enhance the adhesion of the CSEM powder to the commercial fluorine-doped tin oxide (FTO) substrate (purchased from Nanocs (New York, NY)). Inks composed of CSEMs mixed with different amounts of commercial CP were prepared for the doctor-blade coating. A targeted thickness of around 10 μm was achieved by doctor-blade coating the CSEM ink four times onto a FTO substrate. To remove the binder, all of the CEs were heat treated at 350°C for 15 min under Ar flow. The traditional Pt CE was fabricated by a pyrolysis of a pre-coated 5 mM H_2PtCl_6 isopropanol solution onto a FTO substrate at 400 °C for 15 min.

6.2.2 Preparation of TiO_2 photoanode

The TiO_2 photoanode was fabricated on a FTO substrate. TiO_2 with a thickness of ~ 12 μm was fabricated with doctor-blade coatings followed by heat treatment for 15 min at 500°C. Next, the sample was immersed into 40 mM of a $TiCl_4$ aqueous solution at 70°C for 30 min, followed by another heat treatment for 15 min at 520°C. Dye absorption onto the TiO_2 layer was performed for ~ 16 h by immersing the photoanode in a 0.5 mM solution of N719 dye, prepared by mixing acetonitrile and *tert*-butyl alcohol in a volume ratio of 1:1.

6.2.3 Assembly of DSSCs

A sandwich cell composed of the TiO_2 photoanode and the CE was assembled with the electrolyte in-between. The electrolyte was prepared by using 0.6 M of 1-methyl-3-propylimidazolium iodide (PMII), 0.05 M of lithium iodide (LiI), 0.03 M of

iodine (I_2), 0.1 M of guanidinium thiocyanate (GuNCS), and 0.5 M of 4-tert-butyl-pyridine (tBP) in a mixture of acetonitrile and valeronitrile with a volume ratio of 85:15. The active area of the DSSC was 0.12 cm^2. The current density-voltage characteristics of DSSCs were measured with a Keithley 2400 equipment under AM 1.5 G illumination with a solar simulator using 100 mW cm^{-2}.

6.2.4 Materials characterization

The surface morphologies of the counter electrodes were characterized by a FEI Quanta 650 scanning electron microscope (SEM). The electrochemical impedance spectroscopy (EIS) based on a symmetric dummy cell and three-electrode cyclic voltammetry (C-V) ($Ag/AgNO_3$ as a reference electrode and Pt foil as a counter electrode) were utilized to analyze the electrochemical properties. A symmetrical dummy cell configuration was fabricated with two idnetical CEs. The Raman spectra were recorded on a Renishaw inVia Raman microscope with 532 nm laser excitation and a 50X objective. The surface area and pore-size distributions were acquired with the Brunauer-Emmett-Teller (BET) method using an automated gas sorption analyzer (AutoSorb iQ2, Quantachrome Instruments).

6.3 RESULTS AND DISCUSSION

Figure 6.1a shows the scanning electron microscopy (SEM) image of an eggshell membrane before carbonization. It exhibits an entangled architecture of interwoven coalescing fibers, which form a highly porous microstructure. To further enhance the electrical conductivity, the carbonized eggshell membranes were surface-coated with a layer of carbon. The carbonized sucrose-coated eggshell membranes (CSEMs) were

prepared by immersing the fresh eggshell membranes into a sucrose solution and then carbonizing at 800°C. The uniformly coarsened and thickened morphology of the CSEM in Figure 6.1b indicates that the carbonized sucrose is well-coated onto the surface of the eggshell membrane fibers and that the original porous microstructure of the membrane is preserved after carbonization. The inset in Figure 6.1c shows the CSEMs after they have been ground into a powder with a mortar and pestle. As shown in Figure 6.1c, their microstructure is preserved, thus allowing for the fabrication of a CSEM ink that can be cast with a doctor blade method. The cross-sectional SEM image in Figure 6.1d reveals that the doctor blading of an ink of CSEMs mixed with the conductive paint (CP) yields a robust counter electrode, suitable for use in DSSCs. The film adheres well to the FTO substrate as compared to a CSEM film without CP in Figure 6.2.

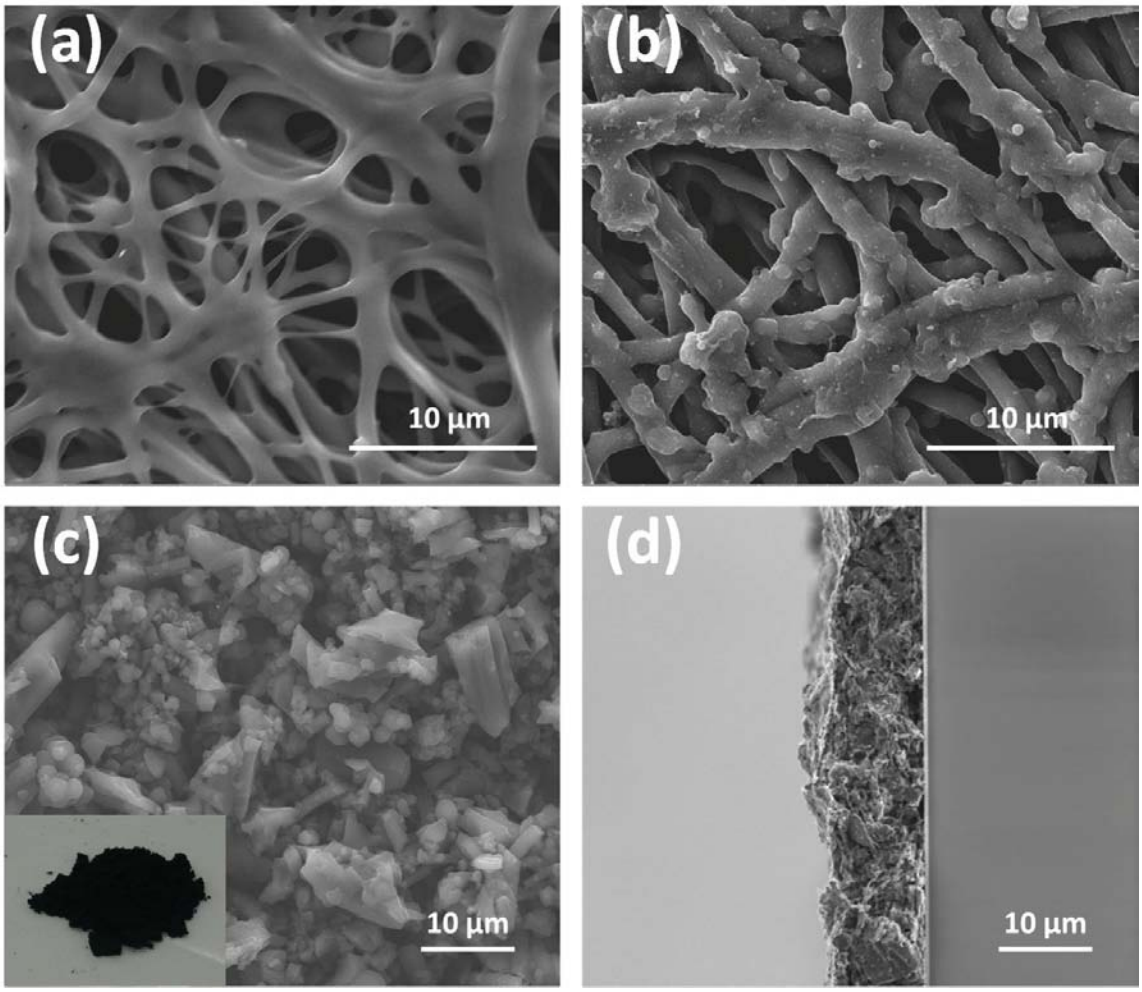

Figure 6.1. In-plane SEM images of (a) an eggshell membrane, (b) CSEM, (c) CSEM after grinding with a mortar and pestle, and (d) cross-sectional SEM image of a CSEM mixed with CP.

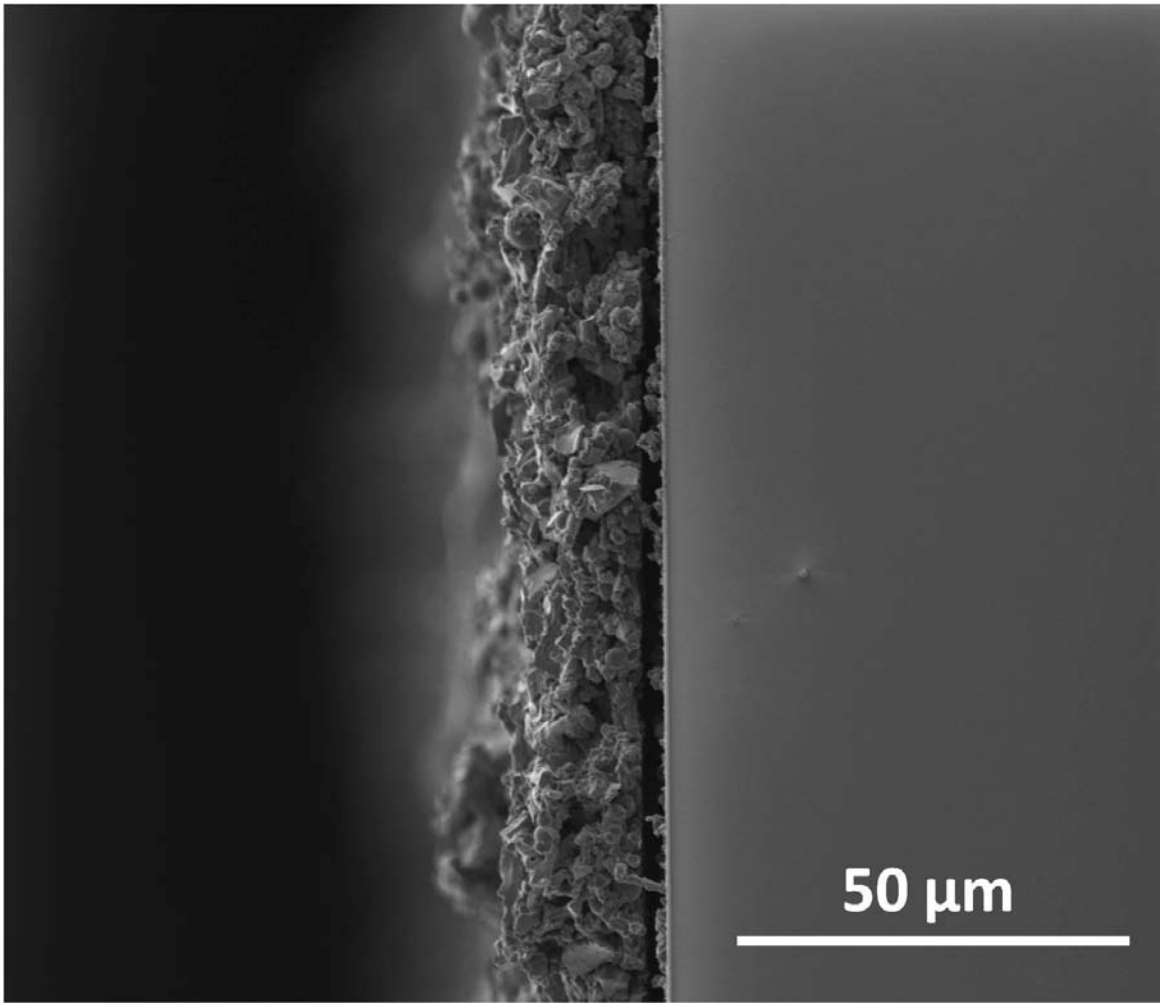

Figure 6.2. Cross-sectional SEM image of CSEM without CP.

Three-electrode cyclic voltammetry was performed to investigate the electrocatalytic activity of the CSEM CE for the reduction of triiodide into iodide. Figure 6.3a shows the cyclic voltammograms (CVs) at 100 mV s^{-1} for CEs based on CSEMs, CP, and Pt in a liquid electrolyte composed of 0.1 M $LiClO_4$, 10 mM LiI, and 1 mM I_2 in acetonitrile. As expected, the CV for the traditional Pt CE shows two clear pairs of redox peaks attributed to (1) the I^-/I_3^- couple at -0.318 V and 0.091 V (*vs.* Ag/Ag^+) and (2) the I_3^-/I_2 couple at 0.265 V and 0.490 V:.

$$I_3^- + 2e^- \leftrightarrow 3I^- \qquad (1)$$

$$3I_2 + 2e^- \leftrightarrow 2I_3^- \qquad (2)$$

The electrocatalytic activity of the CE for the regeneration of the I^-/I_3^- redox couple in DSSCs is directly related to the cyclic voltammetry cathodic current density. The redox peak-to-peak separation is also inversely proportional to charge transfer rate.[80] Thus, the CV of the CE based on CSEM shows a small peak-to-peak separation and higher cathodic current density as compared to the CEs based on Pt and CP, indicating that CSEMs possess superior electrocatalytic activity for the regeneration of the I^-/I_3^- redox couple.

Raman spectroscopy was performed in order to identify the electrocatalytic site of the CSEMs. The top panel of Figure 6.3b shows the Raman spectrum of the CSEMs. Two peaks corresponding to the D and G bands of carbon appear, respectively, at 1343 cm^{-1} and 1589 cm^{-1}. The G band of carbonaceous materials reveals the degree of graphitization while the D band corresponds to the number of defects and disorders, which are known to catalyze the I^-/I_3^- redox couple.[164, 165] The D band peak of CSEMs exhibits a comparable intensity and broader peak width than the G band peak, indicating that the CSEMs contain a low degree of graphitization and a high degree of defects. In contrast, the bottom panel of Figure 6.3b shows that the G band of CP shows much stronger

intensity than the D band, indicating a higher level of graphitization. As a result, this comparative study, along with the cyclic voltammetry results, suggests that the electrocatalytic sites of CSEMs originate from the defects and disorders in its structure.

The surface area and pore-size distributions of the CSEM and CP were evaluated by, respectively, the Brunauer-Emmett-Teller (BET) measurements as well as Horvath-Kawazoe (HK) and density functional theory (DFT) models. Figure 6.3c shows that CSEMs possess a high surface area of 401 $m^2 g^{-1}$ with a total pore volume of 0.25 $cm^3 g^{-1}$ while the CP has a surface area of 39 $m^2 g^{-1}$ with a pore volume of 0.22 $cm^3 g^{-1}$. In addition, the proportion of micropore volume to total pore volume in the CSEM approaches 80%. The nitrogen adsorption-desorption isotherms in Figure 6.3c show that this material exhibits an IUPAC type I isotherm at $P/P_0 < 0.1$ along with a minor IUPAC type H3 mesoporous hysteresis loop at $P/P_0 = 0.45 - 1.0$. This confirms the presence of a hierarchical micro- and meso-porous structure. On the other hand, the CP exhibits an IUPAC type H3 mesoporous hysteresis loop, which is likely due to the presence of aggregates of plate-like conductive carbon particles. In Figure 6.3d, the HK pore-size distribution model indicates that the high microporosity of the CSEM is mostly due to the micropores with a pore size of 0.5 nm. Therefore, triiodide ions with a minimum diameter of 0.3 nm can effectively penetrate into the electrocatalytically active defect-rich micropores of the CSEM and readily undergo the charge transfer process for the regeneration of I^-/I_3^-.[166]

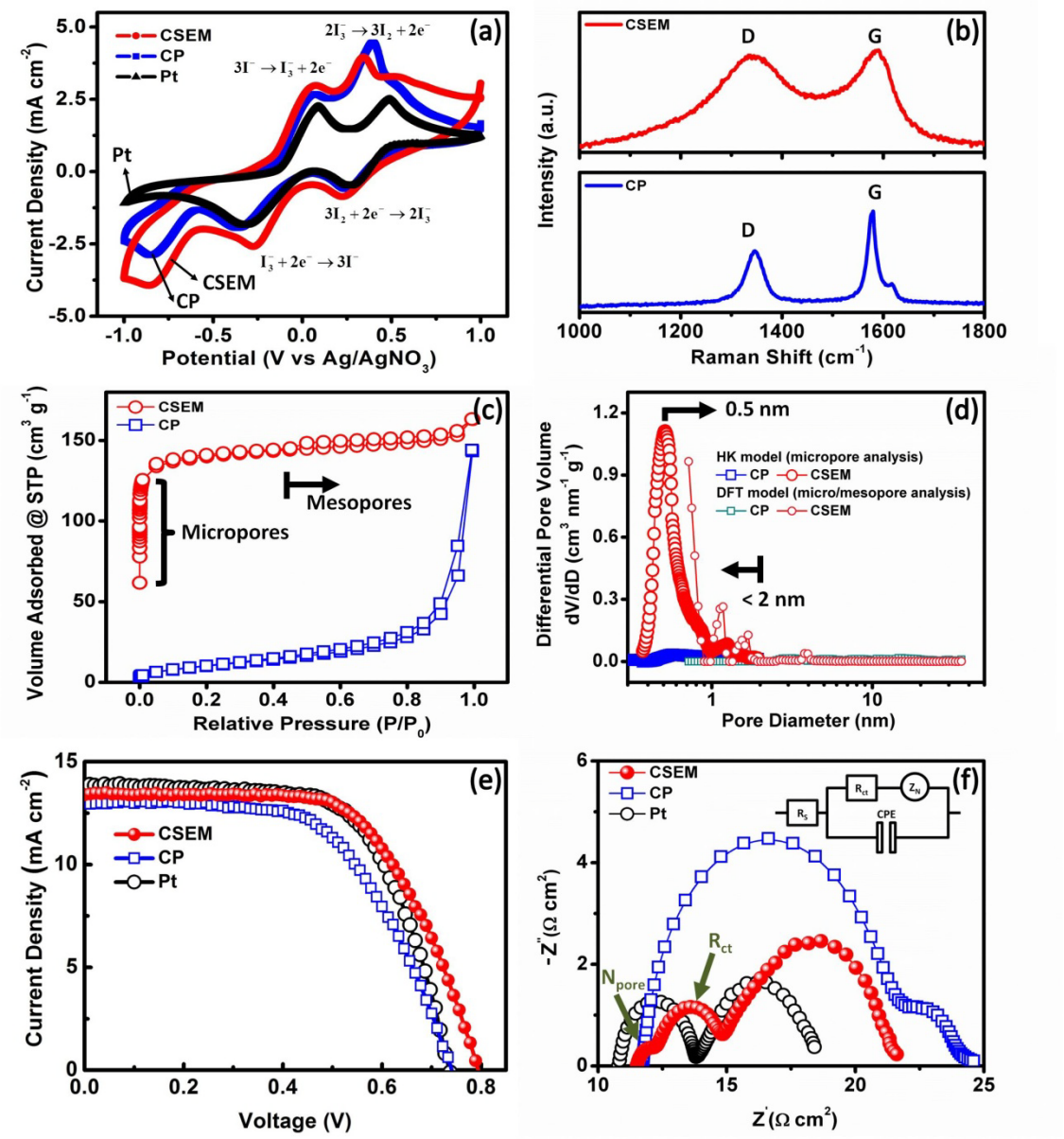

Figure 6.3. (a) Cyclic voltammetry of CSEM, CP, and Pt at 100 mV s^{-1}, (b) Raman spectra of CSEM and CP, (c) nitrogen adsorption-desorption isotherms of CSEM and CP, (d) pore-size distributions of CSEM and CP, (e) J-V characteristics of DSSCs with CSEM, CP, and Pt CEs, and (f) Nyquist plots of CSEM, CP, and Pt CEs.

Current density-voltage (J-V) measurements under the AM 1.5 G condition were carried out to evaluate the conversion efficiencies of a DSSC with a CE based on CSEMs. Figure 6.3e shows that the J-V measurement of a DSSC using a CE based on CSEMs exhibits an efficiency of 6.71%, comparable to that obtained with a Pt-based CE (6.63%). (The error bar in efficiency is estimated to be ±0.02%.) All photovoltaic parameters are summarized in Table 6.1. It is worth noting that the photovoltaic performance of the DSSC with a CE based on CSEMs presents a significant improvement in the open circuit voltage (V_{oc}) from 736 mV to 795 mV. The increase in the V_{oc} in a DSSC can arise from the positive potential shift of the I^-/I_3^- redox couple relative to the Fermi level of TiO_2. As shown above, the electrocatalytic activity of the CE based on CSEMs has a positive influence on the I^-/I_3^- redox potential, which improves the V_{oc}.[162, 167, 168] This result confirms that the microporous structure of the CSEMs can facilitate the triiodide regeneration, thus making the CSEM a promising natural and abundant counter electrode for use in DSSCs.

Table 6.1. Photovoltaic parameters of DSSCs based on CSEM, CP, and Pt CEs measured under AM 1.5 G. The EIS parameters were obtained with a symmetric dummy cell in the dark.

Counter Electrode	V_{oc} (V)	J_{sc} (mA cm^{-2})	FF (%)	Eff. (%)	R_S (Ω cm^2)	R_{ct} (Ω cm^2)
CSEM	795	13.40	63.07	6.71	11.54	1.22
CP	740	12.98	58.99	5.66	11.72	4.68
Pt	736	13.78	65.33	6.63	10.81	1.38

(The error bar of EIS is estimated to be ±0.05 Ω cm^2.)

In addition, as compared with the device performance of DSSCs based on other carbonized naturally-derived CEs in Table 6.2, our CSEM-based CE not only shows a competitive conversion efficiency to a Pt CE but also provides a facile approach for large-scale manufacturing of low-cost CEs.

Table 6.2. Reported efficiencies of DSSCs based on carbonized naturally-derived CEs.[162, 163] ST represents sea tangle.

Counter Electrode	V_{oc} (V)	J_{sc} (mA cm^{-2})	FF (%)	Eff. (%)	Eff.(Pt) (%)	R_{ct} (Ω cm^2)
ST	777	14.45	70.00	7.82	8.11	2.25
Oak	-	-	-	7.98	7.93	2.01
CSEM	795	13.40	63.07	6.71	6.63	1.22

It should be noted that the J_{sc} of a DSSC with a Pt CE is slightly higher than that of a DSSC with a CSEM-based CE due to its higher reflectance. The influence of CP in the DSSC with a CSEM-based CE was evaluated by mixing different amounts of CP into CSEMs in Figure 6.4. The maximum efficiency of the DSSC occurs when the concentration of the CP is 50 wt.% due to the simultaneously improvement of the adhesion, the catalytic activity, and the resistivity. The resistivity of CSEM-based CE as a function of the amount of CP in Figure 6.5 indicates that the added amount of CP effectively improves the electron transport between the fractures of CSEM, leading to the reduced resistivity of the CSEM-based CE by two orders of magnitude. However, all the CSEM-based CEs still have the higher resistivity than the complete CSEM without grinding (5.57×10^{-4} Ω m), suggesting that there is much space for the development of CSEM-based CEs to improve the device performance.

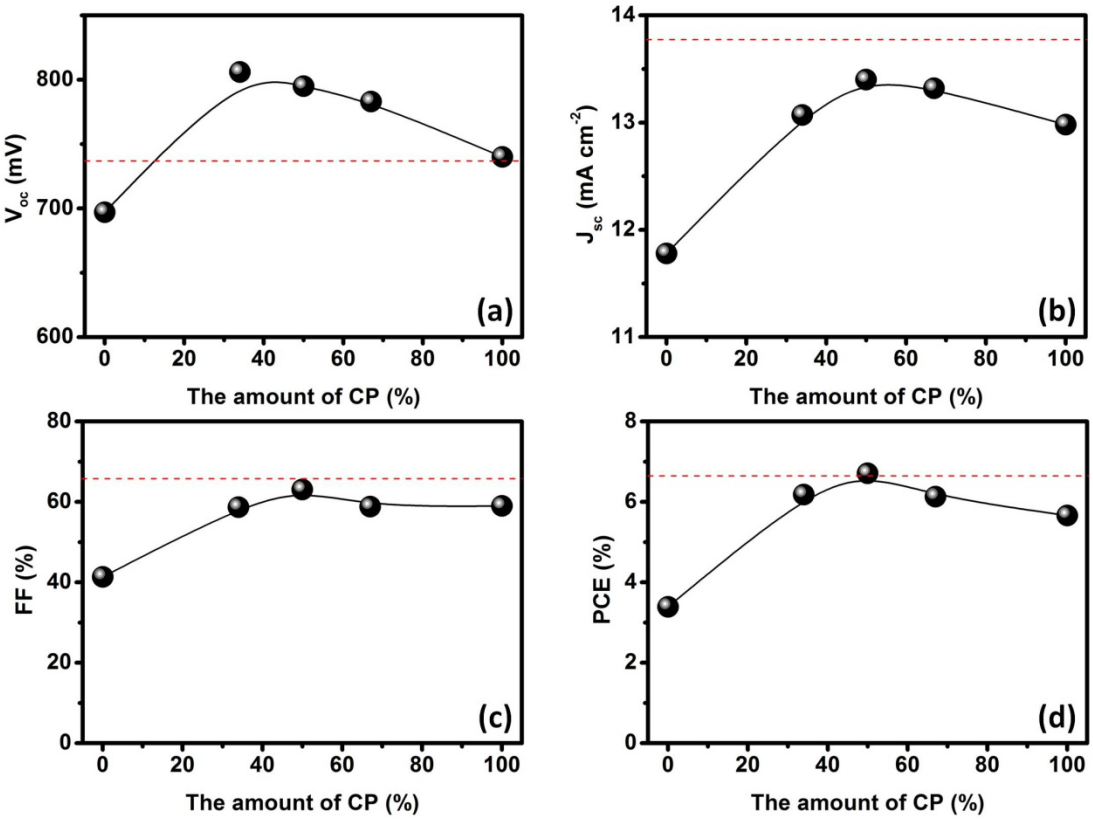

Figure 6.4. DSSC device parameters as a function of the ratio of CP: (a) V_{oc}, (b) J_{sc}, (c) FF, and (d) PCE. The red dashed lines correspond to the device parameters of a DSSC with a CE based on Pt.

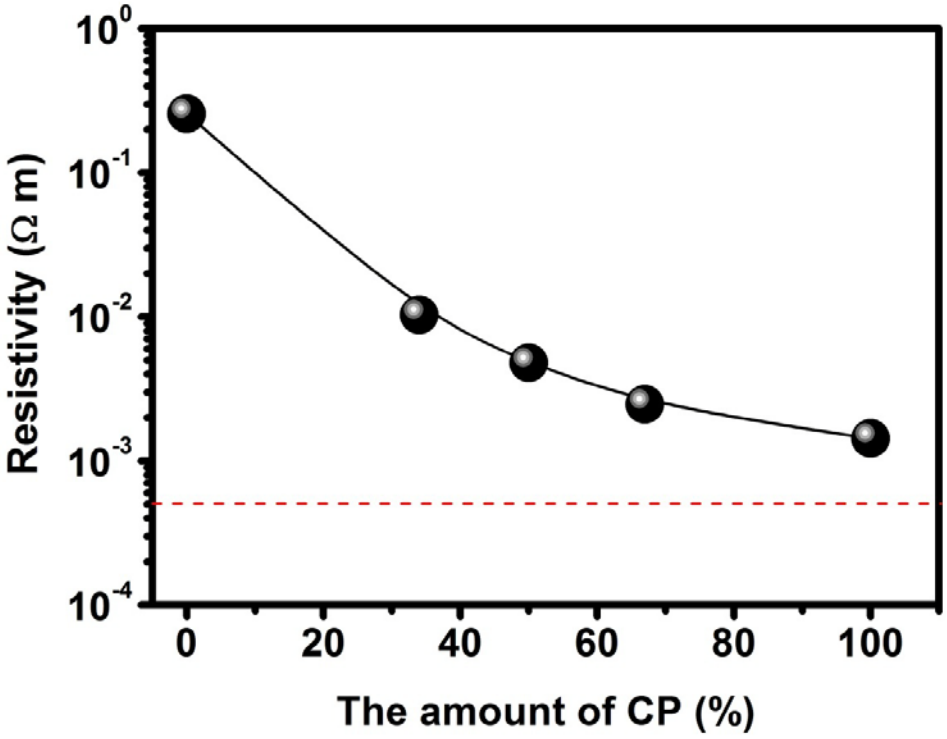

Figure 6.5. Resistivity of the counter electrode as a function of the ratio of CP. The red dashed line represents the resistivity of the complete carbonized sucrose-coated eggshell membrane without grinding (5.57×10^{-4} Ω m).

In order to further understand the charge transfer resistance at the interface between the CE and the electrolyte, electrochemical impedance spectroscopy (EIS) of a CE based on CSEMs was conducted with a symmetrical dummy cell configuration in the frequency range of 10 mHz to 100 kHz at open circuit with a zero bias potential. The magnitude of the alternating signal was 10 mV. The Nyquist plots shown in Figure 6.3f were modeled according to the equivalent circuit diagram depicted in the inset of Figure 6.3f.

The intercept of the Nyquist plot at the real axis (Z') is the series resistance (R_s) of the cell. In the case of Pt counter electrode, a typical curve of two semicircles is observed. The semicircle in the low-frequency range is associated with the Nernst diffusion impedance (Z_w), which corresponds to the diffusion in the electrolyte. The other semicircle in the high-frequency range is the charge transfer resistance (R_{ct}), which originates from the interface between the electrolyte and the CE. The CSEM-based CE, unlike the Pt CE, exhibits an additional semicircle attributed to a secondary Nernst diffusion impedance (N_{pore}). This is likely because the diffusion of I^-/I_3^- in the electrolyte is significantly affected by the microporous CSEM structure.[88, 169] The impedance parameters determined from the equivalent circuit modeling are listed in Table 6.1. The higher FF obtained by a DSSC with a Pt CE can be attributed to its lower series resistance as compared to the DSSC with a CSEM-based CE. However, the CE based on CSEMs possesses a lower charge-transfer resistance (1.22 Ω cm^2) than that of Pt (1.38 Ω cm^2), which agrees well with its high catalytic activity for I^-/I_3^- as shown by the cyclic voltammetry measurement. In addition, the lower charge-transfer resistance of the CSEM-based CE than that of mesoporous oak-based CE (2.01 Ω cm^2) and macroporous sea tangle-based CE (2.25 Ω cm^2) indicates that the smaller size of the

micropore can give a superior catalytic activity to facilitate the triiodide regeneration due to its fast charge transfer.[162, 163]

6.4 Conclusions

In summary, we have demonstrated a low-cost, natural CE, recycled from domestic waste, for use in DSSCs as a substitute for the scarce and expensive Pt CE. The unique hierarchically porous microstructure of the CSEMs effectively facilitates the I^-/I_3^- redox in the DSSC light-electricity conversion process, leading to an improvement of the V_{oc} and a conversion efficiency comparable to that with a Pt CE.

Chapter 7: Summary

This dissertation focused on an exploration of the design and development of efficient solar cells with earth-abundant materials and low-cost processes. Two types of solar cells have been investigated: (i) thin-film solar cells and (ii) dye-sensitized solar cells.

In thin-film solar cells, the Cu-poor and Zn-rich $Cu_2ZnSn(S,Se)_4$ nanocrystals with varying S to Se ratios were successfully synthesized and varied by a facile hot-injection approach. The evolution of $Cu_2ZnSn(S,Se)_4$ nanocrystals to $Cu_2ZnSn(S,Se)_4$ film was investigated for the first time by tuning the ratio of Se to S in $Cu_2ZnSn(S,Se)_4$ nanocrystals followed by a sulfurization step. It was found that minimizing the possibility for the loss of Sn during heat treatment and producing a dense film with large grain size are beneficial for the device performance. Accordingly, a novel low-cost superstrate-type device architecture has been demonstrated, offering an opportunity for the $Cu_2ZnSn(S,Se)_4$ system to circumvent challenges in the existing substrate-type architecture such as decomposition of $Cu_2ZnSn(S,Se)_4$ and a possible Schottky barrier at the $Mo/Cu_2ZnSn(S,Se)_4$ interface. In addition, by developing a robust precursor film with the addition of ethyl cellulose, the loss of Sn associated with the conversion of CZTSe to CZTSSe during the grain growth process has been mitigated, leading to an increase in the conversion efficiency compared to that of the precursor film without using ethyl cellulose. However, there is still room for the improvement of the microstructure and a compact film with larger grain size is required for high efficiency CZTSSe solar devices.

In dye-sensitized solar cells, a designed microstructure of template-free TiO_2 hollow submicrospheres embedded with SnO_2 nanobeans has been developed for use as a versatile scattering layer in DSSCs. It has been found that the template-free TiO_2 hollow

submicrospheres (TiO_2 HS) with a diameter of 600 nm can not only be fabricated with an inside-out Ostwald ripening process but also be robust enough for the subsequent process of embedding SnO_2 nanobeans. The SnO_2 embedded over the hollow sphere possesses a nanobean shape of ~ 5 nm, which effectively decorates the surface of TiO_2 HS and increases its surface area from 40 to 56 $m^2\ g^{-1}$, leading to an increase in the dye adsorption from 6.11×10^{-8} to 8.03×10^{-8} mol cm^{-2} and improvement in the short-circuit-current density J_{sc}. In addition, due to the embedding of the high mobility SnO_2 over the hollow sphere, the device with the scattering layer of SnO_2-embedded TiO_2 HS exhibits a lower electron recombination than those with TiO_2 HS and SnO_2, which agrees well with the observation of a high V_{oc} obtained with the SnO_2-embedded TiO_2 HS. Thus, our designed structure simultaneously promotes dye adsorption, light harvesting, and electron transport, leading to a 28 % improvement in the conversion efficiency as compared with the film-based SnO_2.

Furthermore, a naturally-derived carbonaceous material as a Pt-free counter electrode for DSSCs has also been developed in the form of a carbonized sucrose-coated eggshell membrane (CSEM). This material was made from eggshell membranes that were recycled from domestic waste and applied to DSSCs by the doctor-blade method for the first time. It can be found that the CSEM itself possesses the ability to catalyze the iodide/triiodide redox couple due to its defects and disorder in the structure. In addition, the unique hierarchically-porous microstructure of CSEM exhibits a high surface area of 401 $m^2\ g^{-1}$, leading to a superior electrocatalytic activity for tri-iodide regeneration. The HK pore-size distribution model confirms that the high microporosity of the CSEM is mostly due to a pore size of 0.5 nm. It allows the triiodide ions with a minimum diameter of 0.3 nm to effectively penetrate into the electrocatalytically active defect-rich micropores of CSEM and readily undergo the charge transfer process for the regeneration

of iodide/tri-iodide, leading to an improved V_{oc} and a competitive efficiency comparable to that of a DSSC with a traditional Pt-based counter electrode. Thus, this study not only demonstrates that natural materials with a micropore-rich microstructure can facilitate the charge-transfer process but also brings new insights into the future application of natural materials for use in DSSCs.

Appendix: List of Publications

1. B. Reeja-Jayan, Katharine L. Harrison, K. Yang, **Chih-Liang Wang**, A. E. Yilmaz and Arumugam Manthiram, "Microwave-assisted Low-temperature Growth of Thin Films in Solution," *Scientific Reports* **2**, 1003: 1-8 (2012).
2. **Chih-Liang Wang**, Chih-Chieh Wang, B. Reeja-Jayan and Arumugam Manthiram, "Low-cost, Mo(S,Se)2-free superstrate-type solar cells fabricated with tunable band gap $Cu_2ZnSn(S_{1-x}Se_x)_4$ nanocrystal-based inks and the effect of sulfurization," *RSC Advances* **3**, 19946-19951 (2013).
3. **Chih-Liang Wang** and Arumugam Manthiram, "Low-cost CZTSSe solar cells fabricated with low band gap CZTSe nanocrystals, environmentally friendly binder, and non-vacuum processes," *ACS Sustainable Chemistry & Engineering* **2**, 561-568 (2014).
4. **Chih-Liang Wang**, Jin-Yun Liao, Sheng-Heng Chung and Arumugam Manthiram, "Carbonized Eggshell Membranes as a Natural and Abundant Counter Electrode for Efficient Dye-sensitized Solar Cells," *Advanced Energy Materials* (under review).
5. **Chih-Liang Wang**, Jin-Yun Liao, Yubao Zhao and Arumugam Manthiram, "Template-free TiO_2 Hollow Submicrospheres Embedded with SnO_2 Nanobeans as a Versatile Scattering Layer for Dye-sensitized Solar Cells," *Chemical Communications* (under review).

References

1. H. W. Hillhouse and M. C. Beard, *Curr. Opin. Colloid Interface Sci.*, 2009, **14**, 245-259.
2. M. A. Green, K. Emery, Y. Hishikawa, W. Warta and E. D. Dunlop, *Prog. Photovoltaics*, 2013, **21**, 1-11.
3. I. Repins, M. A. Contreras, B. Egaas, C. DeHart, J. Scharf, C. L. Perkins, B. To and R. Noufi, *Prog. Photovoltaics*, 2008, **16**, 235-239.
4. A. Bosio, N. Romeo, S. Mazzamuto and V. Canevari, *Prog. Cryst. Growth Charact. Mater.*, 2006, **52**, 247-279.
5. J. Britt and C. Ferekides, *Appl. Phys. Lett.*, 1993, **62**, 2851-2852.
6. J. Meier, R. Flückiger, H. Keppner and A. Shah, *Appl. Phys. Lett.*, 1994, **65**, 860-862.
7. D. B. Mitzi, O. Gunawan, T. K. Todorov, K. Wang and S. Guha, *Sol. Energy Mater. Sol. Cells*, 2011, **95**, 1421-1436.
8. D. B. Mitzi, O. Gunawan, T. K. Todorov and D. A. R. Barkhouse, *Philos. Trans. R. Soc. A-Math. Phys. Eng. Sci.*, 2013, **371**, 20110432.
9. K. I. a. T. Nakazawa, *Jpn. J. Appl. Phys. Part 1 - Regul. Pap. Short Notes Rev. Pap.*, 1988, **27**, 2094.
10. K. Hironori, J. Kazuo, Y. Satoru, K. Tsuyoshi, M. Win Shwe, F. Tatsuo, I. Tadashi and M. Tomoyoshi, *Appl. Phys. Express*, 2008, **1**, 041201.
11. C. A. Wolden, J. Kurtin, J. B. Baxter, I. Repins, S. E. Shaheen, J. T. Torvik, A. A. Rockett, V. M. Fthenakis and E. S. Aydil, *J. Vac. Sci. Technol. A*, 2011, **29**, 030801.

12. H. Katagiri, K. Saitoh, T. Washio, H. Shinohara, T. Kurumadani and S. Miyajima, *Sol. Energy Mater. Sol. Cells*, 2001, **65**, 141-148.

13. K. Takeshi, J. Kazuo, T. Kazuyuki, S. Shunsuke, O. Taisuke and K. Hironori, *Jpn. J. Appl. Phys.*, 2005, **44**, 783.

14. H. Katagiri, *Thin Solid Films*, 2005, **480–481**, 426-432.

15. H. Araki, A. Mikaduki, Y. Kubo, T. Sato, K. Jimbo, W. S. Maw, H. Katagiri, M. Yamazaki, K. Oishi and A. Takeuchi, *Thin Solid Films*, 2008, **517**, 1457-1460.

16. K. Wang, O. Gunawan, T. Todorov, B. Shin, S. J. Chey, N. A. Bojarczuk, D. Mitzi and S. Guha, *Appl. Phys. Lett.*, 2010, **97**, 143508.

17. B. Shin, O. Gunawan, Y. Zhu, N. A. Bojarczuk, S. J. Chey and S. Guha, *Prog. Photovoltaics*, 2013, **21**, 72-76.

18. A. Ennaoui, M. Lux-Steiner, A. Weber, D. Abou-Ras, I. Kotschau, H. W. Schock, R. Schurr, A. Holzing, S. Jost, R. Hock, T. Voss, J. Schulze and A. Kirbs, *Thin Solid Films*, 2009, **517**, 2511-2514.

19. H. Araki, Y. Kubo, K. Jimbo, W. S. Maw, H. Katagiri, M. Yamazaki, K. Oishi and A. Takeuchi, *Phys. Status Solidi C*, 2009, **6**, 1266-1268.

20. H. Araki, Y. Kubo, A. Mikaduki, K. Jimbo, W. S. Maw, H. Katagiri, M. Yamazaki, K. Oishi and A. Takeuchi, *Sol. Energy Mater. Sol. Cells*, 2009, **93**, 996-999.

21. J. J. Scragg, D. M. Berg and P. J. Dale, *J. Electroanal. Chem.*, 2010, **646**, 52-59.

22. L. Guo, Y. Zhu, O. Gunawan, T. Gokmen, V. R. Deline, S. Ahmed, L. T. Romankiw and H. Deligianni, *Prog. Photovoltaics*, 2014, **22**, 58-68.

23. K. Maeda, K. Tanaka, Y. Fukui and H. Uchiki, *Sol. Energy Mater. Sol. Cells*, 2011, **95**, 2855-2860.

24. W. Ki and H. W. Hillhouse, *Adv. Energy Mater.*, 2011, **1**, 732-735.

25. H. Xin, J. K. Katahara, I. L. Braly and H. W. Hillhouse, *Adv. Energy Mater.*, 2014, DOI: 10.1002/aenm.201301823.

26. C. J. Stolle, T. B. Harvey and B. A. Korgel, *Curr. Opin. Chem. Eng.*, 2013, **2**, 160-167.

27. C. Steinhagen, M. G. Panthani, V. Akhavan, B. Goodfellow, B. Koo and B. A. Korgel, *J. Am. Chem. Soc.*, 2009, **131**, 12554-12555.

28. Q. J. Guo, H. W. Hillhouse and R. Agrawal, *J. Am. Chem. Soc.*, 2009, **131**, 11672-11673.

29. Q. Guo, G. M. Ford, W. C. Yang, B. C. Walker, E. A. Stach, H. W. Hillhouse and R. Agrawal, *J. Am. Chem. Soc.*, 2010, **132**, 17384-17386.

30. Y. Y. Cao, M. S. Denny, J. V. Caspar, W. E. Farneth, Q. J. Guo, A. S. Ionkin, L. K. Johnson, M. J. Lu, I. Malajovich, D. Radu, H. D. Rosenfeld, K. R. Choudhury and W. Wu, *J. Am. Chem. Soc.*, 2012, **134**, 15644-15647.

31. T. K. Todorov, K. B. Reuter and D. B. Mitzi, *Adv. Mater.*, 2010, **22**, E156-E159.

32. D. A. R. Barkhouse, O. Gunawan, T. Gokmen, T. K. Todorov and D. B. Mitzi, *Prog. Photovoltaics*, 2012, **20**, 6-11.

33. T. K. Todorov, J. Tang, S. Bag, O. Gunawan, T. Gokmen, Y. Zhu and D. B. Mitzi, *Adv. Energy Mater.*, 2013, **3**, 34-38.

34. W. Wang, M. T. Winkler, O. Gunawan, T. Gokmen, T. K. Todorov, Y. Zhu and D. B. Mitzi, *Adv. Energy Mater.*, 2014, DOI: 10.1002/aenm.201301465.

35. M. T. Winkler, W. Wang, O. Gunawan, H. J. Hovel, T. K. Todorov and D. B. Mitzi, *Energy Environ. Sci.*, 2014, **7**, 1029-1036.

36. T. Todorov, O. Gunawan, S. J. Chey, T. G. de Monsabert, A. Prabhakar and D. B. Mitzi, *Thin Solid Films*, 2011, **519**, 7378-7381.

37. R. Haight, A. Barkhouse, O. Gunawan, B. Shin, M. Copel, M. Hopstaken and D. B. Mitzi, *Appl. Phys. Lett.*, 2011, **98**, 253502.

38. D. A. R. Barkhouse, R. Haight, N. Sakai, H. Hiroi, H. Sugimoto and D. B. Mitzi, *Appl. Phys. Lett.*, 2012, **100**, 193904.

39. D. Hariskos, S. Spiering and M. Powalla, *Thin Solid Films*, 2005, **480–481**, 99-109.

40. S. Ahmad, E. Guillen, L. Kavan, M. Grätzel and M. K. Nazeeruddin, *Energy Environ. Sci.*, 2013, **6**, 3439-3466.

41. M. Wu and T. Ma, *J. Phys. Chem. C*, 2014, **118**, 16727-16742.

42. P. Li, J. Wu, J. Lin, M. Huang, Z. Lan and Q. Li, *Electrochim. Acta*, 2008, **53**, 4161-4166.

43. G. Wang, R. Lin, Y. Lin, X. Li, X. Zhou and X. Xiao, *Electrochim. Acta*, 2005, **50**, 5546-5552.

44. M. Ikegami, K. Miyoshi, T. Miyasaka, K. Teshima, T. C. Wei, C. C. Wan and Y. Y. Wang, *Appl. Phys. Lett.*, 2007, **90**, 153122.

45. E. Olsen, G. Hagen and S. Eric Lindquist, *Sol. Energy Mater. Sol. Cells*, 2000, **63**, 267-273.

46. L. Chen, W. Tan, J. Zhang, X. Zhou, X. Zhang and Y. Lin, *Electrochim. Acta*, 2010, **55**, 3721-3726.

47. X. Fang, T. Ma, G. Guan, M. Akiyama, T. Kida and E. Abe, *J. Electroanal. Chem.*, 2004, **570**, 257-263.

48. B. Zhang, D. Wang, Y. Hou, S. Yang, X. H. Yang, J. H. Zhong, J. Liu, H. F. Wang, P. Hu, H. J. Zhao and H. G. Yang, *Sci. Rep.*, 2013, **3**, 1386.

49. R. Narayanan and M. A. El-Sayed, *Nano Lett.*, 2004, **4**, 1343-1348.

50. S. Mathew, A. Yella, P. Gao, R. Humphry-Baker, F. E. CurchodBasile, N. Ashari-Astani, I. Tavernelli, U. Rothlisberger, K. NazeeruddinMd and M. Grätzel, *Nat Chem*, 2014, **6**, 242-247.

51. M. Wu, X. Lin, T. Wang, J. Qiu and T. Ma, *Energy Environ. Sci.*, 2011, **4**, 2308-2315.

52. Y. Gao, L. Chu, M. Wu, L. Wang, W. Guo and T. Ma, *J. Photochem. Photobiol. A-Chem.*, 2012, **245**, 66-71.

53. C. Bu, Y. Liu, Z. Yu, S. You, N. Huang, L. Liang and X.-Z. Zhao, *ACS Appl. Mater. Interfaces*, 2013, **5**, 7432-7438.

54. J. S. Jang, D. J. Ham, E. Ramasamy, J. Lee and J. S. Lee, *Chem. Commun.*, 2010, **46**, 8600-8602.

55. M. Wu, X. Lin, A. Hagfeldt and T. Ma, *Angew. Chem.-Int. Edit.*, 2011, **50**, 3520-3524.

56. G. R. Li, J. Song, G. L. Pan and X. P. Gao, *Energy Environ. Sci.*, 2011, **4**, 1680-1683.

57. M. Wang, A. M. Anghel, B. Marsan, N.-L. Cevey Ha, N. Pootrakulchote, S. M. Zakeeruddin and M. Grätzel, *J. Am. Chem. Soc.*, 2009, **131**, 15976-15977.

58. S.-H. Chang, M.-D. Lu, Y.-L. Tung and H.-Y. Tuan, *ACS Nano*, 2013, **7**, 9443-9451.

59. C.-W. Kung, H.-W. Chen, C.-Y. Lin, K.-C. Huang, R. Vittal and K.-C. Ho, *ACS Nano*, 2012, **6**, 7016-7025.

60. H. Sun, D. Qin, S. Huang, X. Guo, D. Li, Y. Luo and Q. Meng, *Energy Environ. Sci.*, 2011, **4**, 2630-2637.

61. W. Zhao, X. Zhu, H. Bi, H. Cui, S. Sun and F. Huang, *J. Power Sources*, 2013, **242**, 28-32.

62. H. K. Mulmudi, S. K. Batabyal, M. Rao, R. R. Prabhakar, N. Mathews, Y. M. Lam and S. G. Mhaisalkar, *Phys. Chem. Chem. Phys.*, 2011, **13**, 19307-19309.

63. H. Zhang, L. Yang, Z. Liu, M. Ge, Z. Zhou, W. Chen, Q. Li and L. Liu, *J. Mater. Chem.*, 2012, **22**, 18572-18577.

64. Y.-C. Wang, D.-Y. Wang, Y.-T. Jiang, H.-A. Chen, C.-C. Chen, K.-C. Ho, H.-L. Chou and C.-W. Chen, *Angew. Chem.-Int. Edit.*, 2013, **52**, 6694-6698.

65. Q.-H. Huang, T. Ling, S.-Z. Qiao and X.-W. Du, *J. Mater. Chem. A*, 2013, **1**, 11828-11833.

66. M. Wu, Y. Wang, X. Lin, N. Yu, L. Wang, L. Wang, A. Hagfeldt and T. Ma, *Phys. Chem. Chem. Phys.*, 2011, **13**, 19298-19301.

67. M. Wu, J. Bai, Y. Wang, A. Wang, X. Lin, L. Wang, Y. Shen, Z. Wang, A. Hagfeldt and T. Ma, *J. Mater. Chem.*, 2012, **22**, 11121-11127.

68. F. Gong, H. Wang, X. Xu, G. Zhou and Z.-S. Wang, *J. Am. Chem. Soc.*, 2012, **134**, 10953-10958.

69. F. Gong, X. Xu, Z. Li, G. Zhou and Z.-S. Wang, *Chem. Commun.*, 2013, **49**, 1437-1439.

70. Z. Zhang, S. Pang, H. Xu, Z. Yang, X. Zhang, Z. Liu, X. Wang, X. Zhou, S. Dong, X. Chen, L. Gu and G. Cui, *RSC Adv.*, 2013, **3**, 16528-16533.

71. J. Guo, Y. Shi, C. Zhu, L. Wang, N. Wang and T. Ma, *J. Mater. Chem. A*, 2013, **1**, 11874-11879.

72. J. Guo, Y. Shi, Y. Chu and T. Ma, *Chem. Commun.*, 2013, **49**, 10157-10159.

73. X. Xin, M. He, W. Han, J. Jung and Z. Lin, *Angew. Chem.-Int. Edit.*, 2011, **50**, 11739-11742.

74. J. Wang, X. Xin and Z. Lin, *Nanoscale*, 2011, **3**, 3040-3048.

75. S.-J. Yuan, Z.-J. Zhou, Z.-L. Hou, W.-H. Zhou, R.-Y. Yao, Y. Zhao and S.-X. Wu, *Chem.-Eur. J.*, 2013, **19**, 10107-10110.

76. J. Yang, C. Bao, J. Zhang, T. Yu, H. Huang, Y. Wei, H. Gao, G. Fu, J. Liu and Z. Zou, *Chem. Commun.*, 2013, **49**, 2028-2030.

77. J.-Y. Lin and S.-W. Chou, *Electrochem. Commun.*, 2013, **37**, 11-14.

78. X. Zheng, J. Guo, Y. Shi, F. Xiong, W.-H. Zhang, T. Ma and C. Li, *Chem. Commun.*, 2013, **49**, 9645-9647.

79. M. Wu and T. Ma, *ChemSusChem*, 2012, **5**, 1343-1357.

80. M. Wu, X. Lin, Y. Wang, L. Wang, W. Guo, D. Qi, X. Peng, A. Hagfeldt, M. Grätzel and T. Ma, *J. Am. Chem. Soc.*, 2012, **134**, 3419-3428.

81. M. Wu, X. Lin, L. Wang, W. Guo, Y. Wang, J. Xiao, A. Hagfeldt and T. Ma, *The J. Phys. Chem. C*, 2011, **115**, 22598-22602.

82. G. Liu, X. Li, H. Wang, Y. Rong, Z. Ku, M. Xu, L. Liu, M. Hu, Y. Yang and H. Han, *J. Mater. Chem. A*, 2013, **1**, 1475-1480.

83. J.-Y. Lin, G. Yue, S.-Y. Tai, Y. Xiao, H.-M. Cheng, F.-M. Wang and J. Wu, *Mater. Chem. Phys.*,2013, **143**, 53-59.

84. J.-Y. Lin, C.-Y. Chan and S.-W. Chou, *Chem. Commun.*, 2013, **49**, 1440-1442.

85. H. Bi, W. Zhao, S. Sun, H. Cui, T. Lin, F. Huang, X. Xie and M. Jiang, *Carbon*, 2013, **61**, 116-123.

86. G. Yue, J. Wu, J.-Y. Lin, Y. Xiao, S.-Y. Tai, J. Lin, M. Huang and Z. Lan, *Carbon*, 2013, **55**, 1-9.

87. S.-Y. Tai, C.-J. Liu, S.-W. Chou, F. S.-S. Chien, J.-Y. Lin and T.-W. Lin, *J. Mater. Chem.*, 2012, **22**, 24753-24759.

88. H. Zheng, C. Y. Neo and J. Ouyang, *ACS Appl. Mater. Interfaces*, 2013, **5**, 6657-6664.

89. M. Wu, Y. Wang, X. Lin, W. Guo, K. Wu, Y.-n. Lin, H. Guo and T. Ma, *J. Mater. Chem. A*, 2013, **1**, 9672-9679.

90. L. Yi, Y. Liu, N. Yang, Z. Tang, H. Zhao, G. Ma, Z. Su and D. Wang, *Energy Environ. Sci.*, 2013, **6**, 835-840.

91. T. G. Deepak, G. S. Anjusree, S. Thomas, T. A. Arun, S. V. Nair and A. Sreekumaran Nair, *RSC Adv.*, 2014, **4**, 17615-17638.

92. L. Zhao, J. Li, Y. Shi, S. Wang, J. Hu, B. Dong, H. Lu and P. Wang, *J. Alloy. Compd.*, 2013, **575**, 168-173.

93. J. Qi, X. Dang, P. T. Hammond and A. M. Belcher, *ACS Nano*, 2011, **5**, 7108-7116.

94. X. Kou, S. Zhang, C.-K. Tsung, Z. Yang, M. H. Yeung, G. D. Stucky, L. Sun, J. Wang and C. Yan, *Chem.-Eur. J.*, 2007, **13**, 2929-2936.

95. W. Ni, X. Kou, Z. Yang and J. Wang, *ACS Nano*, 2008, **2**, 677-686.

96. Z. Sun, J. H. Kim, Y. Zhao, D. Attard and S. X. Dou, *Chem. Commun.*, 2013, **49**, 966-968.

97. Z. Dong, H. Ren, C. M. Hessel, J. Wang, R. Yu, Q. Jin, M. Yang, Z. Hu, Y. Chen, Z. Tang, H. Zhao and D. Wang, *Adv. Mater.*, 2014, **26**, 905-909.

98. L. De Marco, M. Manca, R. Giannuzzi, M. R. Belviso, P. D. Cozzoli and G. Gigli, *Energy Environ. Sci.*, 2013, **6**, 1791-1795.

99. M. Liang and J. Chen, *Chem. Soc. Rev.*, 2013, **42**, 3453-3488.

100. Y.-S. Yen, H.-H. Chou, Y.-C. Chen, C.-Y. Hsu and J. T. Lin, *J. Mater. Chem.*, 2012, **22**, 8734-8747.

101. J. J. Scragg, T. Ericson, T. Kubart, M. Edoff and C. Platzer-Bjorkman, *Chem. Mat.*, 2011, **23**, 4625-4633.

102. A. Weber, R. Mainz and H. W. Schock, *J. Appl. Phys.*, 2010, **107**, 013516.

103. A. Redinger, D. M. Berg, P. J. Dale and S. Siebentritt, *J. Am. Chem. Soc.*, 2011, **133**, 3320-3323.

104. O. Gunawan, T. K. Todorov and D. B. Mitzi, *Appl. Phys. Lett.*, 2010, **97**, 233506.

105. J. J. Scragg, J. T. Watjen, M. Edoff, T. Ericson, T. Kubart and C. Platzer-Bjorkman, *J. Am. Chem. Soc.*, 2012, **134**, 19330-19333.

106. B. Shin, Y. Zhu, N. A. Bojarczuk, S. J. Chey and S. Guha, *Appl. Phys. Lett.*, 2012, **101**, 053903.

107. C. L. Wang, W. C. Shih, J. W. Liao, Y. C. Wu, C. H. Chen, C. C. Wang and C. H. Lai, *J. Electrochem. Soc.*, 2011, **158**, C231-C235.

108. K. Woo, Y. Kim and J. Moon, *Energy Environ. Sci.*, 2012, **5**, 5340-5345.

109. I. Repins, C. Beall, N. Vora, C. DeHart, D. Kuciauskas, P. Dippo, B. To, J. Mann, W. C. Hsu, A. Goodrich and R. Noufi, *Sol. Energy Mater. Sol. Cells*, 2012, **101**, 154-159.

110. S. Bag, O. Gunawan, T. Gokmen, Y. Zhu, T. K. Todorov and D. B. Mitzi, *Energy Environ. Sci.*, 2012, **5**, 7060-7065.

111. G. Zoppi, I. Forbes, R. W. Miles, P. J. Dale, J. J. Scragg and L. M. Peter, *Prog. Photovoltaics*, 2009, **17**, 315-319.

112. S. C. Riha, B. A. Parkinson and A. L. Prieto, *J. Am. Chem. Soc.*, 2011, **133**, 15272-15275.

113. K. L. Ou, J. C. Fan, J. K. Chen, C. C. Huang, L. Y. Chen, J. H. Ho and J. Y. Chang, *J. Mater. Chem.*, 2012, **22**, 14667-14673.

114. Q. Guo, G. M. Ford, H. W. Hillhouse and R. Agrawal, *Nano Lett.*, 2009, **9**, 3060-3065.

115. S. Y. Chen, X. G. Gong, A. Walsh and S. H. Wei, *Appl. Phys. Lett.*, 2010, **96**, 021902.

116. H.-S. Duan, W. Yang, B. Bob, C.-J. Hsu, B. Lei and Y. Yang, *Adv. Funct. Mater.*, 2012, **23**, 1466-1471.

117. C.-L. Wang, C.-C. Wang, B. Reeja-Jayan and A. Manthiram, *RSC Adv.*, 2013, **3**, 19946-19951.

118. I. Gur, N. A. Fromer, M. L. Geier and A. P. Alivisatos, *Science*, 2005, **310**, 462-465.

119. M. G. Panthani, V. Akhavan, B. Goodfellow, J. P. Schmidtke, L. Dunn, A. Dodabalapur, P. F. Barbara and B. A. Korgel, *J. Am. Chem. Soc.*, 2008, **130**, 16770-16777.

120. W. Ma, J. M. Luther, H. M. Zheng, Y. Wu and A. P. Alivisatos, *Nano Lett.*, 2009, **9**, 1699-1703.

121. C. Wadia, A. P. Alivisatos and D. M. Kammen, *Environ. Sci. Technol.*, 2009, **43**, 2072-2077.

122. H. Ramsurn and R. B. Gupta, *ACS Sustain. Chem. Eng.*, 2013, **1**, 779-797.

123. L. M. Peter, *Philos. Trans. R. Soc. A-Math. Phys. Eng. Sci.*, 2011, **369**, 1840-1856.

124. A. Fairbrother, E. Garcia-Hemme, V. Izquierdo-Roca, X. Fontane, F. A. Pulgarin-Agudelo, O. Vigil-Galan, A. Perez-Rodriguez and E. Saucedo, *J. Am. Chem. Soc.*, 2012, **134**, 8018-8021.

125. S. Ahn, S. Jung, J. Gwak, A. Cho, K. Shin, K. Yoon, D. Park, H. Cheong and J. H. Yun, *Appl. Phys. Lett.*, 2010, **97**, 021905.

126. H. Yoon, J. H. Woo, B. Joshi, Y. M. Ra, S. S. Yoon, H. Y. Kim, S. Ahn, J. H. Yun, J. Gwak, K. Yoon and S. C. James, *J. Electrochem. Soc.*, 2012, **159**, H444-H449.

127. S. Ahn, C. Kim, J. H. Yun, J. Gwak, S. Jeong, B. H. Ryu and K. Yoon, *J. Phys. Chem. C*, 2010, **114**, 8108-8113.

128. M. Grossberg, J. Krustok, J. Raudoja, K. Timmo, M. Altosaar and T. Raadik, *Thin Solid Films*, 2011, **519**, 7403-7406.

129. P. A. Fernandes, P. M. P. Salome and A. F. da Cunha, *J. Alloy. Compd.*, 2011, **509**, 7600-7606.

130. P. M. P. Salome, P. A. Fernandes and A. F. da Cunha, *Thin Solid Films*, 2009, **517**, 2531-2534.

131. H. R. Chandrasekhar, R. G. Humphreys, U. Zwick and M. Cardona, *Phys. Rev. B*, 1977, **15**, 2177-2183.

132. M. Ishii, K. Shibata and H. Nozaki, *J. Solid State Chem.*, 1993, **105**, 504-511.

133. R. Mainz, B. C. Walker, S. S. Schmidt, O. Zander, A. Weber, H. Rodriguez-Alvarez, J. Just, M. Klaus, R. Agrawal and T. Unold, *Phys. Chem. Chem. Phys.*, 2013, **15**, 18281-18289.

134. E. Lee, S. J. Park, J. W. Cho, J. Gwak, M. K. Oh and B. K. Min, *Sol. Energy Mater. Sol. Cells*, 2011, **95**, 2928-2932.

135. T. Maeda, S. Nakamura and T. Wada, *Jpn. J. Appl. Phys.*, 2012, **51**, 10NC11.

136. T. Nakada, N. Okano, Y. Tanaka, H. Fukuda and A. Kunioka, *Proc. 1st World Conference on Photovoltaic Energy Conversion (Hawaii, 1994)*, 1994, 95-98.

137. S. Ikeda, R. Kamai, T. Y. Yagi and M. Matsumura, *J. Electrochem. Soc.*, 2010, **157**, B99-B103.

138. C.-L. Wang and A. Manthiram, *ACS Sustain. Chem. Eng.*, 2014, **2**, 561-568.

139. B. Oregan and M. Gratzel, *Nature*, 1991, **353**, 737-740.

140. H. Yu, Y. Bai, X. Zong, F. Tang, G. Q. M. Lu and L. Wang, *Chem. Commun.*, 2012, **48**, 7386-7388.

141. G. Zhu, X. Wang, H. Li, L. Pan, H. Sun, X. Liu, T. Lv and Z. Sun, *Chem. Commun.*, 2012, **48**, 958-960.

142. Y.-Z. Zheng, J. Zhao, H. Zhang, J.-F. Chen, W. Zhou and X. Tao, *Chem. Commun.*, 2011, **47**, 11519-11521.

143. Z. Dong, X. Lai, J. E. Halpert, N. Yang, L. Yi, J. Zhai, D. Wang, Z. Tang and L. Jiang, *Adv. Mater.*, 2012, **24**, 1046-1049.

144. Y. Rui, Y. Li, Q. Zhang and H. Wang, *Nanoscale*, 2013, **5**, 12574-12581.

145. J.-Y. Liao, B.-X. Lei, D.-B. Kuang and C.-Y. Su, *Energy Environ. Sci.*, 2011, **4**, 4079-4085.

146. A. Pang, X. Sun, H. Ruan, Y. Li, S. Dai and M. Wei, *Nano Energy*, 2014, **5**, 82-90.

147. E. Hendry, M. Koeberg, B. O'Regan and M. Bonn, *Nano Lett.*, 2006, **6**, 755-759.

148. M. Chen, C. Ye, S. Zhou and L. Wu, *Adv. Mater.*, 2013, **25**, 5343-5351.

149. J. Du, J. Qi, D. Wang and Z. Tang, *Energy Environ. Sci.*, 2012, **5**, 6914-6918.

150. Y. Zhao, Q. Chen, F. Pan, H. Li, G. Q. Xu and W. Chen, *Chem.-Eur. J.*, 2014, DOI: 10.1002/chem.201400120.

151. J. Chen, L. Yang, Z. Zhang, S. Fang and S.-i. Hirano, *Chem. Commun.*, 2013, **49**, 2792-2794.

152. J.-Y. Liao and A. Manthiram, *Adv. Energy Mater.*, 2014, DOI: 10.1002/aenm.201400403.

153. Q. Wang, J.-E. Moser and M. Grätzel, *J. Phys.Chem. B*, 2005, **109**, 14945-14953.

154. A. Yella, H.-W. Lee, H. N. Tsao, C. Yi, A. K. Chandiran, M. K. Nazeeruddin, E. W.-G. Diau, C.-Y. Yeh, S. M. Zakeeruddin and M. Grätzel, *Science*, 2011, **334**, 629-634.

155. J. W. Galusha, M. R. Jorgensen and M. H. Bartl, *Adv. Mater.*, 2010, **22**, 107.

156. D. Losic, J. G. Mitchell and N. H. Voelcker, *Adv. Mater.*, 2009, **21**, 2947-2958.

157. E. Raymundo-Pinero, M. Cadek and F. Beguin, *Adv. Funct. Mater.*, 2009, **19**, 1032-1039.

158. Z. Li, L. Zhang, B. S. Amirkhiz, X. Tan, Z. Xu, H. Wang, B. C. Olsen, C. M. B. Holt and D. Mitlin, *Adv. Energy Mater.*, 2012, **2**, 431-437.

159. S.-H. Chung and A. Manthiram, *Adv. Mater.*, 2014, **26**, 1360-1365.

160. H. Yao, G. Zheng, W. Li, M. T. McDowell, Z. Seh, N. Liu, Z. Lu and Y. Cui, *Nano Lett.*, 2013, **13**, 3385-3390.

161. C. Wang, F. Meng, M. Wu, X. Lin, T. Wang, J. Qiu and T. Ma, *Phys. Chem. Chem. Phys.*, 2013, **15**, 14182-14187.

162. L. Wang, Y. T. Shi, X. G. Bai, Y. J. Xing, H. Zhang, W. Guo, N. Wang, T. L. Ma and M. Gratzel, *Energy Environ. Sci.*, 2014, **7**, 343-346.

163. Q. W. Jiang, G. R. Li, F. Wang and X. P. Gao, *Electrochem Commun.*, 2010, **12**, 924-927.

164. S.-H. Park, B.-K. Kim and W.-J. Lee, *J. Power Sources*, 2013, **239**, 122-127.

165. G. Veerappan, K. Bojan and S.-W. Rhee, *ACS Appl. Mater. Interfaces*, 2011, **3**, 857-862.

166. W. J. Lee, E. Ramasamy, D. Y. Lee and J. S. Song, *ACS Appl. Mater. Interfaces*, 2009, **1**, 1145-1149.

167. G. Veerappan, W. Kwon and S.-W. Rhee, *J. Power Sources*, 2011, **196**, 10798-10805.

168. K. Imoto, K. Takahashi, T. Yamaguchi, T. Komura, J. Nakamura and K. Murata, *Sol. Energy Mater. Sol. Cells*, 2003, **79**, 459-469.

169. J. D. Roy-Mayhew, D. J. Bozym, C. Punckt and I. A. Aksay, *ACS Nano*, 2010, **4**, 6203-6211.

Vita

Chih-Liang Wang was born in Tainan, Taiwan, and grew up at the same city. He received his B.S. and M.S. degrees in Materials Science and Engineering from National Tsing Hua University, Hsinchu, Taiwan, in 2005 and 2007, respectively. Then, he served as an alternative military service until October 2008. After that, he worked for the industry collaboration solar project at National Tsing Hua University as a research assistant. In August 2010, he entered the Materials Science and Engineering Graduate Program at the University of Texas at Austin and focused on the research and development of solar cells.

Permanent email: clwang@utexas.edu

This dissertation was typed by the author.